Design, Operation and Testing in Expansion Tube Facilities for Super-Orbital Re-entry

Peter Jacobs and Richard Morgan as editors, together with
Aaron Brandis[*], David Buttsworth[†], Andrew Dann[‡], Mary D'Souza, Troy Eichmann,
David Gildfind, Rowan Gollan, Carolyn Jacobs[§], Matthew McGilvray[‡],
Tim McIntyre, Neil Mudford, Hadas Porat, Dan Potter[¶], Fabian Zander

Centre for Hypersonics, The University of Queensland, Australia.

Correspondence: peterj@mech.uq.edu.au, r.morgan@uq.edu.au

May 18, 2013

Abstract

The expansion tube is our tool of choice for producing radiating, high-enthalpy flows relevant to the study of re-entry aerothermodynamics. First, we describe the operating principles of a free-piston-driven expansion tube and two example facilities that have been constructed at The University of Queensland. These have been applied to a range of aerothermodynamic studies and a large effort has also been put into the development of instrumentation, including surface measurements, optical and spectrometric instruments. Two situations are described where radiating and ablating flows have been created, using both preheated hot walls and walls heated by aerodynamic processes during the test.

The detailed flow in these expansion tube facilities turns out to be quite complex and computer models are needed to completely and accurately describe the experimental flow properties and to diagnose the gas dynamic behaviour of the machine when developing new operating conditions. We describe two of the specialized flow simulation codes that we have written to assist us in our experimental work and look at the application of these codes to the expansion tube experiments.

Contents

1 INTRODUCTION **2**

2 EXPANSION TUBE FACILITIES **2**
2.1 X2 Expansion Tube 4
2.2 X3 Expansion Tube 7

3 INSTRUMENTATION **9**
3.1 Surface radiation gauges 9
3.2 Spectral measurements 11
3.3 Two Colour Ratio Pyrometry 12
3.4 Interferometry 13

[*]NASA Ames Research Center, California, USA.
[†]Faculty of Engineering and Surveying, University of Southern Queensland, Australia.
[‡]Department of Engineering Science, University of Oxford, UK.
[§]Ecolé Centrale Paris, France.
[¶]DLR Göttingen, Germany.

4 TEST FLOWS **14**
4.1 Flow over a cylinder 14
4.2 Mach Disk Flow 14
4.3 Simulation of entry into Titan's atmosphere 18
4.4 Ablation study 19
4.5 Hot wall reentry testing 21

5 SIMULATION CODES **29**
5.1 One-dimensional Flow Code, L1d 29
5.2 Multidimensional-Flow Code, Eilmer 30

6 FACILITY SIMULATIONS **31**
6.1 Commissioning a New Lightweight Piston for X2 31
6.2 Hybrid simulation of the X2 expansion tube 41
6.3 Axisymmetric simulation of the X2 shock tube 51

7 HAYABUSA RE-ENTRY OBSERVATIONS **55**

8 CONCLUDING REMARKS **60**

9 ACKNOWLEDGEMENTS **61**

1 INTRODUCTION

When a spacecraft enters an atmosphere, the free stream flow forms a bow shock ahead of the forebody, and the shock heated gas transfers heat to the body by convection and radiation. While convection can be predicted well, radiative heating predictions still have uncertainties larger than 30% when using state of the art models [1]. Super-orbital re-entry, especially, still offers a host of challenges that are being tackled through the combined efforts of computational simulation and experimental measurements. To understand the minimum requirements of a thermal protection system's heat shield material, in-flight testing is ideal. However, current opportunities for flight testing of prototype configurations are rare and far between, so experimental efforts are generally focused on laboratory simulations.

High flow speeds, in excess of 10 km/s, are required for the ground-based study of the aerothermodynamics of superorbital re-entry. The operation of a continuous wind tunnel producing the requisite flow speeds is problematic. First, it is difficult to design a facility that would bear the sustained heating rates to the tube walls for long periods and, second, the energy requirements for continuous operation are prohibitive. Impulse facilities, such as expansion tubes, are thus the machines of choice for testing at hypersonic speeds.

In Australia, laboratory simulation of super-orbital flow energies is achieved using expansion tunnel facilities located at the University of Queensland[2, 3]. These facilities are impulsive wind tunnel facilities which produce test flows with a duration on the order of 100 (and up to 500) microseconds. Actual flight conditions produce ablative flows for several tens of seconds under atmospheric conditions that are slightly different than in the wind tunnel facilities. Although recent free-piston driver developments have established new flow conditions, scaled testing of thermal protection system models is commonly employed.

2 EXPANSION TUBE FACILITIES

The concept of replacing the steady expansion of a shock tunnel with an unsteady expansion was first investigated by Resler and Bloxsom [4] in 1952. By adding to the total enthalpy of the test gas using an unsteady

expansion rather than with a shock, it was claimed that higher flow velocities, and high Mach number and Reynolds number flows could be generated. The flow was not stagnated and this in turn would mean less dissociation and ionisation. The disadvantages were a much shorter test time and development of large boundary layers in the resulting test flow. Hertzberg et al [5] were the first to apply the unsteady expansion concept by modifying a shock tunnel but Trimpi [6] in 1962 performed a more detailed theoretical study and was the first to coin the term 'expansion tube'. NASA investigated the use of expansion tubes in the 1960's and 70's and highlighted a number of discrepancies between theory and experiment [7]. In particular there were problems with flow attenuation, secondary diaphragm rupture, flow turbulence, interface mixing, boundary layer thickness, thermal non-equilibrium and test time. After many investigations the expansion tube at NASA Langley was deactivated since only one usable condition for each test gas was obtainable for model testing.

Currently, the largest expansion tube in the world is the Lens-XX at the Calspan-University of Buffalo Research Center (CUBRC) in New York State [8, 9]. It has a nominal operating range of 3–12 km/s and has been used to generate test flows at 10 km/s for radiation measurements [10].

Expansion tubes at UQ

Expansion tube research began at The University of Queensland in 1987 when Paull et al [11] converted the small shock tunnel, TQ, to an expansion tube by directly connecting the driver to the shock tube. This facility, reconfigured by Morgan [12, 13] and renamed X1, used multiple diaphragm sections to create the compound driver and to generate super-orbital capabilities. Investigations by Paull and Stalker [14] into test gas disturbances and research at GASL [15] finally determined that by using blends of nitrogen, argon and helium as the driver gas the perturbations could be reduced and many more conditions could be achieved. The successful driver gas blends sufficiently increased the speed of sound over the driver/test gas interface which was shown to limit the penetration of driver gas noise into the test gas.

In 1995, the X2 free-piston-driven expansion tube was commissioned at The University of Queensland [16]. The two-piston configuration was chosen to reduce the cost of the high pressure primary driver section, which increases greatly with diameter. This decision was taken in the knowledge that it would give reduced performance and increased complexity in order to build the largest driven tube diameter possible with the funds available at the time. It was the prototype for a larger expansion tube, X3, which was subsequently commissioned in 2001.

Application to superorbital experiments

In expansion tube mode, experiments are performed on subscale models of aeroshell configurations as shown in the upper part of Figure 1. Because the models in the experiment are scaled, the flow conditions also require appropriate scaling to maintain similarity between the experiment and the true flight conditions. Typically, the product of density and length is kept the same as for the full scale vehicle and, although this provides similarity for some aerothermodynamic processes such as chemical dissociation, the radiative energy exchange scales differently.

To fully replicate the chemical, and radiation, processes requires real flight densities. In the expansion tube facility, we generate an abstract flow situation such that the full shock layer conditions can be replicated without needing the full scale model. This is done by generating a conical converging shock that terminates in a Mach disk, located in the middle of the test section. Section 4.2 describes the arrangement more completely.

Alternatively, the facility may be operated in nonreflected shock tube mode. When using nonreflected shock tube mode, there is no subscale model placed in the test flow. Instead, the object of observation is the relaxing flow immediately behind the shock as it propagates into the test gas. It is helpful to think of this type of experiment as observing the bow shock that is driven by the aeroshell. There is no actual aeroshell

driving the shock, rather just high pressure gas generated in the shock tube. This direct observation of a passing shock layer in nonreflected shock tube mode is shown in the lower part of Figure 1.

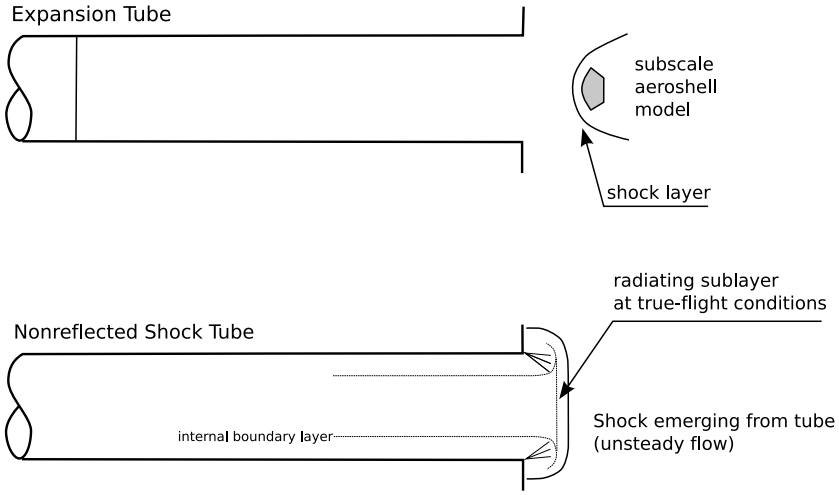

Figure 1: Schematic representation of types of experiments performed for the study of radiating blunt body flows.

2.1 X2 Expansion Tube

Figure 2 shows a photograph of the X2 hardware in the UQ laboratory and a schematic overview of the full facility, from compressed-air reservoir through to the combined test section and dump tank at the downstream end.

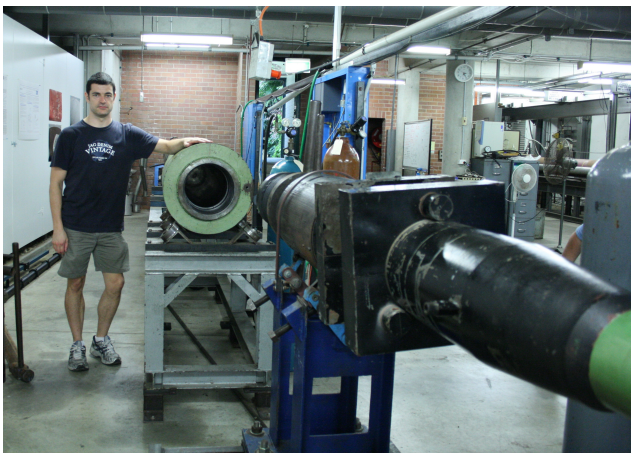

(a) David Gildfind with the X2 facility. Downstream tubes are in the foreground of the photograph.

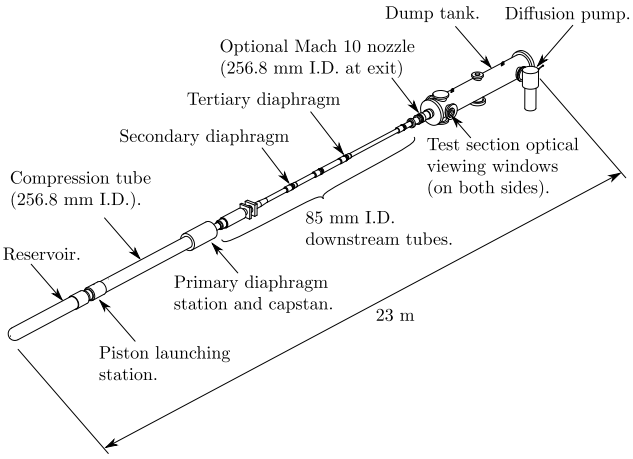

(b) Overview of the X2 facility with Mach 10 nozzle [17].

Figure 2: X2 superorbital expansion tube facility.

Figure 3 shows a schematic of the X2 facility and a wave diagram of the flow process. The representation in Figure 3 corresponds to use of the facility in expansion tunnel mode. The test gas which eventually passes

over the model (or in this diagram, the Pitot rake), initially resides in the shock tube. The gas initially at rest in the acceleration tube is called the accelerator gas.

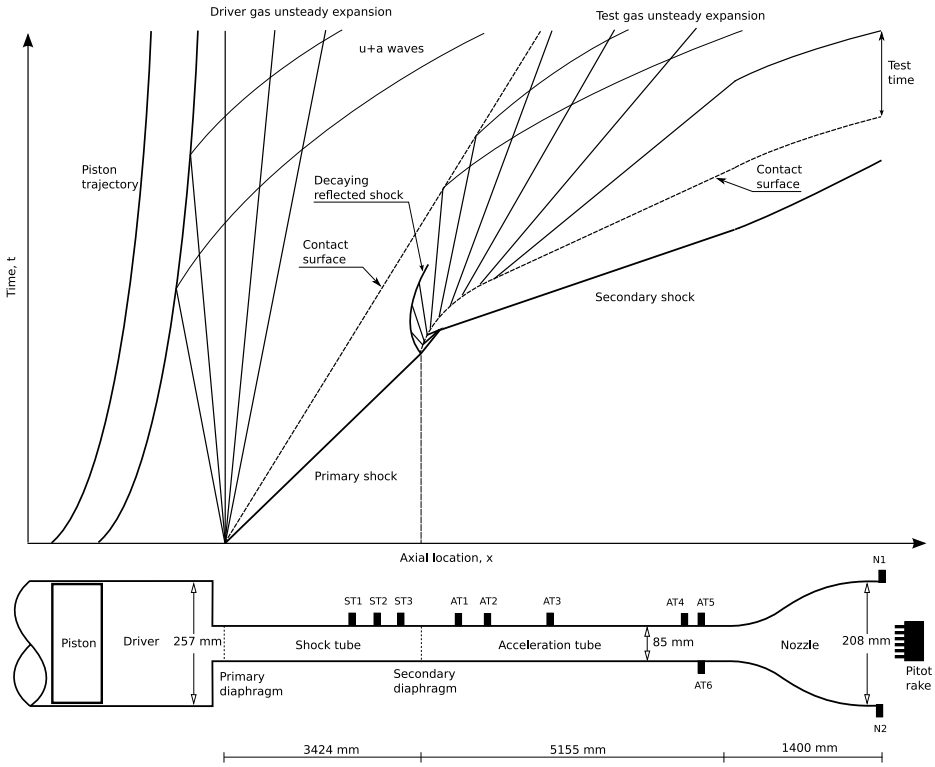

Figure 3: A schematic of the X2 facility configured for expansion tunnel operation. A wave diagram, or (x,t)-diagram, shows the flow process. [18]

In the diagram, $t = 0$ corresponds to the rupture of the primary diaphragm; at this point the 35 kg piston is nearing the end of its stroke. The primary diaphragm is made of mild steel. Its thickness is varied according to the desired rupture pressure. The rupture of the diaphragm produces a shock, labelled the primary shock. This shock travels through the shock tube compressing and accelerating the test gas. The secondary diaphragm is only very light and so ruptures when the primary shock arrives. The secondary shock propagates into the acceleration tube, its faster speed a consequence of the lower density medium. The compressed test gas now expands, in an unsteady manner, into the acceleration tube. This expansion process drives the low pressure accelerator gas before it. This interface between test gas and accelerator gas is labelled as the contact surface. The test gas expansion is controlled by the pressure of the accelerator gas; a lower pressure accelerator gas results in a stronger expansion. The steady test time, as indicated in Figure 3, is limited by the arrival of a $u + a$ wave from the centred expansion.

Many high enthalpy conditions benefit from operation of the expansion tube with a shock-heated secondary driver [19]. This is a volume of helium contained at the beginning of the driven tube, between the primary diaphragm and the test gas, and requires the use of a second thin Mylar diaphragm. The secondary driver provides additional shock strength for high enthalpy conditions, but is also used for relatively low enthalpy scramjet conditions to prevent corruption of the test flow by acoustic disturbances originating in the free-piston driver, a noise mechanism originally identified by Paull and Stalker [14]. For further details about the principles of expansion tubes see Reference [13].

Numerical simulations aid the expansion tube testing by estimating a full set of flow properties that are not directly measurable. For example, numerical simulations help to establish the set of flow conditions in

the test gas when operated in expansion tunnel mode. This is important because these are the flow conditions which form the free stream flow for the subscale model; subsequent analysis of the experiment depends on reliable estimates of the free stream flow conditions. An example simulation for a condition in the X2 facility, operated in expansion tube mode, is presented in Section 6.2. This simulation targets the 25 MJ/kg CO_2–N_2 operating condition developed in Reference [20] to obtain spectrally resolved radiation intensity measurements of the recompression shock formed over a finite cylinder.

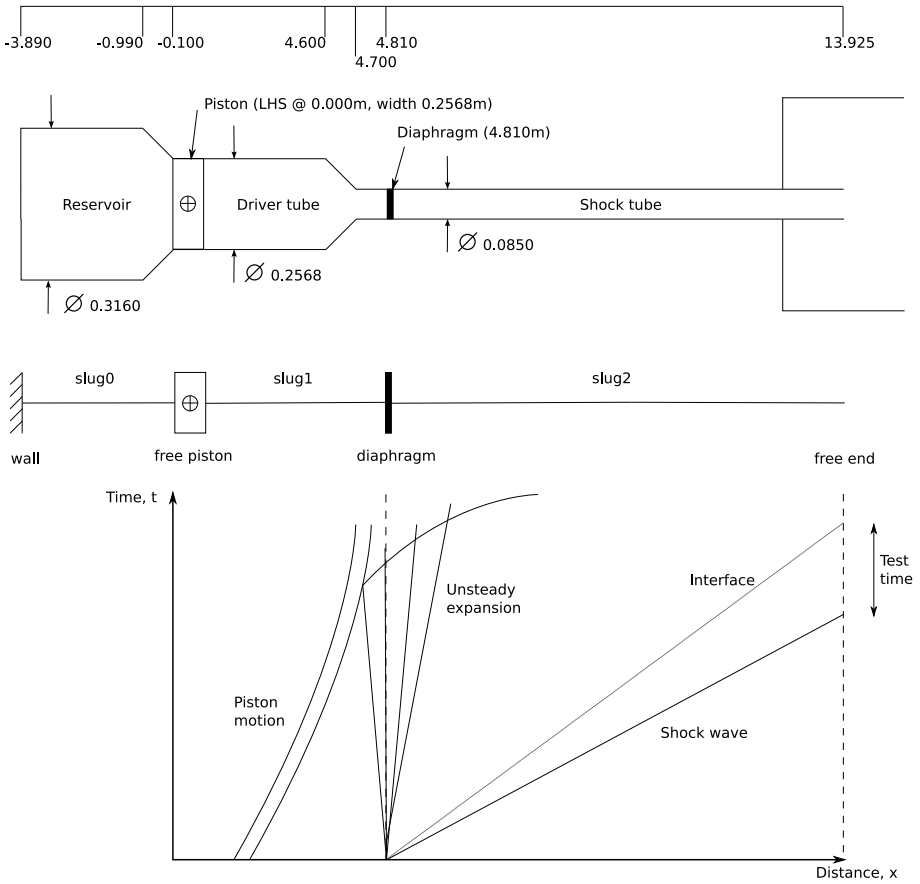

Figure 4: A schematic of the X2 facility configured for nonreflected shock tube operation. A wave diagram shows the flow process.

The X2 facility is operated as a conventional shock tube when used in nonreflected shock tube mode. Figure 4 shows a schematic of the facility and a wave diagram for the flow process. Prior to $t = 0$, the piston compresses the driver gas which is often a mixture of helium and argon. The rupture of the diaphragm corresponds to $t = 0$ in Figure 4. After diaphragm rupture, the shock then propagates into the shock tube which contains the test gas. The experiment involves making optical measurements of the radiating flow as the shock emerges from the shock tube and into the test section.

The section of the flow labelled test time in Figure 4 distinguishes this mode of operation from the expansion tunnel mode: for the nonreflected shock tube mode, the gas immediately behind the primary shock is of interest whereas for the expansion tunnel mode, the test gas has been previously “gathered up” in the shock tube and allowed to expand in the accelerator tube. In the experiments using nonreflected shock tube mode only a small portion of the test gas is of interest, namely, the nonequilibrium radiating gas immediately behind the shock.

2.2 X3 Expansion Tube

The X3 facility, in its current configuration [21], is a much larger facility than X2 and is shown schematically in Figure 5 without the final expansion nozzle. The principal benefits of building a large machine are the increase in test slug length and larger core flow diameter achieved in the test section.

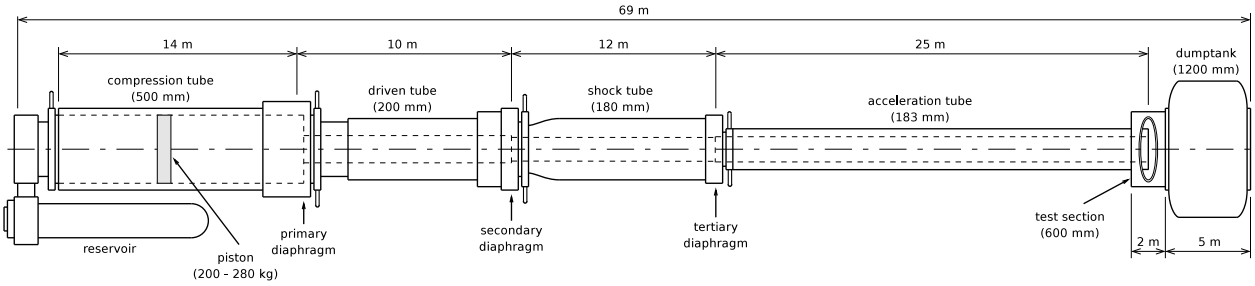

Figure 5: Schematic layout of the X3 superorbital expansion tube [2].

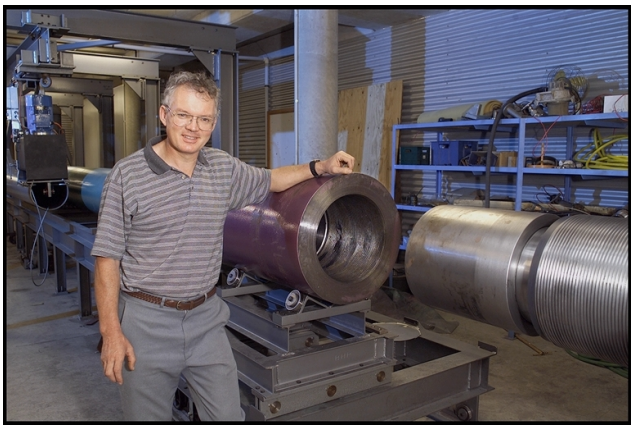

(a) Richard Morgan with the X3 facility.

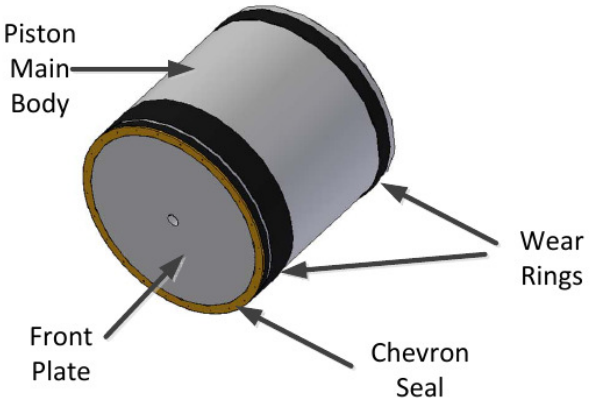

(b) Single-stage piston [21].

Figure 6: Principal drivers of the X3 facility.

A schematic of the piston arrangement is shown in Figure 6b which illustrates the single large diameter piston which is constructed from aluminum and has a diameter of 498 mm and a length of 520 mm. A chevron seal attached to the front of the piston creates the seal to the compression tube inner diameter of 500 mm. Low friction wear rings, front and back, allow the piston to slide within the compression tube. The front plate is flat and the inner part of the piston is hollow with attachment points to add more mass to the piston if required. When tuned correctly, the piston will now come to rest with minimal impact on a nylon rod buffer thus ensuring that the maximum amount of energy is transferred to the driver gas.

The addition of a steady expansion nozzle to the end of the acceleration tube (thus operating in expansion tunnel mode) has three main benefits: increased test core flow diameter; slight increase in test time from use of gas in the unsteady expansion fan; and avoidance of viscous corruption of test flow for low enthalpy true flight scramjet conditions. This comes at the cost of density-length capability and a reduction in the total pressure/total enthalpy multiplication achieved through the test gas unsteady expansion for a targeted test flow Mach number. However, with a high performance driver like that implemented on X3, these losses in capability can be easily overcome for most conditions.

The Mach 10 steady expansion nozzle (Figure 7a) was manufactured by Teakle Composites. It consisted

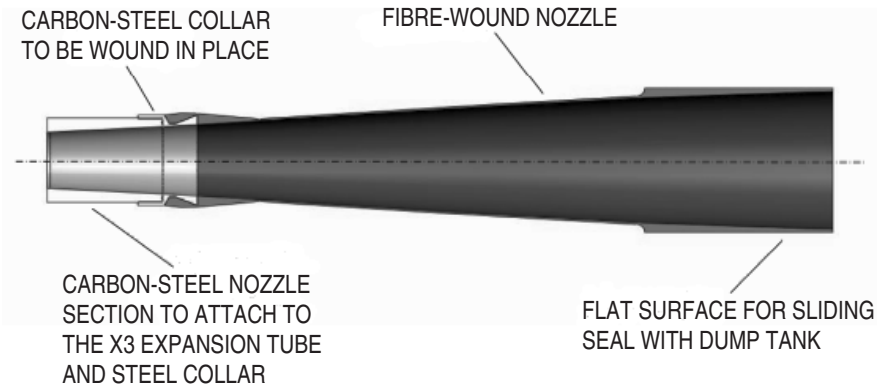

(a) Final expansion nozzle [22].

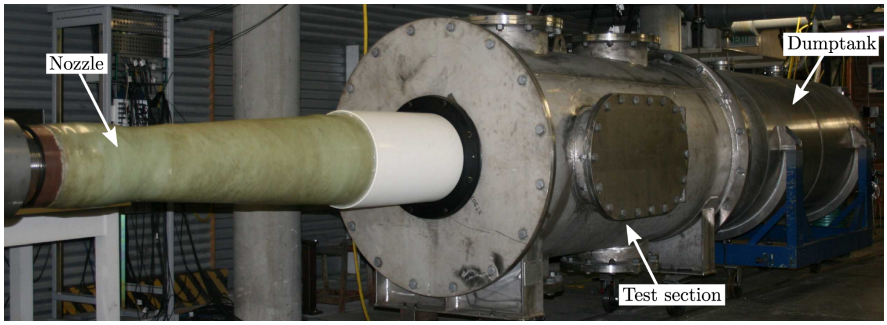

(b) Nozzle, test-section and dump-tank [17].

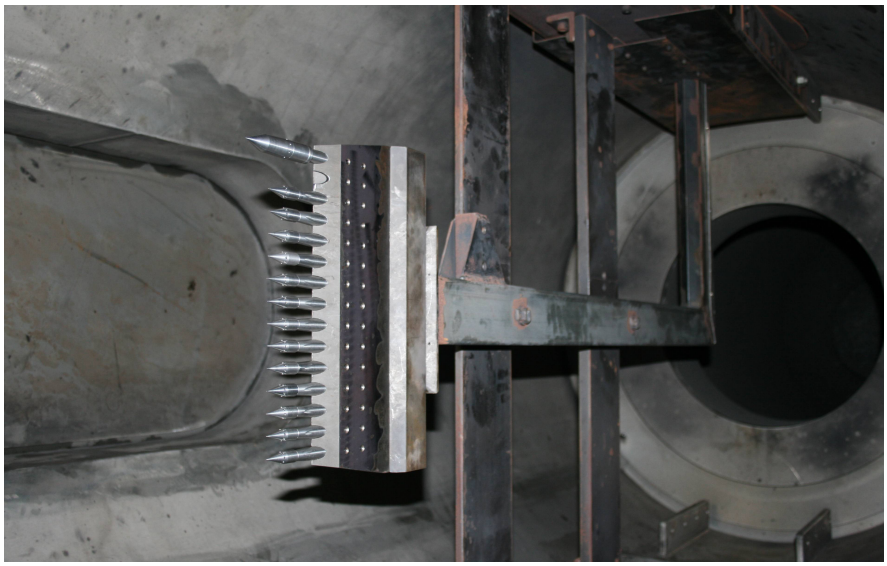

(c) Pitot probes in test section [17].

Figure 7: Nozzle, test-section and dumptank of the X3 facility.

of three main components: steel attachment components for connection to the acceleration tube, a filament-wound nozzle and a sliding seal. The steel components for attachment to the acceleration tube consisted of two parts. A carbon-steel nozzle section allowed attachment to the existing acceleration tube which in turn threaded on to a carbon steel collar and fiber-attachment point. The glass fiber was wound directly on to the collar to provide a mechanical lock and pressure seal. The filament-wound nozzle (Figure 7b) was made from a glass fiber and an epoxy resin with a minimum thickness of 5 mm to maintain structural integrity and prevent through-gassing. It was wound on to a high density polyurethane mandrel which had been machined to the required contoured profile. To create the constant diameter sliding seal, an additional winding was made at the nozzle end and finished with a gel coating. The nozzle has a total length of 2.5 m and increases the flow exit diameter to 440 mm from the existing acceleration tube exit diameter of 183 mm.

A photo showing the assembled Mach 10 nozzle, test section and dump tank is shown in Figure 7b. The test section provides increased space for large scale models and multiple viewing and data ports. The standard diameter of the test section is approximately 1200 mm with a length of approximately 2500 mm and was constructed from 304 stainless steel. Together with the dumptank, the effective test section/dumptank volume is over 6.2 m^3.

The interior of the test section is shown in Figure 7c. A Pitot rake is mounted in the test section to allow measurement of nozzle exit pitot pressures at radial spacings of 20 mm. The Pitot probe tips are a new design consisting of a 15° cone tip. Following recent experimental testing of high total pressure scramjet conditions in X2, it was found that the bow shock associated with normal Pitot measurements led to erosive heating damage. The cone probe was thus developed to provide a partial impact pressure measurement. The static pressure on the cone surface is measured with these probes and while this is not a Mach number independent measurement, sensitivity to Mach number reduces for Mach>>5. If the Mach number of the flow is approximately known, this cone pressure can be relatively easily correlated to actual Pitot pressure or an equivalent metric in CFD. Large optical viewing ports were constructed in the test section and one of these is visible on the left in Figure 7c although it is not fitted with an optical window at this stage.

3 INSTRUMENTATION

3.1 Surface radiation gauges

Radiation gauges have been developed using thin film heat gauges mounted behind a viewing window, where the window separates the convective heating from the radiative heating. An improved version [23] of Capra's radiation gauge [24] has been designed, manufactured and tested. The emphasis for the new design was improving the calibration procedure of the gauges, as well as redesigning the optical black coating to maximize the signal measured.

The new radiation gauges, as seen in the microscope image in Fig. 8a, consist of a thin film heat gauge that was manufactured out of 2 mm quartz rods cut to 5 mm length pieces. Two gold tabs were hand painted on the quartz substrate to create connections for the nickel sensing element, which was then sputter coated onto the polished quartz face. The exposed nickel strip is approximately 1.0 mm x 0.3 mm x 0.1 μm in size. Insulated wires were soldered to the gold tabs for connections to the external electronics. The thin film heat gauges were then calibrated, and placed in a brass housing mount that allows the gauge to be mounted behind a fused silica viewing window (4mm dia. 2mm thickness).

Calibration

Recently, the gauges were used in experiments on Titan atmospheric entry conditions, where the radiation was expected to be dominated by CN violet. Preliminary experiments in X2 with the new Titan conditions

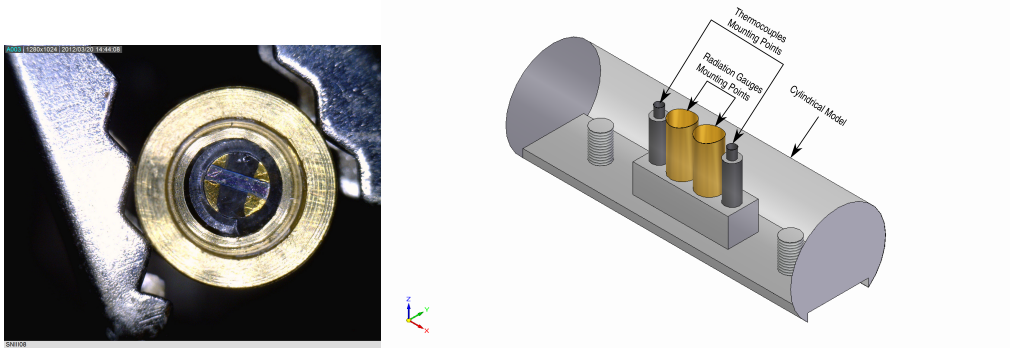

(a) Radiation gauge (b) Mounting in a cylindrical model

Figure 8: Radiation gauges and their application in a bluff body model [23].

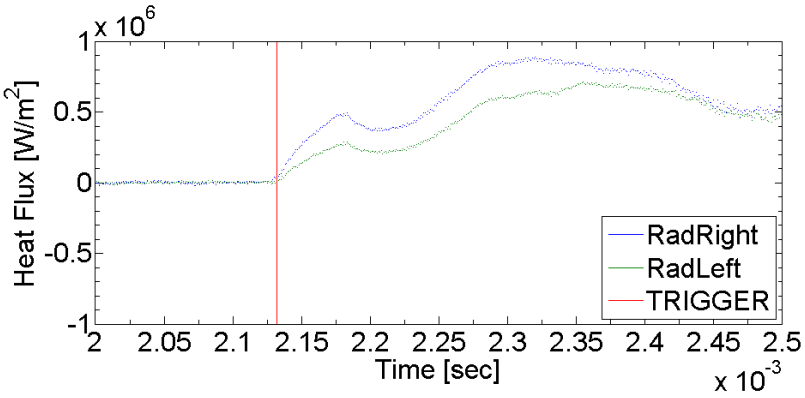

Figure 9: Signal from uncalibrated radiation gauges, heat flux during Titan 6.5 km/s condition, shot x2s1786 [25].

confirmed that the radiation gauges are sensitive enough to respond to this level of radiation at the short test time. These tests were conducted using two uncalibrated gauges, mounted on a cylindrical model. Uncalibrated results from the radiation gauges for a 6.5km/s Titan condition are presented in Figure 9.

Of special importance is the sensitivity of the gauges in the part of the spectrum dominated by the CN bands (357-418nm), and a new calibration technique has been set up for this purpose. Capra [24] performed an indirect calibration of the gauges. Using a welding arc, the gauges were exposed to the same conditions with and without black paint coating and the difference in the measured values were compared with experimental data available for the amount of heat absorbed by black paint application. After achieving good agreement, the theoretical value was used. Capra outlined a method that was not available at the time but is the ideal way to properly calibrate the gauges by generating the three wavelengths of interest (357, 386, 418nm which correspond to CN radiation peaks) with known intensities, using a laser.

The new calibration procedure uses high power narrow wavelength band light emitting diode (LED) instead of a single wavelength laser. Three commercially available LEDs where identified as potentially suitable, covering the wavelength range between 365-404nm, and a 383nm peak wavelength LED was used in the preliminary study. A 9W LED chip NC4U134A from Nichia was sourced, and a photomultiplier tube (PMT) was used to verify the peak wavelength of the 9W LED.

A radiation gauge was connected to an amplifier, and the response to the LED light was recorded by a data acquisition system, allowing the calculation of the heat flux sensed by the gauge. All the gauges were

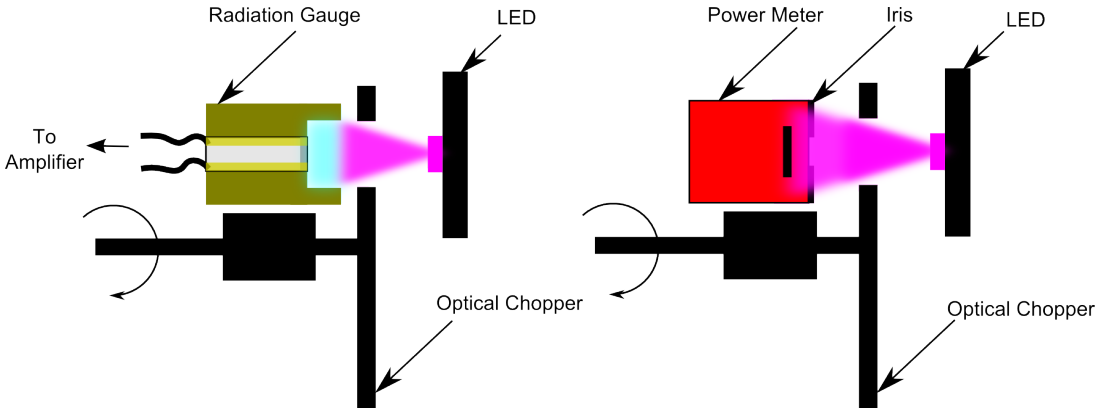

(a) Setup I (b) Setup II

Figure 10: Radiation gauge calibration (not to scale) [25].

coated with an antireflection coating that can vary from one gauge to another and the aim of the calibration is to account for these differences by calibrating each gauge independently for radiative heating in the band of 380-390nm. The calibration procedure developed compromises of two stages. At the first stage illustrated by Figure 10a, a radiation gauge is connected to an amplifier, and the response to the LED light is recorded by a data acquisition system. An optical chopper was designed to expose the calibration source for short periods of time. The radiation gauges tested showed good responses to the LED, with amplification between 100-2000 depending on the gauge. The data gathered is then used to calculate the heat flux sensed by the gauge, and is then compared to the heat flux that was measured by the power meter.

After measuring the heat flux detected by each gauge at a fixed distance away from the LED, the second stage utilises a power meter (Thorlabs s302c), placed in the same location behind a small aperture (Figure 10b). The measured power is then converted to heat flux, and compared with the detected heat flux per gauge, completing the gauge calibration for the waveband. To date, only preliminary analysis of such data was conducted, and further development of the calibration method may be necessary to ensure each radiation gauge can be calibrated easily.

3.2 Spectral measurements

Figure 11 illustrates the layout of the optical instruments used to probe the characteristics of the shock and ablation layers in the expansion tube tests. Luminosity from substantial portions of the model and shock layer flow is visualized using a Shimadzu HPV-1 high speed CCD video camera. The HPV-1 was positioned on a raised mount above the horizontal plane passing through the tunnel centre line. The model was imaged using the HPV-1 without blocking the field of view of the UV spectrometer using an elevated, flat aluminium turning mirror.

For the Hayabusa model, radiation from chemical species in a narrow, 3.9 mm long strip of the field of view parallel to and including the stagnation streamline was spectrally resolved using an Acton Research Spectro Pro 2300I spectrograph. Spectra were collected across this window over a 10 μs interval during the steady test time of the flow. The upper spectrometer in each of the figures utilizes a 0.3 m UV/Visible spectrograph with a diffraction grating coupled to a Princeton Instruments PI-max intensified CCD camera. Diffraction gratings with 150, 600 and 1800 line/mm are used. The mirrors used in the optical path between the flow and the spectrograph were UV enhanced aluminium.

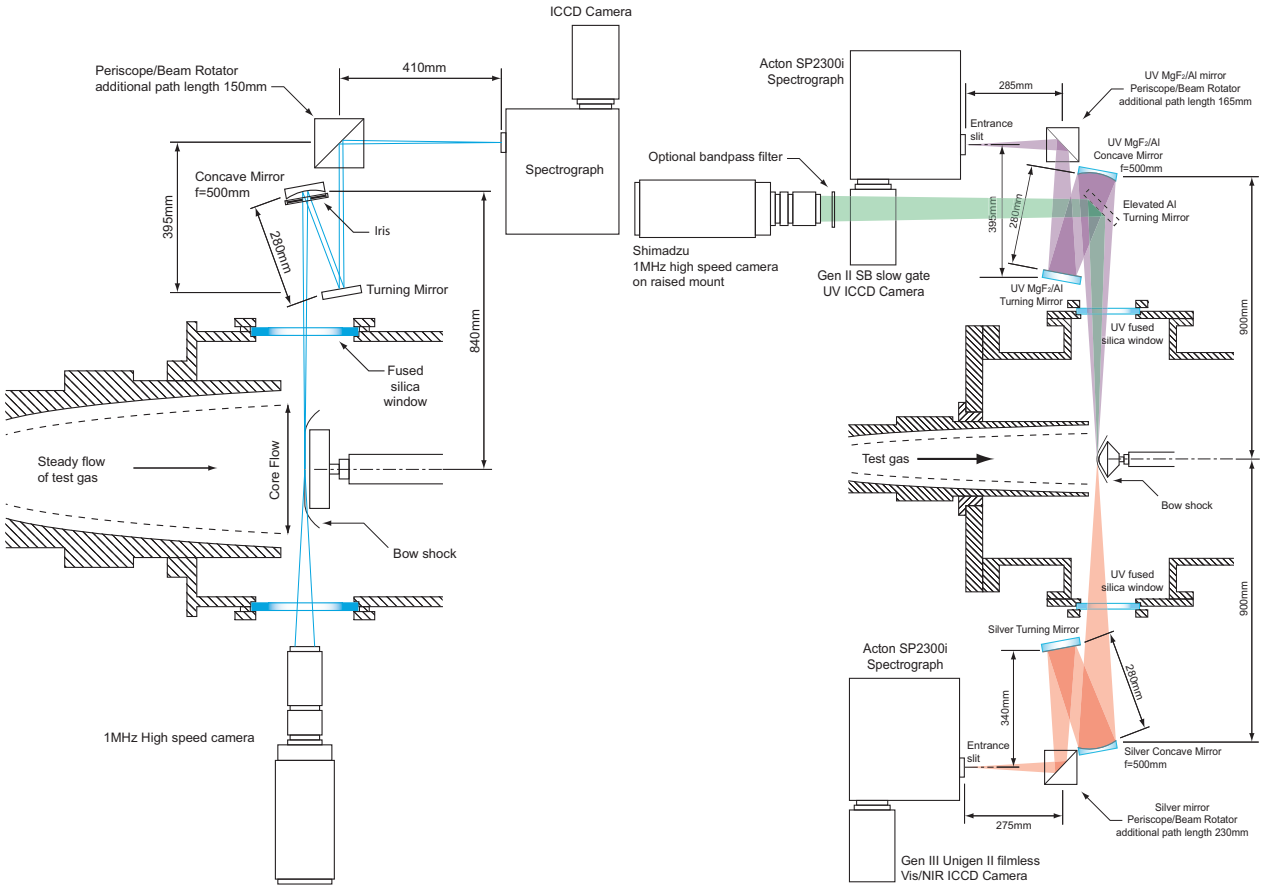

(a) Cylinder with only the UV spectrometer.

(b) Hayabusa model with both spectrometers.

Figure 11: Schematic arrangements for the optical access to blunt-body shock layers [26].

Calibration

The ICCD detector attached to the spectrometer records a signal in counts which is related to the amount of radiation being emitted from the hot gas in the shock layer over the model. This signal is converted into a spectral radiance by a calibration procedure which takes into account the sensitivity of the detector, the collection efficiency of the optics and losses due to optical components. The first step in this process is to convert the counts to a spectral irradiance (W/m^2/nm) by comparison with a signal recorded using a calibrated source placed in front of the spectrometer. Losses due to the window and the reflectivity of mirrors are taken into account. From a knowledge of the imaging optics and the limiting aperture in the system, the spectral irradiance is converted to a spectral radiance (W/m^2-nm-sr) emitted by the hot test gas in front of the model.

3.3 Two Colour Ratio Pyrometry

Most of the models tested in expansion tubes have been at room temperature before testing and so have had cold surfaces for the short duration of the test flow. Section 4.5 describes some recent experiments [27] in which the model surfaces are heated to temperatures above 2000 K before the arrival of the test flow. In order to define the conditions under which the testing is taking place, it is necessary to know the temperature of the model surface as the flow arrives. The regular methodology for measuring a spatially resolved surface temperature is using infrared pyrometery, however this equipment was not available at the time of testing so an alternative was required. The alternative found to be suitable was using a two colour ratio pyrometric

(TCRP) technique which can be implemented with a standard commercially available digital SLR camera. This technique has previously been successfully used to measure spatial temperature distributions for various applications and is described in detail by Ma [28].

Regular pyrometry relies on the measurement of the absolute intensity at a particular wavelength which can be equated to a temperature of the emitting body. This method is very accurate however it does require expensive, highly calibrated equipment. TCRP does not require an absolute measurement of intensity, instead relying on the ratio of intensities at two different known wavelengths. The selected wavelengths can be chosen arbitrarily as long as they are known and can be measured. Digital cameras fulfil this role by capturing red, green and blue wavelength intensities which are required for recreating images as seen by the human eye. The CCD or CMOS sensor is comprised of an array of red, green and blue pixels which capture the intensity over specific wavelength regions. By capturing this data from an image the two colour ratios can be used to calculate a temperature for each pixel. For this analysis the model being imaged is assumed to be radiating as a grey body, i.e. constant emissivity, and this assumption is supported by the research of Balat-Pichelin [29] for carbon-carbon materials in near vacuum conditions.

3.4 Interferometry

Interferometry can be used to measure density, ionization levels, species concentrations and temperatures. In particular, two-wavelength holographic interferometry has been used in the X2 expansion tube flows [30].

A Nd:YAG laser can be used to generate a light beam consisting of 355 and 532 nm components formed to propagate collinearly. The beam is divided into two separate paths, the recording and test beams, each containing both wavelengths. The recording beam passes above the tunnel using periscopes and is then expanded to illuminatethe holographic plate. The testbeam is expanded to fill the test section windows and pass over the model. Lenses are then used to image the model onto the holographic plate. An aperture can used at the focus of the beam to remove flow luminosity, particularly in the high-temperature region in front of the bluff body under test.

To perform interferometry, it is necessary to record no-flow and with-flow holograms. To achieve this, the laser is triggered once before tunnel operation and once during the test time. This creates four holograms, which, when reconstructed, generate two independent interferograms, corresponding to the two wavelengths. Finite fringes are added to the image by slightly tilting one of the mirrors in the recording beam between exposures. Finite fringes allow processing of the interferogram using Fourier transform methods and allows quantitative data to be extracted The interferograms are separately processed to yield phase distributions, which can be combined to determine the density and electron concentration. Under the assumption of chemical and thermal equilibrium, the density and electron concentration are linked by the Saha equation, such that temperature can be estimated numerically.

4 TEST FLOWS

4.1 Flow over a cylinder

The results [31] of the two-wavelength holographic interferometry measurements for four cylinders in a 10 km/s flow are shown in Fig. 12

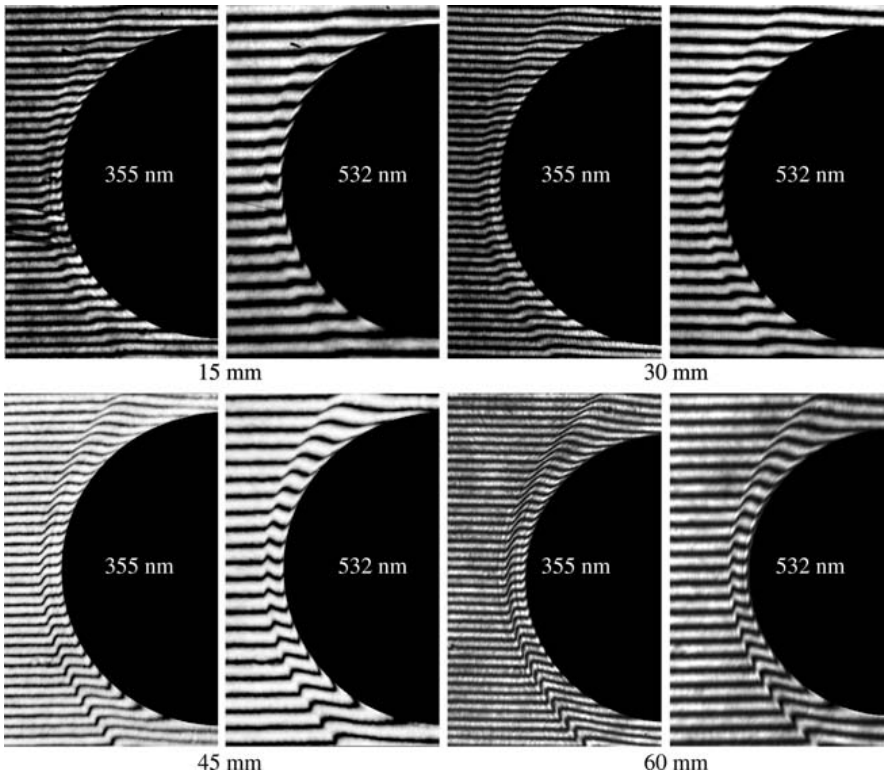

Figure 12: Shock shapes around various cylinders images using two-wavelength holographic interferometry [31].

In these interferograms, an increase in density produces an upwards-going fringe shift while the formation of free electrons creates a downwards going fringe shift. The wavelength dependence of the refractivities means that heavy particles produce larger fringe shifts at lower wavelengths while electrons have a bigger effect at longer wavelengths. In each interferogram, there is a positive (upward) going fringe shift in front of the body indicating the location of the shock front. Particularly noticeable in the 532 nm image for the 60 mm long cylinder is a negative (downward) going shift just behind the shock front indicating the onset of ionization.

4.2 Mach Disk Flow

The flow design that we introduce here is a new method of creating the normal shock, physically similar to a 'bow' shock, without the need for a vehicle body. This therefore eliminates the need for the excessively large models required to create the shock stand off associated with the real flight densities. This allows the study of the non-equilibrium region behind the shock all the way through to equilibrium.

The design theory for these geometric models is taken from hypersonic inlet design conducted by Molder [33]. This design process uses the Taylor-Maccoll equations to create a contoured wedge ring which, for an ideal gas, produces a perfectly straight conical shock impinging on the centreline as shown in Fig. 13a.

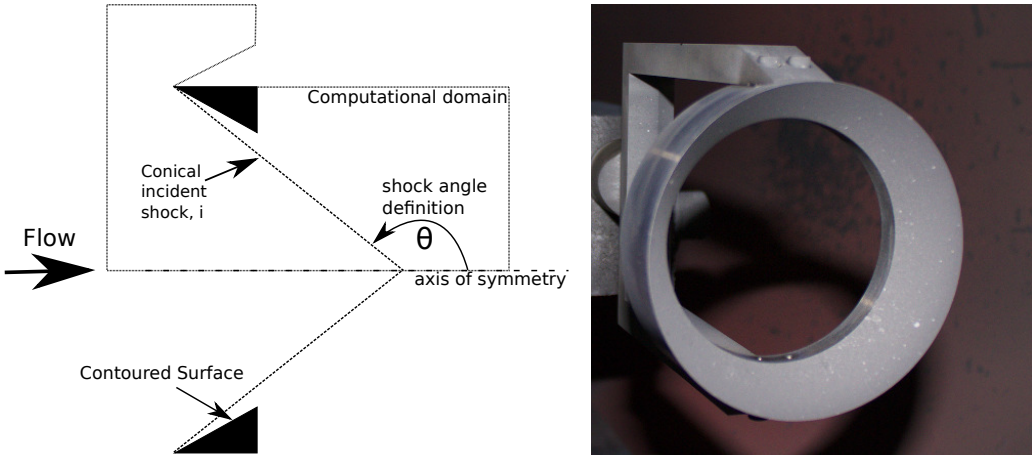

(a) Schematic of generator (b) Mounted in the X2 facility

Figure 13: Geometric configuration of conical shock generator. [32]

The design of the contoured wedge is dependent only on the Mach number of the flow and the desired shock angle (as defined in Fig. 13a) for any given ideal gas.

Due to the mass flow of gas being processed by the shock structure, this perfect regular shock reflection is not possible and a Mach reflection is formed at the centreline. The resulting structure of the Mach reflection is shown in Fig. 14a. It is the formation of the Mach stem and the flow downstream of the Mach stem that are of interest.

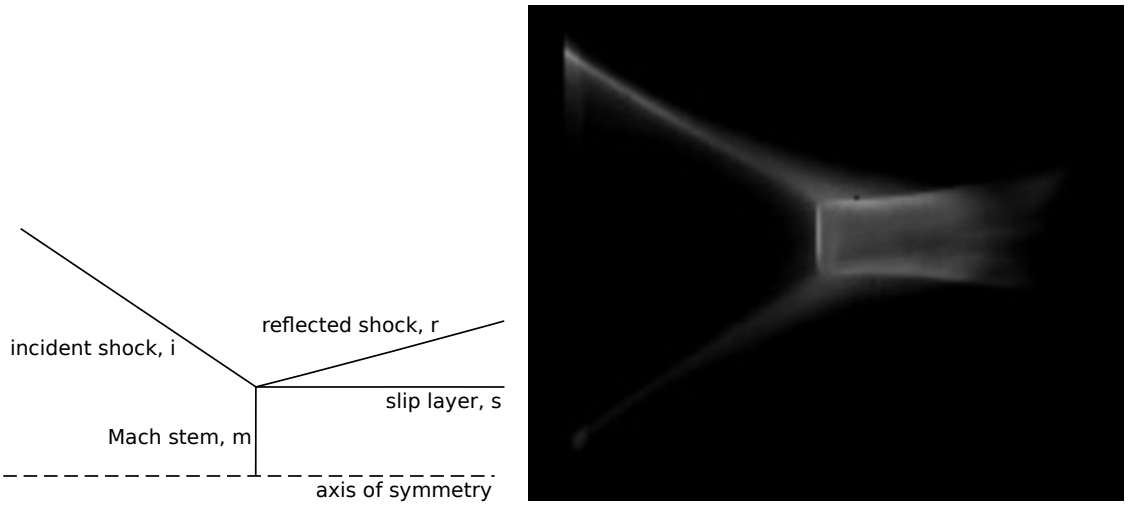

(a) Schematic view (b) Video frame

Figure 14: Mach reflection shock structure of Mach 10 air test flow in the X2 expansion tube. [32]

The Mach disk is essentially a normal shock formed in the free-stream flow similar to that which is created in the stagnation region of an atmospheric (re-) entry vehicle. This allows the study of the physio-chemical processes behind the shock representative of what would be seen on a flight vehicle. This is generally not directly possible in these facilities using a blunt body model as the required length scales of the model are not achievable (for true flight density). Another advantage is that the model is in front of the shock structure such that it does not interfere with the downstream flow development. With blunt body models, the usable flow length is limited by the shock stand off distance from the model.

The inclusion of the high temperature gas effects further complicate the flow structure due to the energy absorption of the gas chemistry. This effect causes the conical design shock to curve downstream and greatly change the shock structure on the axis.

Figure 13b shows the model mounted in the X2 facility during the testing campaign. The ring has a diameter of 100 mm and is positioned centred on the nozzle approximately 10 mm downstream from the exit plane. This ensures that the entire model is captured completely in the core flow of the facility.

During the testing, the flows were visualised using a Shimadzu HPV-1 high speed camera and during some testing a UV spectrometer was also utilised for spectral measurements. This initial testing was primarily for proof of concept and hence more detailed measurements have not been taken at this stage. The luminosity imaging using the HPV-1 was sufficient to demonstrate the Mach disk formation in the targeted flow.

Figure 14b shows a still extracted from one of the air tests. This clearly shows the expected shock structure and in particular the formation of the Mach disk. From the luminosity imaging, the shock structure appears to be reasonably steady. This is more apparent in the Titan test gas where the luminosity is due to the gas chemistry rather than the aluminium contamination, as is presumed with the air flow. This image has also been compared with the CFD results to verify the prior analysis and the result of this is shown in Fig. 15. With the exception of the upstream convex Mach disk seen in the CFD, the results show good agreement. The conical, converging shock is well matched and the following shear layers are also closely matched.

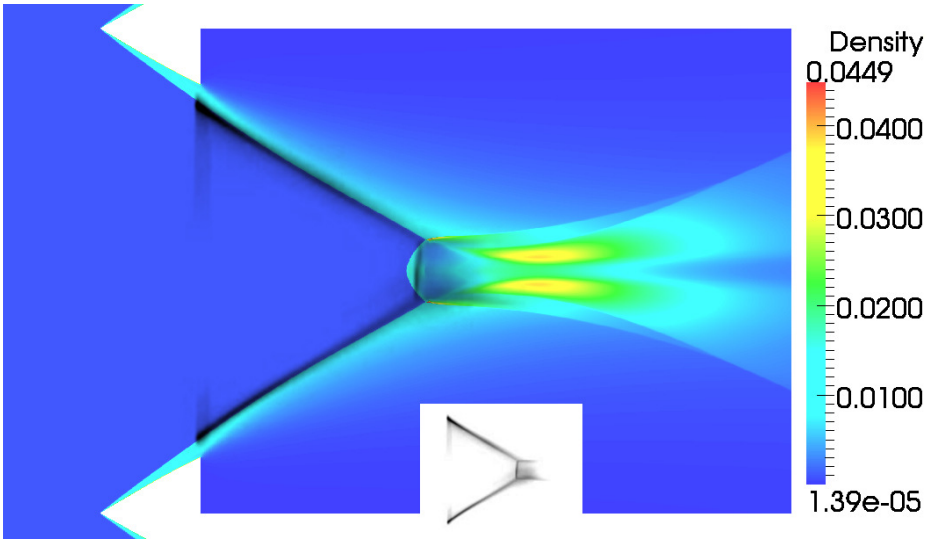

Figure 15: A comparison of the luminosity imaging (black and white) with the CFD calculation (colour). [32]

The computational formation of the upstream convex Mach disk may be explained by the flow startup features seen in Fig.16. This montage shows some upstream jetting occurring during the startup processes of the flow, including the temporary formation of the upstream bulging Mach disk. It is possible that this startup feature is maintained by the numerical diffusion in the CFD close to the geometric singularity at the flow axis.

Spectral Results

The initial testing did not concentrate on getting spectral data, however, some sample data was recorded for proof of concept purposes. An Acton SpectraPro SP2358i spectrometer with a Princeton Instruments PI-MAX UltraViolet sensitive camera was used. A quasi-one-dimensional slit spanning across either side of

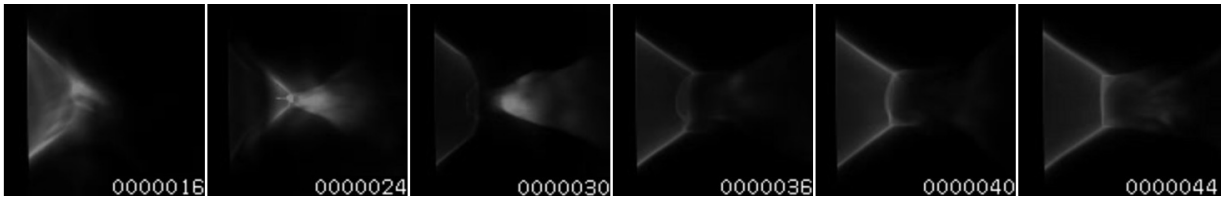

Figure 16: Flow start process captured by high speed video for the Mach 8 air condition. [32]

the Mach disk was imaged as shown in Fig. 17a. For this testing, the exact location of the Mach disk on the slit was not calibrated, however, for later testing this would be positioned differently to fully capture the post normal shock relaxation effects.

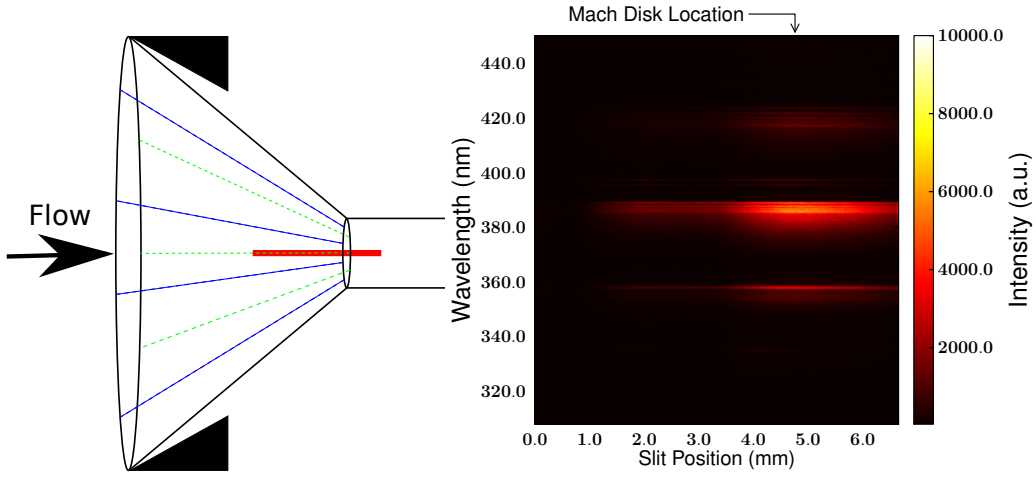

(a) Sampled region indicated in red.

(b) Flow left to right.

Figure 17: Sample UV spectrum from a Titan gas test. [32]

A representative, uncalibrated spectral result is shown for a Titan test conducted with the Mach disk configuration. Figure 17b shows the full spectra measured, with the flow from left to right. There is no spectral data visible where the ring model is obscuring the view of the flow($<$1 mm), then there is a steady increase in radiation towards the peak radiation location at approximately 5 mm (in a slit frame of reference). This slow build up of measured radiation intensity is caused by the conical converging shock that is being imaged approaching the Mach disk. Behind the Mach disk the measured intensity then reduces towards the end of the slit.

This is shown more clearly in Fig. 18, which is the spectral intensity for a single wavelength. There it is also noticeable that the radiation decreases with distance which is the relaxation occurring behind the normal shock.

The spectral results shown, although preliminary, give an indication of how this technique might be used to investigate the flow region behind a normal shock. Careful consideration is required in regards to the axial symmetry of the flow that is being visualised / measured, however it should be possible to account for this using the Abel transform. This would require incremental measurements using a radially-aligned spectrometer slit, however, the result should be an axially well-resolved species distribution behind the normal shock. This should prove to be very useful for verifying models of the post shock relaxation processes that can then be applied to other situations.

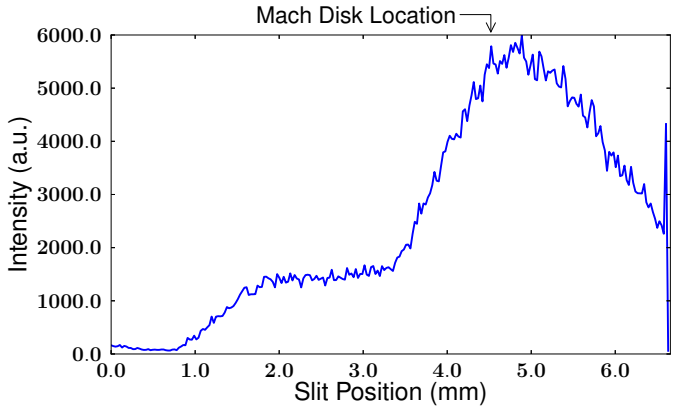

Figure 18: Spectral intensity for single wavelength, $\lambda = 386.3$ nm (flow left to right). [32]

4.3 Simulation of entry into Titan's atmosphere

For atmospheric entry into Titan (a moon of Saturn) radiation heat transfer is responsible for a large portion of the heat load at relatively low entry speeds when compared with Earth entry. This is caused by the carbon content in Titan's atmosphere, in the form of methane. The methane dissociates in the bow shock layer and combines with atmospheric nitrogen to form CN. The CN is expected to produce 99% of the radiation in the shock layer. These processes are currently poorly understood, and are not exclusive to Titan atmospheric entry. The CN is a strong radiator that dominates the radiative heating into the atmosphere of Mars as well.

Expansion tunnels are an effective technique to produce hypervelocity entry flows typical of Titan atmospheric entry, enabling the study of radiative heat transfer. New conditions for peak heat transfer at the stagnation point of a cylindrical model with an entry velocity of 6.5km/s have been developed and validated with a pitot survey. Preliminary measurements of heat transfer were made using radiation gauges and emission spectroscopy, in an effort to demonstrate their applicability.

The test gas is a mixture of 95% Nitrogen and 5% Methane. A 25 mm diameter cylindrical model of 75 mm length was used for the preliminary experimental campaign. It was instrumented with two radiation gauges and two thermocouples. Radiative heat flux and total heat flux measurements were made in parallel with emission spectroscopy.

Two new Titan atmospheric entry test conditions were developed, with freestream velocities of 6.5 km/s and 8.5 km/s. The first condition simulates peak radiation for Titan entry at the stagnation point, using a test flow with a freestream velocity of 6.5km/s. The second condition, having an 8.5km/s freestream velocity, represents the case where almost all the heat transfer is believed to be from CN dissociation [34].

The conditions were tested in X2, and the freestream cone head pressure was measured. This was done by using a rake with vertically aligned 15^{o} cone head caps to measure the static pressure on the cone surface during a shot. The test times for the two conditions were measured as 150 μs and 200 μs for the 6.5km/s and 8.5km/s respectively. Table 1 presents flow properties for the two conditions where U_1, U_2, p_{s_5} are the primary shock speed, post-shock gas speed, static pressure of the test gas; H_0, U_5, U_e are the enthalpy, expanded test flow speed and the equivalent flight speed.

Emission Measurements

Emission spectroscopy measurements were taken during the 6.5 km/s Titan conditions. The optical arrangement as it was setup in X2 is illustrated in Figure 11. A 1MHz high speed camera Shimadzu HPV-1 was used

Table 1: Flow properties for Titan entry conditions with test gas 5% CH_4, 95% N_2.

	6.5km/s		8.5km/s	
Flow property	Measured	CEA	Measured	CEA
U_1 [km/s]	3.376	-	4.1	-
U_2 [km/s]	-	2.965	-	3.668
p_{s_5} [kPa]	-	31.224	-	2.346
p_{s_∞} [kPa]	-	2.136	-	580.314
p_{c_∞} [kPa]	26.642	27.496	6.675	6.809
T_∞ [K]	-	864.21	-	1583.14
a_∞ [m/s]	-	607.5	-	822
ρ_∞ [g/m^3]	-	7.763	-	1.151
M_∞	-	11.09	-	8
γ_∞	-	1.341	-	1.290
R_∞ [J/kgK]	-	318.398	-	318.434
h_∞ [MJ/kg]	-	1.7101	-	2.444
S_∞ [MJ/kgK]	-	9.697	-	10.913
H_0 [MJ/kg]	-	23.358	-	39.596
U_5 [km/s]	6.58	-	8.62	-
U_e [km/s]	-	6.835	-	8.899

to record 100 frames over the test time. The optical arrangement was designed to image the emitted radiation from the shock layer onto the slit of a UV/Visible system compromised of a SpectraPro 2356i 300mm spectrograph and a detector camera PIMAX 1024 SB ICCD.

Raw spectra as recorded in the experiments is shown in Figure 19a. The orientation of the spectra corresponds to a flow coming from the bottom of the image. Prominent features of the spectra include the two CN violet bands, clearly visible with peaks at 358nm and 385nm. The maximum heating along the stagnation streamline, corresponds to pixels 130-150. Integrated raw spectral lines from this region are shown in Figure 19b. The data is yet to be calibrated for spectral irradiance. The additional (Fe) features in the shock layer reveal the boundary layer before the model face. The two peaks at 394-396nm correspond to the aluminium diaphragm used in the test.

4.4 Ablation study

The geometry of the Hayabusa models tested in the X2 expansion tunnel facility is illustrated in Figure 20. The forebody of the model is a 45 degree sphere-cone which accurately represents the actual capsule at a $1/10^{th}$ scale. The aftbody deviates slightly from the published Hayabusa geometry but these differences will not affect the simulated forebody radiation – the primary concern here.

Two types of model have been tested in the X2 expansion tunnel: a non-coated steel model and a steel model coated with a layer of epoxy. The coated models were created by applying a layer of epoxy to a steel model. After the epoxy was cured, the epoxy layer was machined back to the required dimensions. The extreme heat load experienced by the model at the simulated super-orbital re-entry conditions raises the surface temperature of the epoxy sufficiently for ablation of some of the material which can be detected optically.

A composite negative image of the emissions from the shock layer of the non-coated and coated models as recorded with the high speed camera is presented in Figure 21. The images of both the non-coated and coated models are from the steady flow period.

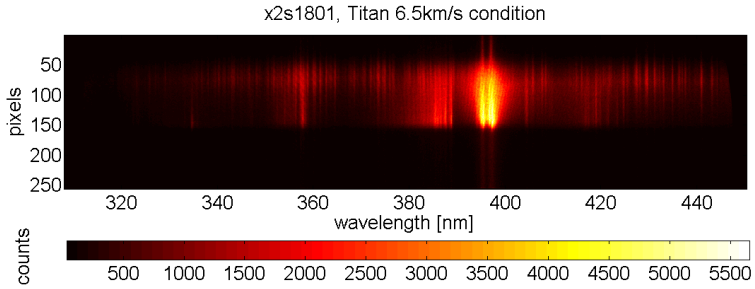

(a) Raw data

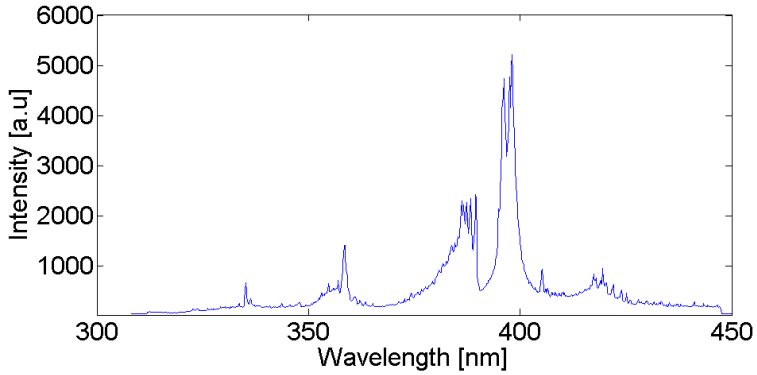

(b) Integrated data

Figure 19: Spectral data from shot number x2s1801, Titan 6.5km/s condition. The sampled region is the maximum heating region along the stagnation streamline. [25]

In the raw images from the high speed camera, the shock layer appears to have a relatively uniform brightness. Consider the optical path length through the shock layer along the lines of sight which pass through the stagnation streamline. The path length close to the leading edge of the shock wave is short relative to the path length through the shock layer region close to the solid surface. Hence, the observed overall uniformity of the shock layer brightness implies emissions are strong close to the shock and fall away towards the body surface. In the case of the models with the epoxy coating, the camera signal rises steeply close to the surface implying the presence there of a layer of high power density. The axisymmetric nature of the flow field allows a quantitative analysis of the emissive power density of the gases in the shock layer via the inverse Abel transform. Images from the high speed camera have been converted to a power density expressed in arbitrary units, via this transform. The results are shown in Figs.22 for non-coated and coated models. As yet, the camera calibration has not been performed to connect absolute emissive power to image intensity. Hence the emissive power is in arbitrary units.

It can be seen from these figures that, for the uncoated model case, there is high power density immediately behind the shock that falls away quickly as the body is approached. For the coated model case, there is a second power density peak of comparable strength close to the model surface. This is thought to be caused by emission from ablation products some of which have reacted with the oncoming air flow in the shock layer. The spectral signatures of CN and C_2 are observed in the spectra reported here. As the flow passes around the body nose and along the skirt, the levels of both the post shock and ablation layer power density peaks decline, however, the decline in peak levels is more severe for the uncoated model case.

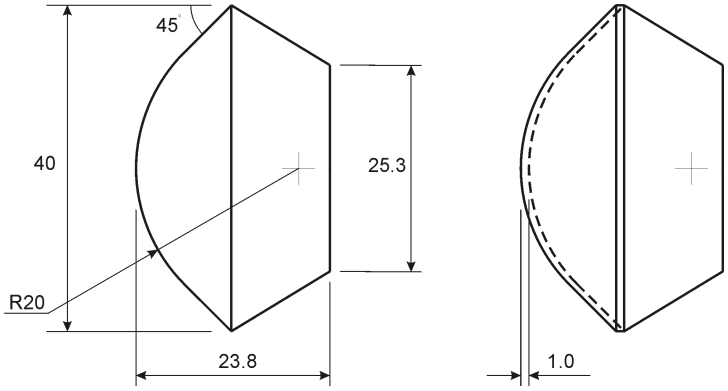

Figure 20: Schematic of the Hayabusa models tested in the X2 facility. Left: non-coated steel model. Right: Model with a 1 mm epoxy layer. [3]

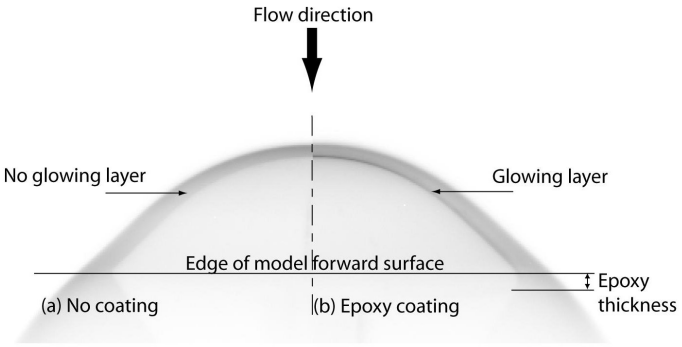

Figure 21: Negative greyscale image from the high-speed camera. Left: no coating. Right: epoxy coating. [3]

Results from four shots using the UV spectrometer are presented in Figure 23. For the production of this figure, the data has been averaged over 6 pixel rows (corresponding to averaging over a spatial distance of 0.1 mm) centred on the peak CN $\Delta\nu = 0$ signal in the shock layer. This corresponds to a location 0.15 ± 0.05 mm upstream of the stagnation point. We identify this region of the shock layer as the ablation layer because it is the region where carbon pyrolysis gas from the epoxy layer encounters nitrogen in the shock layer and reacts chemically. Figure 23 indicates that the epoxy coating results in increased CN emissions at this particular location by a factor of between 1.6 and 1.8. C_2 Swan bands are present only when an epoxy coating is present: no C_2 Swan bands are detected when an epoxy coating is not present.

4.5 Hot wall reentry testing

The impulse facility time scales are insufficient to allow a thermal equilibrium to be reached using the aerothermal heating generated in the facility if the model is initially at room temperature. Times in the order of 1–10 seconds would be required to correctly simulate the effects of ablation and surface chemistry on the flow field for models initially at room temperature. This time scale is required for the thermal energy to be transferred into the surface and reach an equilibrium temperature and to establish the rates of pyrolysis and mass flow which are an integral feature of ablative TPS. This process precludes the study of a fully coupled ablating flow field in impulse facilities, however preheating of the model can be used to eliminate the initial time requirement allowing the study of the effects of ablation and surface chemistry on the flow field around the model.

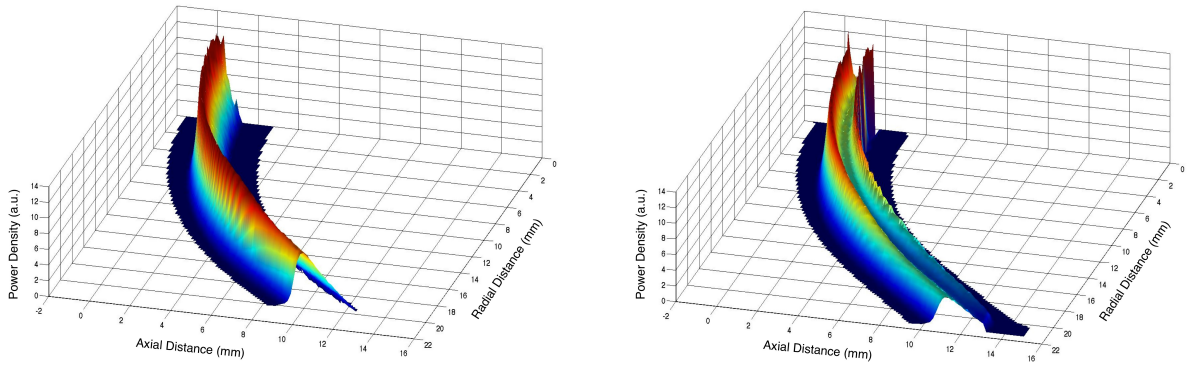

(a) Uncoated model.

(b) With epoxy coating.

Figure 22: Time averaged power densities within the shock layer around the Hayabusa model. [3]

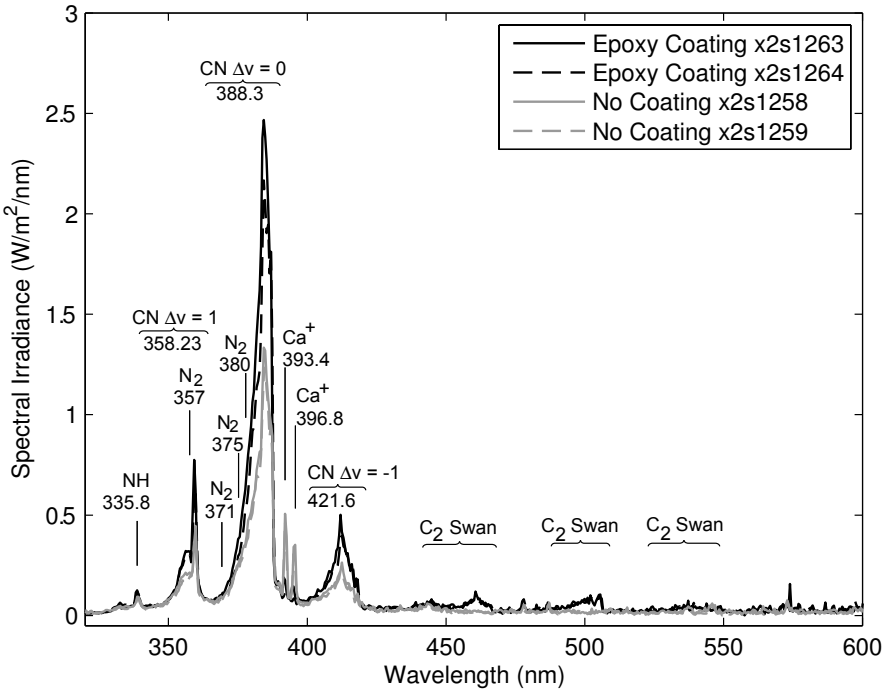

Figure 23: Spectral radiance measured in the ablation layer measured in the stagnation region. [3]

Initial studies have previously been conducted in the University of Queensland expansion tunnels using thin graphite and epoxy layers on models to simulate the ablation, as discussed in Sec. 4.4 [35], however these investigations were limited to wall temperatures of approximately 1200 K and used materials that were different from those used in thermal protection systems.

The concept developed here [27] allows the preheating of carbon fibre based materials, such as commonly used in thermal protection systems, to temperatures of up to 2500 K. This preheating removes the initial time required to reach the equilibrium temperature and allows the flow over a hot ablating body to be investigated in an impulse facility. Although the surface temperature is reached through a different process this creates a situation where the surface boundary condition is matched to that seen in flight and the flow/surface interaction can be simulated.

The intention of this study is to show that it is feasible to investigate the mixing layer due to the ablation and surface chemistry in an impulse facility. A proof of concept study was undertaken in the University of Queensland's X2 expansion tunnel with a simplified model which was preheated to 2000 K and then exposed to a flight equivalent 8.6 km/s air flow representative of that experienced by a vehicle undergoing an Earth re-entry. For this study, CN radiation was used as an indicator of the effect of the preheated wall as this is formed by a surface chemistry reaction which requires a high activation energy for the carbon to leave the surface. This is a reaction that has been highlighted as being potentially important for radiating re-entry flows [36] and one that has not previously been quanitified through laboratory simulation of the hypervelocity aerothermal effects.

The concept of preheating is not new for impulse facilities however previously used methods, such as heaters or radiative heating, have only been capable of heating models up to 800 K and are usually only effective with metallic models. Here, we use a carbon-carbon material for the model which is quite commonly used in flight vehicles and allows preheating up to 2500 K. Resistive heating is used by running a current through the model which causes a large, quick energy delivery into the model causing the temperature to rise to $>$2000 K in less than 10 seconds. This heating can be conducted immediately prior to the expansion tunnel firing, thus when the flow arrives the model is heated to the desired temperature and a high wall temperature impulse tunnel test is possible.

By using a controllable power supply the temperature of the model can be selected for the test. The power required is a function of the losses experienced in the system and the size of the model being heated. At high temperatures ($>$2000 K) the radiative losses of models become quite large (scaling with temperature to the power of 4) and large amounts of power are required. The testing conducted here used a model 10 mm high and 75 mm long and this required 2 kW of power to heat above 2000 K. This represents approximately 1 MW/m^2 surface radiation which limits the temperature which can be achieved with the current apparatus. This methodology allows a new range of preheated model tests to be conducted in impulse facilities and scaling to higher temperatures and/or larger models can be achieved using a larger power supply.

The materials being used for this testing are manufactured using Toray T700S-12k carbon fibre tow and Cellobond J2027L Phenolic resin. The reinforced carbon-carbon (RCC) samples came from the same materials however they were processed further into RCC. The final density of the RCC was estimated to be 1300 kg/m^3.

During the tests, imagery was taken with a VnIR spectrometer, a UV spectrometer, a high speed video camera, a digital SLR taking multiple images for the two colour pyrometry analysis, a data acquisition system recording the power into the carbon-carbon model and a data acquisition system recording the tunnel pressures for flow condition determination.

For these tests in the X2 facility, a Canon 400D DSLR was used. The camera used a Canon EF 75–300 mm lens and was located targeting the front surface of the model as shown in Figure 24b. Typical settings used for the testing were: ISO 100, 1/4000 exposure, f/10 aperture and a focal length of 300 mm.

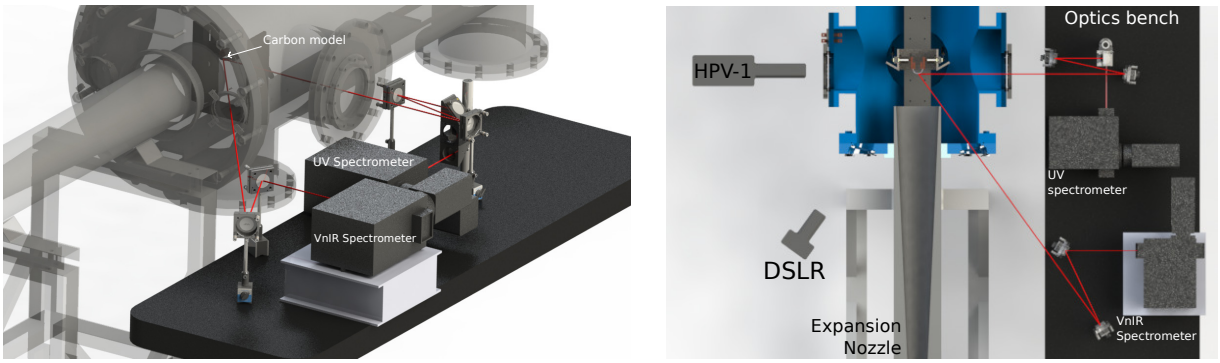

(a) CAD model of optics

(b) Platform view of optics

Figure 24: Representations of the optical layout used during the tunnel testing. [27]

The tests were recorded using a Shimadzu HPV-1 high speed camera to record the luminosity of the flow over the model. The HPV-1 was located perpendicular to the flow at a distance of 1 m as shown in Figure 24b. Various frame rates are possible with the camera however for the majority of the tests videos were recorded at 1 MHz with a 0.5 μs exposure time.

In the tunnel testing, the system was configured with one focusing mirror and one flat turning mirror as indicated in Figure 24, the VnIR optical path is imaging the model surface at an angle of approximately 45^o to the tunnel axis. A 2:1 magnification was used which ensured the spectrometer slit was completely exposed to the surface of the model. The spectrometer was triggered manually prior to the switch-on of the carbon model power supply and recorded 200 frames with an exposure time of 30 ms. This was sufficient to allow the entire heating cycle to be captured and the temperature deduced up to the arrival of the test flow.

For the purposes of this proof of concept testing, CN emission was used as the indicator for the effect of the hot wall on the flow field chemistry. The CN chemical mechanism has been identified as important for re-entry vehicles and a full investigation into the phenomena will be one of the initial uses of this new testing methodology.

The tunnel initial conditions are reservoir: 6.85 MPa air, driver: 742 mbar He with 186 mbar Ar, shock tube: 3 kPa Air and acceleration tube: 10 Pa Air. Shock speeds in the acceleration tube are deduced by measuring the pressure rise along the length of the tube indicating the arrival of the shock at particular locations. The measured shock speeds in the acceleration tube were 8.4$\pm$0.15 km/s which after expansion through the nozzle results in the 8.6 km/s flight speed equivalent conditions.

Figure 25 shows a representation of the model as located in the tunnel during the testing. The model is positioned as a blunt body in the centre of the core flow.

Figure 26 shows the capture area that is imaged during the tunnel tests by the UV spectrometer. This is focused on the stagnation point of the model and captures the model, the shock layer and some of the free stream. The capture area depicted in Figure 26 shows the horizontal dimension to scale however the vertical dimension has been magnified for clarification, the real height of the imaged area during the tests was 25 μm.

Results

Figure 27 shows a montage of images extracted from the high speed camera footage of a hot carbon-carbon test over a 10 μs section of the test time. This shows the shock layer clearly formed over the model and close inspection also shows small particles of hot ablating carbon being removed from the surface of the model as demonstrated. The particle velocity was estimated assuming it was travelling close to the model surface resulting in a velocity in the boundary layer of 1.1 km/s.

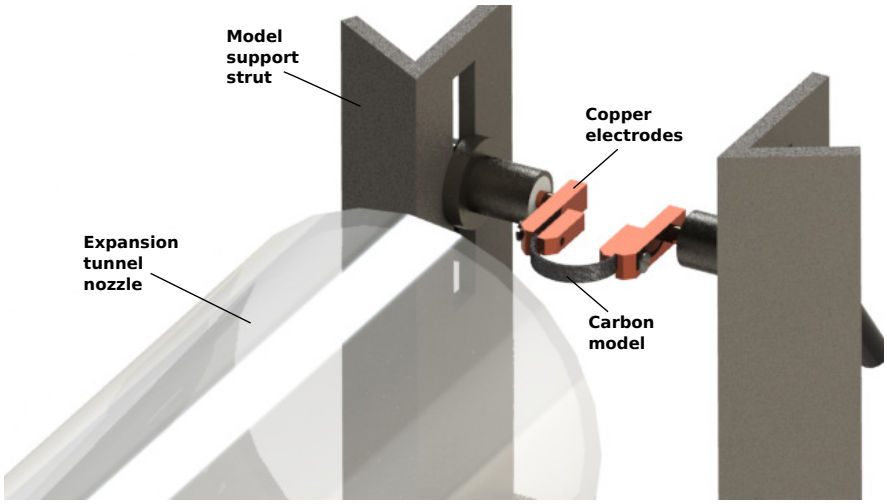

Figure 25: View of carbon-carbon model in X2. [27]

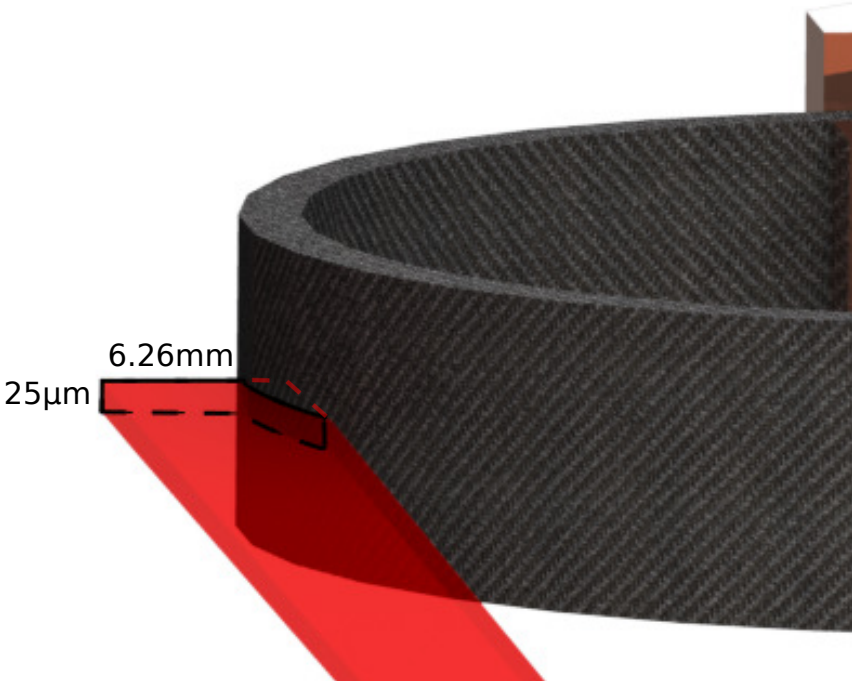

Figure 26: UV spectrometer capture area on model - side on view of model (slit height not to scale). [27]

Figures 28 to 31 show the TCRP and VnIR spectrometer results for a hot wall test conducted in X2. Figures 28 and 29 show the raw image captured with the DSLR camera and the processed temperature extracted from the image at a time of approximately 15 s after the start of the model heating. Images are taken every 2 s during the heating of the model and the final image is taken immediately prior to the test. At this stage the model temperature is reasonably steady and it is this final image that is used to deduce the temperature of the model during the test time. The physical tunnel configuration causes some visibility limitations meaning that only half of the model can be imaged and this is what is shown here. The right side of the image corresponds approximately to the middle of the model where the view is inhibited by the nozzle of the tunnel. The spatial variation in the temperature is due to the fibre locations and the contact

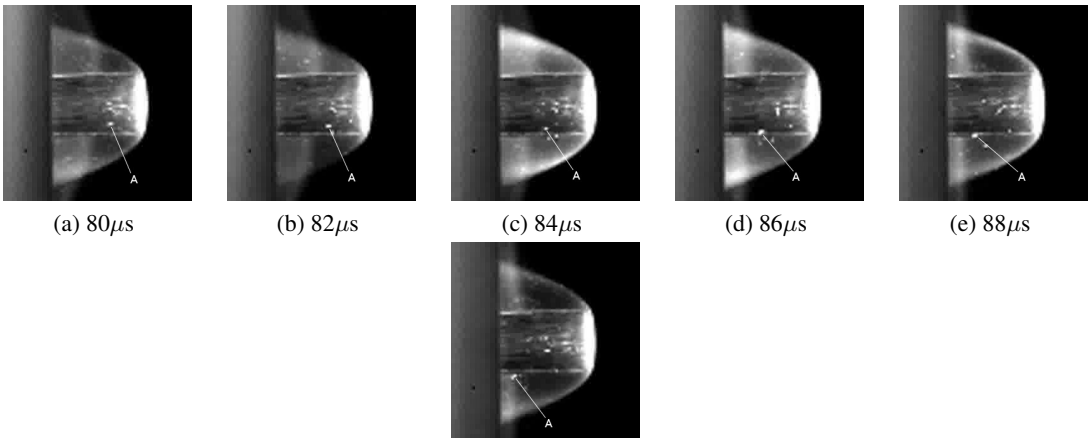

(a) 80μs (b) 82μs (c) 84μs (d) 86μs (e) 88μs

(f) 90μs

Figure 27: Images extracted from the high speed camera footage; 1 MHz framerate, 0.5 μs exposure, shot x2s1758. “A” demonstrates the particle tracking. [27]

resistance between the electrical connections and the fibre rovings. Some fibres are in better physical contact with the electrical connections and hence have a lower electrical contact resistance and more of the current flows through those fibres and heats them more effectively, this does however equilibrate over time as the thermal conductivity causes the energy to spread over the model. In addition the processing technique also introduces some minor discrepancies, pixels where one of the colour channels is either saturated or where the signal to noise ratio is significant are shown as either a ‘hot’ or ‘cold’ spot at either extreme of the displayed scale.

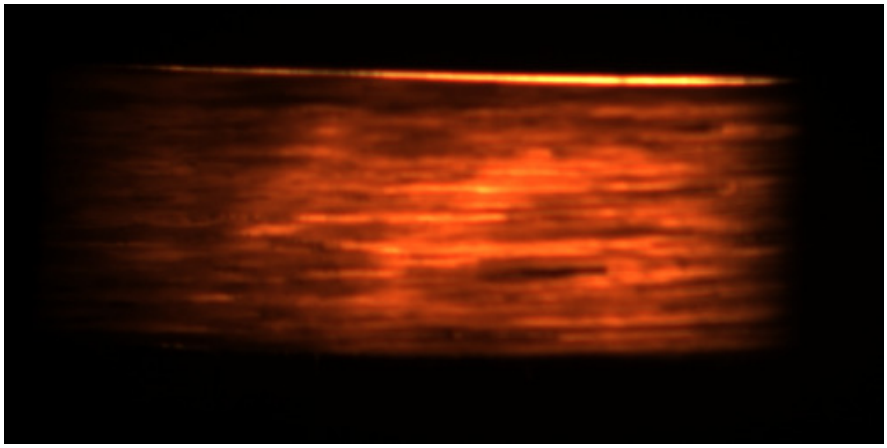

Figure 28: DSLR image of model in tunnel immediately prior to the test time; exposure 1/4000, f/10, shot x2s1775. [27]

The VnIR spectrometer results also show some spatial temperature variation, however it is not seen as clearly because the spectrometer only images a 1D line on the surface of the model. Figure 30 shows the raw, unprocessed VnIR spectral data at a point at the centre of the front surface of the model. Such data was then processed by fitting Planck curves to give time-resolved temperatures at each vertical slit location as shown in Figure 31.

The profile shown in both Figures 29 and 31 are extracted from equivalent positions on the model although from opposing sides of the symmetry plane (see Figure 24b for geometric description). These profiles show the temperature measured with both methods to be of the order of 2000–2200 K with some minor spa-

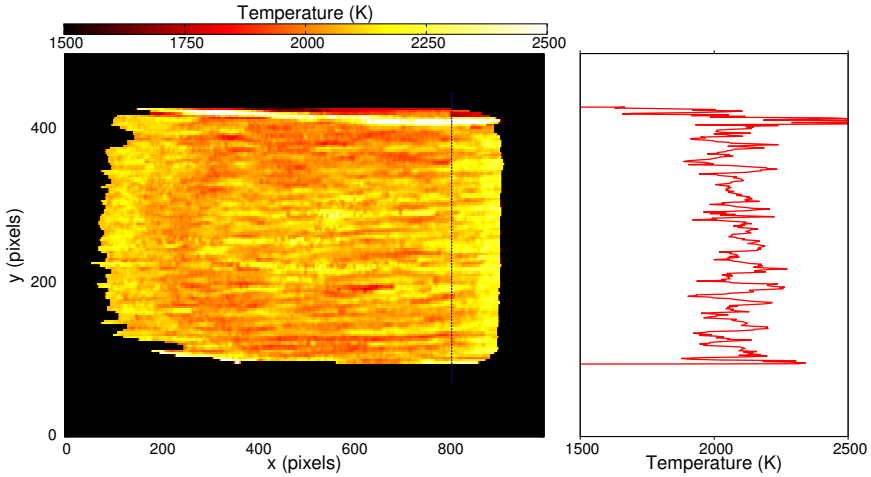

Figure 29: Temperature derived from the DSLR photo of Figure 28 - profile extracted along dotted line at pixel column 800, shot x2s1775. [27]

tial variations as described previously.

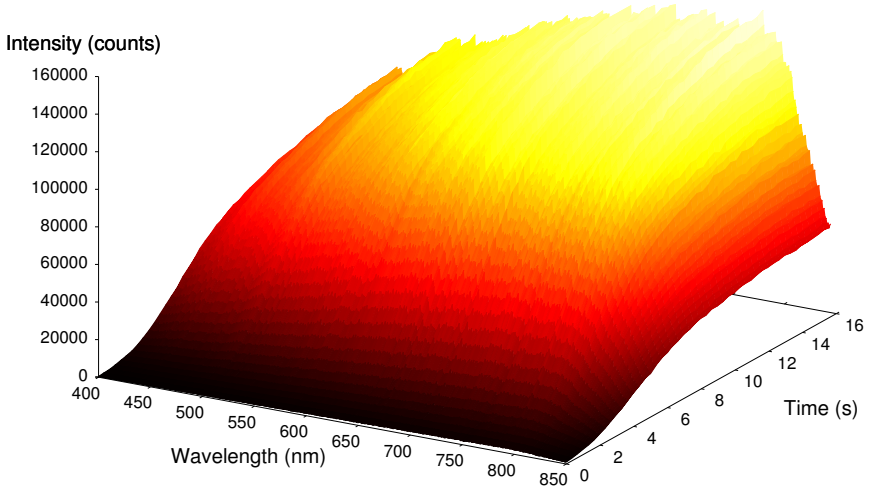

Figure 30: VnIR spectra obtained in the pre-heating period for shot x2s1775. [27]

The temperature-time history of the heating process is shown in Figure 32 with the results of a thermal analysis, the TCRP and the VnIR spectrometry shown. Additionally, the power input and the calculated model resistance are also shown to demonstrate how the material properties change with temperature. The thermal analysis is a one-dimensional transient finite difference model for the carbon and copper supports which includes radiation, conduction and convection effects. The copper supports for the carbon model heat significantly during the test but do not reaching melting temperature for tests of less than 20 s. The oscillations in the power supplied are due to the rectifier that is continually compensating the input voltage in an attempt to output the desired power. The resistance of the model drops as the temperature rises, this is assumed to be a function of the material properties which change with temperature. The most important result is the final temperature of 2100 K, deduced using three different methods which all agree to within $\pm$100 K which is within the expected uncertainty for these methods. Further calibration of the temperature determination methods is being undertaken with the full test optics to increase the certainty in measurements.

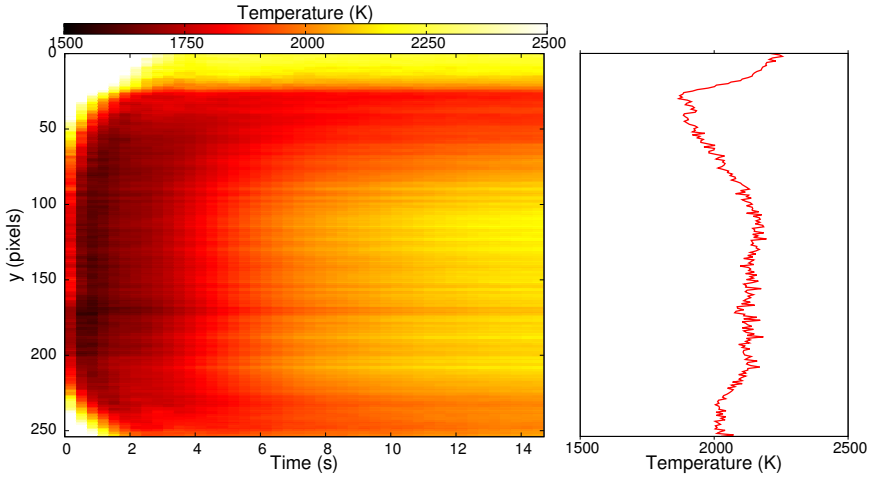

Figure 31: Time resolved temperature plot from VnIR spectrometry of Figure 30 - profile extraced at t = 14.5 s, shot x2s1775. [27]

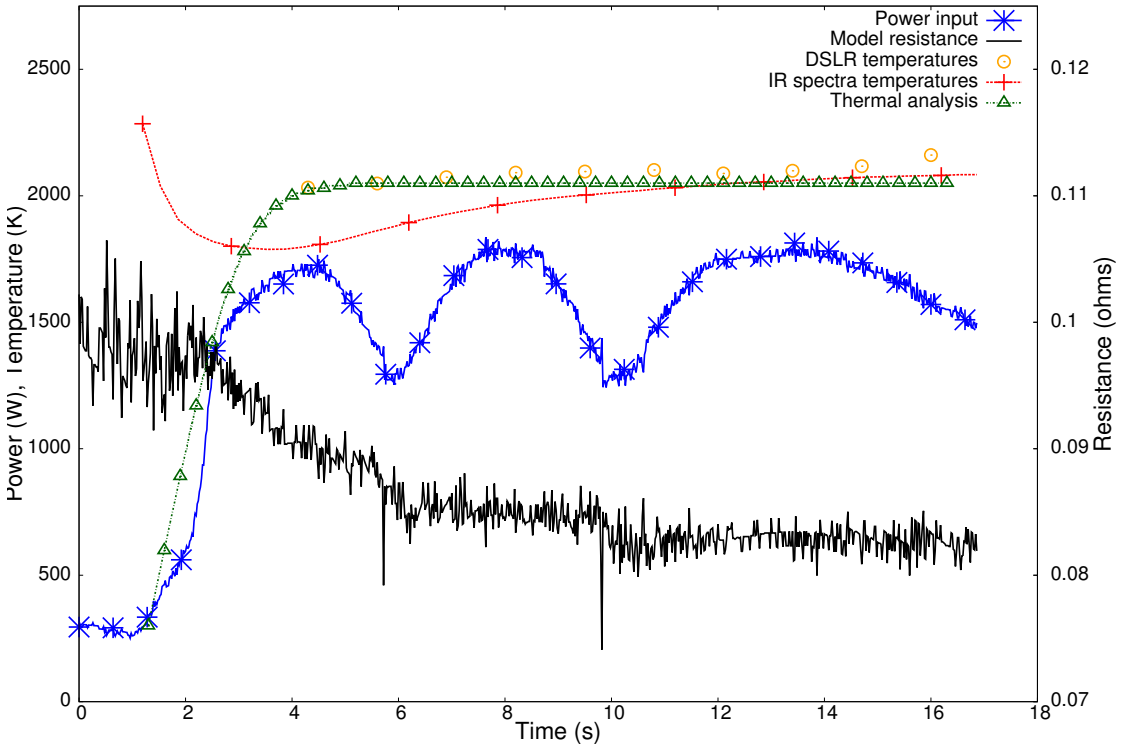

Figure 32: Temperature time history, shot x2s1775. [27]

5 SIMULATION CODES

Because the experimental facilities are complex multiscale machines, we have a range of codes, each with quite different capability and computational requirements. The codes that are used most frequently are:

- `L1d`: a simulation code for time-dependent quasi-one-dimensional flows, used to simulate entire facilities with moderate level of detail, and
- `Eilmer` [37, 38]: a time-accurate simulation code for multidimensional flows, used when multidimensional effects cannot be separated from the transient flow.

A detailed discussion of these codes, in the context of expansion tube analysis, is available in a previous VKI lecture [39].

5.1 One-dimensional Flow Code, L1d

In order to estimate the performance of a free-piston driven impulse facility, one must consider both the dynamics of the piston and gases, and the viscous effects (including heat transfer) simultaneously. Models which omit these effects require a number of facility-specific fudge factors which can be obtained accurately only after the construction and operation of the facility. The computer code `L1d` was originally developed to simulate the (gas-dynamic) operation of a free-piston driven facility during the design process. It is closely related to other light-gas gun codes (see e.g. [40], [41], [42], [43], [44]) and borrows a number of ideas from some of them. The principal features of the code are:

- Quasi-one-dimensional formulation for the gas-dynamics. There is only one spatial coordinate but gradual variation of duct area is allowed.
- The ability to simulate several independent (or interacting) slugs of gas. Also, several pistons/projectiles and multiple diaphragms may be included. Coupling to the gas dynamics is via the boundary conditions of the gas slugs.
- A Lagrangian discretization of the gas slugs. This is done by dividing each gas slug into a set of control-masses (or gas particles) and following the positions of these particles.
- Nominal second-order accuracy in both space and time combined with a robust shock-capturing scheme. The use of a shock capturing scheme means that the same set of equations is used to compute the motion of the gas whether a shock is present or not. This simplifies the code (as shocks do not need to be explicitly identified or tracked) and is especially important in situations where shocks may form from the merging of finite compression waves and where multiple shocks and contact surfaces interact in a complicated manner. It also results in a smearing of the shocks over a couple of computational cells. However, in practice, this is not a problem as any smeared shocks can be sharpened by increasing the grid resolution.
- Viscous effects are included using the standard engineering correlations for friction and heat transfer in pipe flow. Although these correlations are generally derived for steady incompressible flow, they seem to perform adequately in the simulations where the flows are predominantly unsteady and are very compressible.

The general procedure for modelling a specific facility (or system) is to divide the facility into its component parts such as the tube, pistons, diaphragms and volumes of gas (i.e. gas slugs). The description of each component is formulated separately and components allowed to interact through boundary conditions. The core of `L1d` is a time-stepping loop which first applies the specified boundary conditions and then advances

the state of the entire system forward in time by a small increment (or time step). The generic components described in the following sections include a slug of compressible gas, a piston and a diaphragm.

Each slug of gas is treated in a Lagrangian framework in which the slug is divided into a number of control-mass elements (or cells) moving in a variable-area duct. Flow in one dimension only is considered and any area changes in the tube area are assumed to be gradual. Although the boundary layer along the tube wall is not completely modelled in the formulation of the gas-dynamic equations, some of its effects are modelled in the momentum equation by the addition of a wall shear stress. These approximations are arguably the most troublesome part of the modelling process as they cannot be fixed later by simply increasing the grid resolution.

Each piston is assumed to have fixed mass, length and frontal area. The piston state is given by a flag indicating whether the piston is constrained. Its centroid position and its velocity are updated in step with the dynamics of the adjacent gas slugs. For the simulation of the X2 facility, the frictional force is assumed to be due to the "chevron" seal near the front face of the piston. Diaphragms are also implemented as a flag for the status of the diaphragm (intact or burst) and a burst pressure. Note that the burst pressure is a "dynamic" burst pressure which may be significantly higher than the burst pressure obtained in hydrostatic rupture tests [45]. The state quantities for both pistons and gas slugs are advanced in time with a simple, low-order integration scheme.

5.2 Multidimensional-Flow Code, Eilmer

For simulating two- and three-dimensional flow fields, we use the code `Eilmer` [38], which is one of a series of derivative codes from the single-block Navier–Stokes integrator `CNS4U` [46].[1] The code solves the compressible Navier–Stokes equations via a cell-centred time-dependent finite-volume formulation. The governing equations are expressed in integral form over arbitrary quadrilateral cells, with the time rate of change of conserved quantities in each cell specified as a summation of the mass, momentum and energy flux through the cell interfaces. For two-dimensional flow, the code is capable of considering both planar and axisymmetric two-dimensional geometries and the thermochemistry module can handle gases in chemical equilibrium or nonequilibrium. When simulating gases with finite-rate chemistry and radiation energy exchange, these physical processes are treated with an operator-split approach. The computational core of `Eilmer` is written in C++, with the option for user-defined functions such as boundary conditions provided as Lua scripts. Preprocessing (*i.e.* grid generation) and postprocessing is handled by a collection of Python programs.

The code is formulated around the integral form of the Navier-Stokes equations. The array of conserved quantities is dependent on the thermal model under consideration, and for the thermal nonequilibrium models includes an array of modal energies. We choose to solve both total and all individual species continuity equations to add rigour to our solver. The redundant information gives us a good idea when the numerics are running into trouble.

The flux vectors are divided into inviscid and viscous contributions and the corresponding vector of source terms is separated into geometric, chemistry, thermal energy exchange and radiation contributions in order to apply the operator-splitting integration approach, as advocated by Oran and Boris [47] (see Chapter 11 of their text), is applied whereby the physical mechanisms are treated in a decoupled fashion. Currently the radiative source term vector is applied closely coupled with the inviscid fluxes. This seems to be adequate for the work done thus far, but may need to be revised for strongly radiatively coupled flows.

The advantage of the operator-splitting approach is that the optimal integration scheme for each component of the physics can be implemented. This is especially useful for solving large chemical kinetic systems.

[1] At the time of running the axisymmetric simulations discussed in the following sections, the code went by the name `mb_cns2`.

The resultant set of ODE systems are integrated in time via a simple multi-stage update scheme for the inviscid and viscous increments, one of a selection of methods (including a method for stiff systems) for the chemistry increment and the 4^{th} order Runge-Kutta-Fehlberg method for the thermal energy-exchange increment.

6 FACILITY SIMULATIONS

The `L1d` simulation gives quick results for bulk gas conditions in the shock tube but does not include the details of the reflected-shock interaction with the shock-tube boundary-layer. To capture these details, and the expansion process through a high Mach number nozzle, axisymmetric flow simulations are used. Even though the Drummond tunnels is a relatively low enthalpy machine, the axisymmetric simulations of the full facility are computationally demanding.

For the modelling of the X2 expansion tube, we again start with the `L1d` modelling of the whole facility to look at developing operating conditions with a new, light weight piston (Section 6.1). Since this mode of analysis in exploratory, we need to do many simulations and concentrate on the large-scale facility behaviours of piston motion and shock speed. Once the operational conditions are defined, we need to increase the level of detail of the simulation model in order to get complete estimates of the test-section flow conditions. The interaction of the final expansion and chemistry, together with substantial boundary layers growing in the acceleration tube, demands a high resolution numerical simulation. The computational cost for doing this high-resolution axisymmetric simulation for the entire X2 machine is very high so we make use of both simulation codes. The `L1d` code is used to model the whole facility and transient flow data, just upstream of the secondary diaphragm, is fed to axisymmetric simulation of the unsteady expansion process through the acceleration tube and into the dump tank. An example of this hybrid simulation approach is discussed in Section 6.2. These are the same simulation studies presented in the previous VKI lecture [39].

6.1 Commissioning a New Lightweight Piston for X2

The Free Piston Driver

The free piston driver is currently our preferred technique to achieve high performance drivers for our impulse facilities. Since this type of driver compressively heats the driver gas, it is capable of achieving both the high pressures and the high sound speeds required to generate strong shock waves. However, the free piston driver presents three main challenges:

1. Tuning its operation to prevent damage to the piston, to the buffer and to the compression tube.
2. Tuning its operation to achieve sufficient constancy of driver pressure for a sufficient duration.
3. The monetary cost of the driver assembly is very high since the structural requirements are very high.

Stalker [48, 49], who invented the free piston driver for shock tubes, describes the basic operation of the free piston driver. A piston initially separates a volume of high pressure reservoir gas (typically air) from a volume of lower pressure driver gas (typically Helium, for both its high sound speed and safe handling characteristics). The piston is released and is accelerated by the high pressure reservoir gas into the driver gas. The acceleration continues until the pressures on both sides of the piston are equal. At this point, the piston has acquired significant kinetic energy from the reservoir gas and therefore continues to compress the driver gas as it decelerates, transferring its kinetic energy to the driver gas. The pressure in the driver gas

continues to increase until the diaphragm separating the compression tube and the shock tube ruptures, upon which shock tube flow is initiated [48, 49].

In order to achieve a high temperature in the driver gas, large compression ratios are typically used, therefore the volume of driver gas at diaphragm rupture is relatively small. If the piston is moving with relatively low velocity at this point, the driver gas slug has approximately constant volume. The unsteady expansion will therefore lead to a rapid pressure drop in the driver gas. The effect of this pressure drop is then transmitted downstream as a reflected $u + a$ characteristic, potentially interfering with downstream flow processes before or during the test time [48].

We have recently been trying to produce high Mach number, high static pressure flow conditions in the X2 expansion tube facility, however, initial attempts did not achieve expected results. The existing 35 kg piston is relatively heavy for the length of compression tube and therefore is operated at slow speeds; the result being that the driver gas maintains its pressure for a relatively short duration. For the high speed flow conditions for which X2 is typically used (such as planetary entry between 6 and 10 km/s), critical flow processes occur in the test section before the reflected $u + a$ characteristic from the driver reaches the test section, and target flow conditions are therefore achieved.

However, considering the slower shocks generated through the dense test gas for high total pressure conditions, arly pressure loss in the driver manifests itself in shock speeds which rapidly slow down before the critical flow processes reach the test section, preventing target flow conditions from being achieved. Table 2 summarises a Mach 13 high total pressure flow condition which was attempted with X2. Figure 33 shows several shock speeds measured at different points along the tunnel and compares these to theoretical estimates based on classical analytical calculations (i.e. the original target shock speeds).

Symbol	Value	Units	Description
$p_{A,0}$	1.1	MPa	Reservoir fill pressure, Air.
$p_{D,0}$	30.0	kPa	Driver fill pressure, 100% Helium.
p_{rupt}	15.5	MPa	Primary diaphragm rupture pressure.
λ	42.5	[-]	Driver compression ratio.
m_p	35.0	kg	Piston mass.
p_{sec}	150	kPa	Secondary driver fill pressure, Helium.
p_{shk}	330	kPa	Shock tube fill pressure, Air.
p_{acc}	254	Pa	Acceleration tube fill pressure, Air.
L_{sec}	3.424	m	Secondary driver tube length.
L_{shk}	1.301	m	Shock tube length.
L_{acc}	4.254	m	Acceleration tube length.
M	13.4	-	Predicted Mach number at nozzle exit; target $= 13.0$.
u	3.950	km/s	Predicted flow velocity at nozzle exit; target $= 3.952$ km/s.
p_0	$1,450$	MPa	Predicted total pressure at nozzle exit.
t_{tt}	0.063	ms	Predicted test time.

Table 2: Mach 13 calculated flow condition.

Referring to Figure 33, shock speeds are seen to significantly attenuate, particularly in the high pressure (330 kPa initial fill pressure) air-filled shock tube. An analysis from `L1d2`, which shows predicted shock speed as the incident shock traverses the length of the tunnel, demonstrates good agreement with experimental results. This shock attenuation results in significantly reduced speed and total pressure in the test gas compared to the target flow condition. To address this problem, a new lightweight piston was developed for use in a tuned driver configuration, described in the next sections.

It is noted that a secondary driver was used for this experiment. The secondary driver is an intermediate tube filled with Helium, located between the primary diaphragm and the air-filled shock tube. It is configured so that the sound speed of the shock processed Helium in the secondary driver exceeds the sound speed of

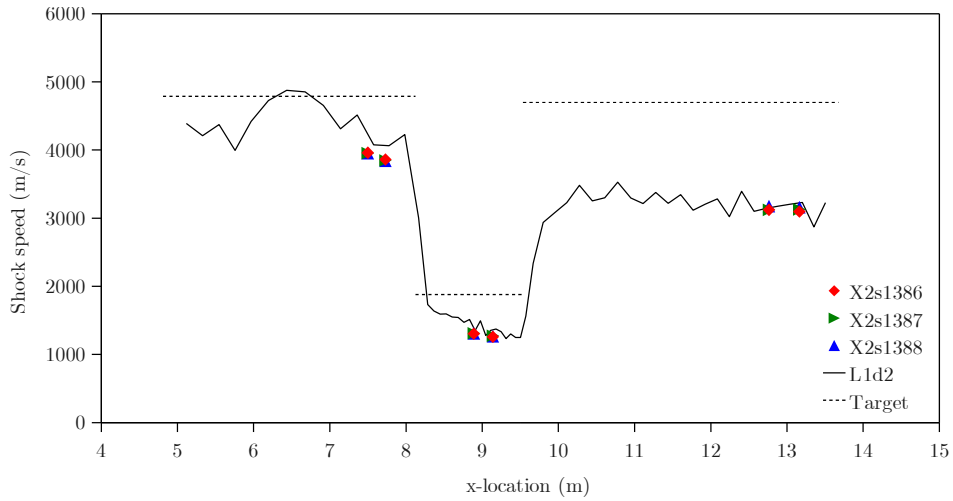

Figure 33: X2 shock speeds for Mach 13 condition, using 35 kg piston with 100% Helium driver. Data points denoted 'X2s...' indicate experimentally measured shock speeds.

the expanded driver gas. This increase in sound speed across the interface between the two gases prevents transmission of transverse acoustic noise in the driver gas into the adjacent gas. If the air filled shock tube is used directly adjacent to the primary diaphragm, this sound speed increase is not achieved, resulting in significant unsteadiness in the test flow. This phenomenon is detailed in Paull and Stalker [50].

Tuned Piston Operation

The concept of tuned piston operation was originally proposed by Stalker in [48] and [49] and attempts to increase the duration over which driver gas is maintained at a useful pressure. It involves configuring the driver so that diaphragm rupture occurs while the piston still has sufficient velocity to compensate for driver gas loss to the shock tube [48]. Ignoring wave processes in the driver, there is a reference piston speed, U_{ref}, which will exactly compensate for driver gas loss into the shock tube, thus resulting in approximately constant pressure in the driver. The actual piston speed at the moment of diaphragm rupture, u_{rupt}, is non-dimensionalised by this reference speed, U_{ref}, to produce Itoh's [51] piston over-drive parameter, β:

$$\beta = \frac{u_{rupt}}{U_{ref}} \tag{1}$$

Stalker [49] proposed the idea of configuring the driver such that $\beta > 1$, thereby "over-driving" the piston. For $\beta > 1$, the piston will actually momentarily continue to increase the driver pressure following diaphragm rupture, before pressure begins to fall again. The duration of time over which this variation in driver pressure is within acceptable limits (typically considered to be around 10% of the target pressure [52, 49, 48, 51]), can correspond to a significantly extended period of useful supply time. This concept is explained schematically in Figure 34.

Piston Soft Landing Condition

Over-driving the piston results in the piston having a relatively large velocity (typically $100 - 300$ m/s) at the moment when the diaphragm ruptures. However, it is also necessary to stop the piston before it collides with the end of the compression tube, which can prove challenging since the distance available to decelerate the piston is relatively small for the high compression ratios required for driver performance. Itoh et al.

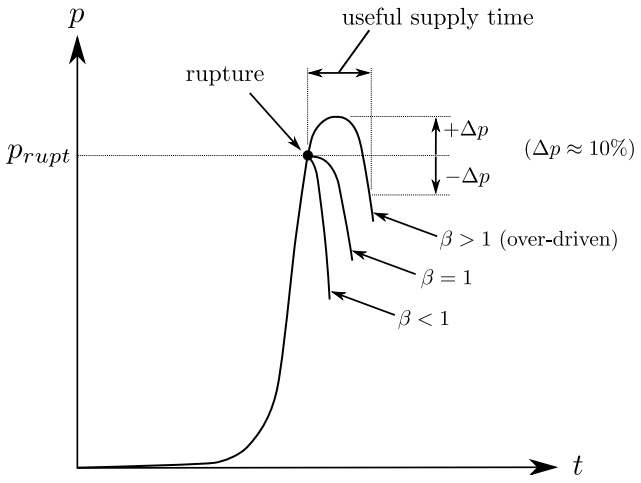

Figure 34: Effect of piston over-driving on driver pressure.

[51] identified the types of motion possible, after diaphragm rupture, as the piston approaches the end of the compression tube. These are shown in Figure 35 and are defined as being either 'piston rebound', 'soft landing', or 'direct impact'. The eventual piston motion depends primarily on the properties and initial fill pressures of the reservoir and driver gases, the piston mass, and the geometry of the compression tube and reservoir. Itoh [51] proposes targeting the soft landing condition and sizing the piston buffer so that it catches the piston at its inflection point (where piston velocity and acceleration are simultaneously zero; i.e. $u_m = 0$ per Figure 35).

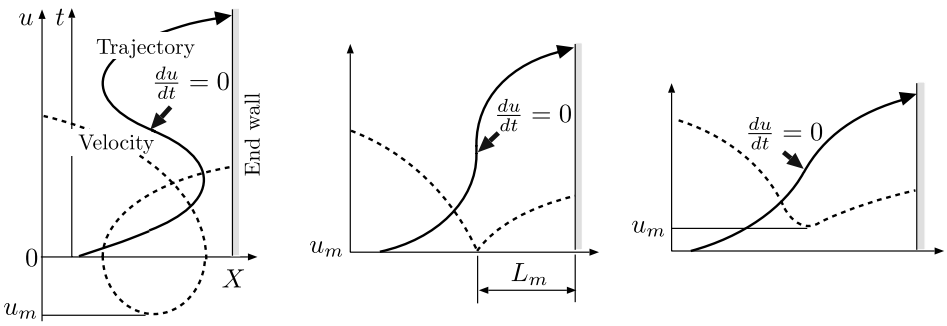

(a) Rebound impact $u_m < 0$ (b) Soft landing $u_m = 0$ (c) Direct impact $u_m > 0$

Figure 35: Characteristics of piston motion (taken from Itoh [51]). Subscript m refers to the instant when piston acceleration is zero; if $u_m = 0$ then the piston has an inflection point where it can theoretically be 'caught' by an appropriately sized buffer, thus avoiding impact.

A soft landing condition was targeted for the new X2 free piston driver. It was considered impractical to incorporate brakes in the piston (which help prevent the rebound motion identified in Figure 35), and survivable direct impact is never feasible for anything other than low speed impacts. An analysis in accordance with Stalker [49] indicated that it was necessary to make the new piston as light as possible. Structural strength and facility interface requirements (i.e. the ability to use the piston with the existing compression tube and with the existing launcher arrangement) placed restrictions on how light the piston could be made. However, the final mass of 10.5 kg was determined to be sufficiently low to achieve a tuned driver condition

which would have sufficient performance to achieve the target flow conditions. The new lightweight 10.5 kg piston is shown in Figure 36.

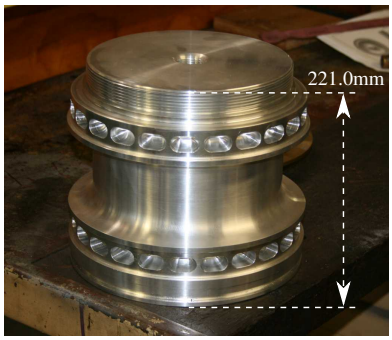

(a) Piston body, machined from 7075-T6 aluminium. Note: material removal across piston skirt, and circumferential pocketing.

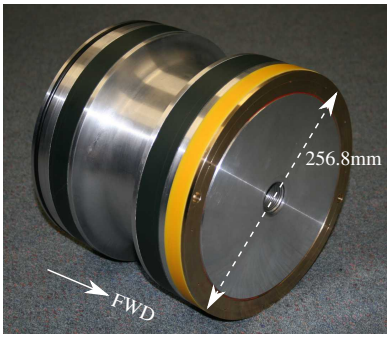

(b) Final piston assembly. Note: nylon chevron seal (yellow) and wear bands (dark green), and copper alloy seal support ring.

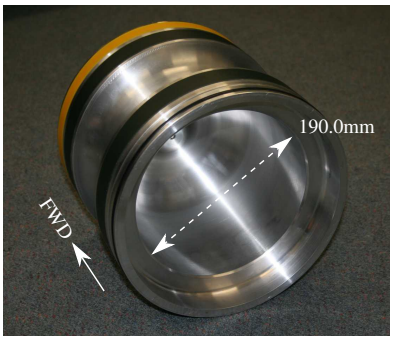

(c) Final piston assembly, viewed from behind. Note: internal cavity which interfaces with piston launcher.

Figure 36: New lightweight piston for X2. [17]

Considered qualitatively, tuned free-piston driver conditions require comparatively light pistons for the following reasons:

1. At the point of diaphragm rupture, the piston velocity needs to be high in order to match the mass flow of driver gas into the shock tube. Especially for a relatively short compression tube like X2's (approximately 4.5m), a piston must be light enough to accelerate to a high speed over this short distance, or else reservoir pressures must become prohibitively high.

2. For large compression ratios, the distance between the piston and the end of the compression tube is quite short. For a given driver gas pressure at rupture, the piston needs to be very light to decelerate to rest over this short distance.

Calculation of New Free-Piston Driver Conditions

There are practically limitless combinations of parameters which will lead to tuned operation of a free piston driver, but several design constraints reduce the design space to a more manageable scale:

1. Piston mass: minimum piston mass is limited by structural and interface requirements (10.5 kg for X2's new lightweight piston).

2. Driver pressure: the compression tube is limited by the magnitude of pressure it can structurally contain (40 MPa for X2).

3. Reservoir pressure: the reservoir fill pressure, which accelerates the piston down the compression tube, is limited by reservoir structural strength (X2 has recently been temporarily rated to 8 MPa to permit operation of these driver conditions, however it has been designed for 10 MPa and will be re-rated accordingly at a future date).

4. Compression tube length and diameter: there is significant expense involved with changing the fundamental configuration of the facility, therefore compression tube geometry was assumed to be fixed.

Several variables remain available for driver condition design:

1. Reservoir fill pressure (0-8 MPa).
2. Driver fill pressure ($<$1 MPa).
3. Driver gas composition (Helium and Argon). The required piston speed for tuned operation depends on the speed of sound of the compressed driver gas. Reducing the sound speed (through the addition of Argon to Helium), reduces the required piston speed, however shock strength is also reduced.
4. Primary diaphragm thickness and material (in this study, diaphragm thickness was limited to 1.2, 2.0 and 2.5 mm thick, cold-rolled steel sheet; each was pre-scored to 0.2mm depth; rupture pressures were assumed to be 15.5, 27.9 and 35.7 MPa respectively, based on previous testing).
5. Buffer length (the distance from the extreme end of the tube where the piston makes contact with the buffer).

The process used to develop new driver conditions is outlined in Figure 37. The first step was to develop a rapidly solved 0-D perfect gas analytical model of the free-piston compression process. The piston equations of motion were obtained from Hornung [53] and used to predict piston motion and driver pressure before and after diaphragm rupture (assumed physical processes are shown in Figure 38). The 0-D model was used to manually identify a range of potential tuned driver solutions. The computational time was sufficiently small that each solution could be quickly identified.

Whilst the 0-D model proved capable of modeling the driver compression process fairly effectively, it could not make accurate predictions of required reservoir gas fill pressure. The reservoir gas expansion process was assumed to be an ideal unsteady expansion as shown in Figure 38b. With X2, reservoir gas must pass through an area change and also through a slotted launcher (refer Figure 39). This convoluted flow path has the effect of throttling the expansion process, significantly reducing the strength of the reservoir pressure force eventually acting on the piston. Further, X2's reservoir has finite length, and the unsteady expansion through the reservoir eventually reflects from the extreme end and causes a further pressure drop. Both of these factors necessitate a much better predictive tool for the reservoir gas flow.

`L1d2` was used to fine tune the free-piston driver configuration prior to any experimental testing. The code is capable of capturing the longitudinal unsteady wave processes which occur during piston operation and includes piston friction, flow chemistry, and pipe-flow viscous effects along the tube walls. Gradual area changes can be handled by the code, however 3-D physical processes, such as flow through the launcher, cannot be directly modeled. To simulate the effect of these complex flow paths, `L1d2` uses loss regions, which apply a loss factor over a finite length of the tube where an area contraction etc. is present. Representative loss factors can only be determined from experimental data, therefore development of loss factors must occur in conjunction with experimental testing. There is no guarantee that a loss region will model a disturbed flow region with useful accuracy; however, anecdotal experience indicates that the modeling tool is quite effective once tuned for a given test condition. The `L1d2` driver geometry used to model X2 with the lightweight piston is shown in Figure 40.

Considering the existing 35 kg free piston driver for X2, the driver has been configured such that the amount of reservoir gas energy imparted to the piston is only a little greater than that required to rupture the steel diaphragm; for example, if the reservoir fill pressure is lowered by 10-20%, the piston will not have enough energy to raise driver pressure to the diaphragm rupture pressure, therefore the diaphragm will not rupture. The result is that the piston does not have significant energy following diaphragm rupture. Further, since the piston is heavy, this energy is not associated with a high velocity, therefore the risk of significant impact velocities into the end of the compression tube are low.

A key characteristic which differentiates tuned free-piston driver operation with the lightweight piston is that the piston is given significantly greater energy than that which is required to break the diaphragm,

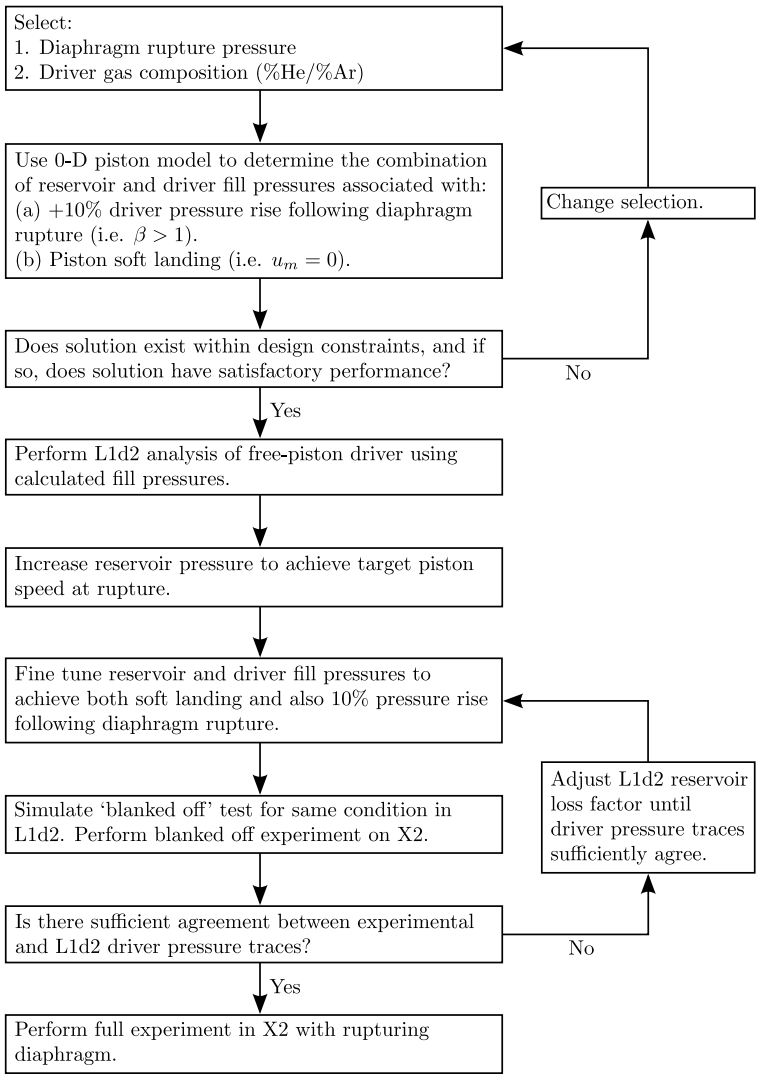

Figure 37: X2 free-piston driver condition development process.

since it must also have sufficient energy to continue to push driver gas through the throat of the driver, at full pressure, *after* the diaphragm has broken. The lightweight tuned piston has to be accelerated to much higher velocities, be decelerated over a very short distance, and has significantly greater energy than that required to rupture the diaphragm. The risk of facility damage due to uncertainties in the analysis are much greater, therefore predictive tools must be as accurate as possible. To achieve this accuracy with `L1d2`, a series of blanked off tests was performed.

Blanked-Off Driver Tests

A blanked-off driver test involves operating a free-piston driver condition using a stiff, non-rupturing diaphragm, typically manufactured from thick steel. For this commissioning process, a PCB pressure transducer was located in the diaphragm, so that driver pressure could be measured during the piston compression process. During a blanked off test the piston bounces back and forth until the piston comes to rest. So long as the driver pressure does not exceed the facility pressure limit, no damage will be done to the piston. A corresponding analysis can be performed with `L1d2`. The `L1d2` model is then tuned until an acceptable

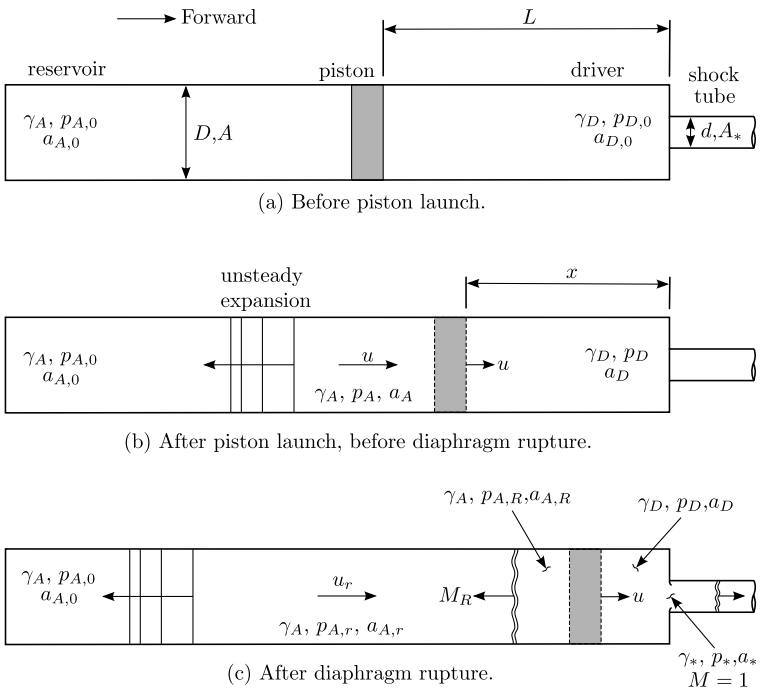

Figure 38: Assumed free piston driver states, pre- and post- diaphragm rupture.

Figure 39: Piston launcher for X2 (shown detached from tunnel). Note: the launcher inserts into piston; reservoir gas must channel through the slots in the launcher, with significant resultant losses to the flow.

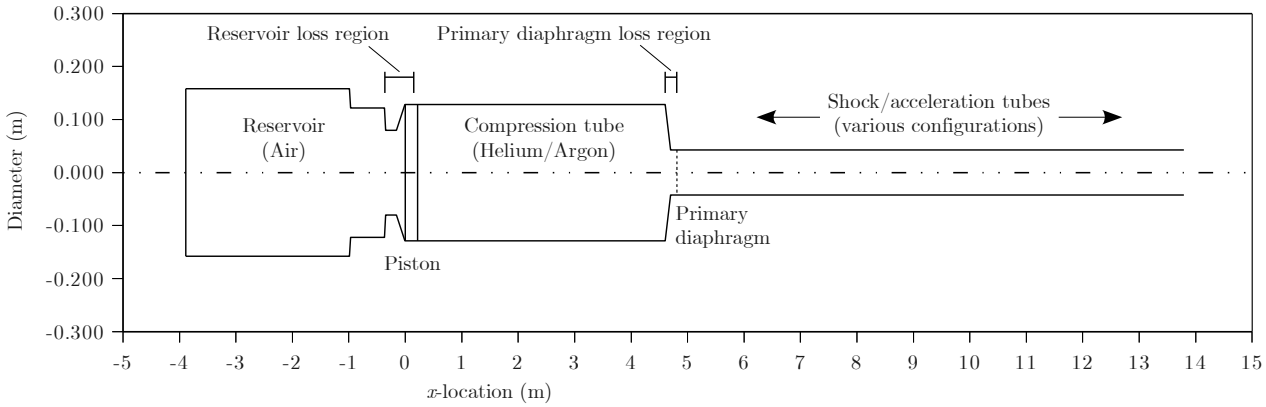

Figure 40: `L1d2` geometric representation of X2 impulse facility. Note: longitudinal scale has been compressed to fit diagram onto page.

level of correlation is obtained between the experimental and numerical pressure traces.

This methodology is very effective, since it allows full correlation of the driver pressure trace right up until the moment when the diaphragm rupture pressure is reached. At this point with a normal experiment, the diaphragm would then rupture, initiating shock tube flow. If strong agreement can be obtained with the blanked off tests, then it increases confidence that the post-diaphragm rupture piston dynamics will also be predicted with good accuracy.

A broad analysis of different driver conditions using the 0-D analytical model, followed by detailed analysis with `L1d2`, eventually led to three driver configurations which were considered to be feasible. The three conditions each used an 80% Helium / 20% Argon driver gas mix. The difference between the conditions was the thickness of the cold-rolled steel diaphragm for each; 1.2 mm, 2.0 mm and 2.5 mm. Table 3 details the three new driver conditions.

			Fill pressures			
Driver condition ID [–]	Piston mass [kg]	Diaphragm thickness[1] [mm]	$p_{A,0}$ [MPa]	$p_{D,He,0}$ [kPa]	$p_{D,Ar,0}$ [kPa]	Buffer Length[2] [mm]
LWP-1.2mm-Rev-0	10.524	1.2	4.94	88.2	22.1	100
LWP-2.0mm-Rev-0	10.524	2.0	6.85	74.3	18.5	45
LWP-2.5mm-Rev-0	10.524	2.5	6.08	61.7	15.5	45

[1] Diaphragms are manufactured from cold-rolled steel and pre-scored to 0.2 mm depth.
[2] Buffer is comprised of 6x50 mm diameter nylon studs.

Table 3: X2 lightweight piston finalised driver conditions.

Blanked-off tests were performed for each condition prior to performing diaphragm rupturing experiments. Figures 41(a-c) compare pressure traces between `L1d` predictions and experimental measurement. Close correlation is observed for the average pressure magnitudes. There is some difference in the unsteady behaviour (waviness); it was found that `L1d` had difficulty predicting the detailed unsteady behaviour of the driver pressure through the sharp area change to the primary diaphragm. The `L1d` pressure traces are taken just before the compression tube area reduces. It was found that loss factors had to be increased from 0.5 (which is used with the existing 35 kg piston `L1d` model) to approximately 3.5 for the lightweight piston, to obtain good agreement between numerical and experimental driver pressure traces. This is not surprising, since the reservoir pressures are almost an order of magnitude higher, and the piston velocity and acceleration are also much higher.

It is also noted that for blanked-off experimental tests with 2.0 and 2.5 mm steel diaphragms, the driver pressure was scaled upwards to ensure peak pressure did not exceed the facility limit of 40 MPa. Since reservoir pressure has proven most difficult to predict accurately, the reservoir pressure was not scaled. Prior to the rapid increase in driver pressure as the piston nears the end of its stroke, piston dynamics is primarily dependent on reservoir pressure (i.e. driver pressures are low for most of the piston stroke). Therefore these scaled blanked-off tests still permit reasonable verification of most of the compression process.

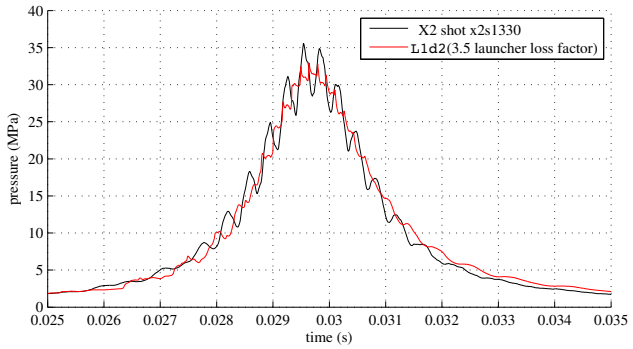

(a) Driver condition LWP-1.2mm-Rev-0 (100% driver fill pressure / 100% reservoir fill pressure)

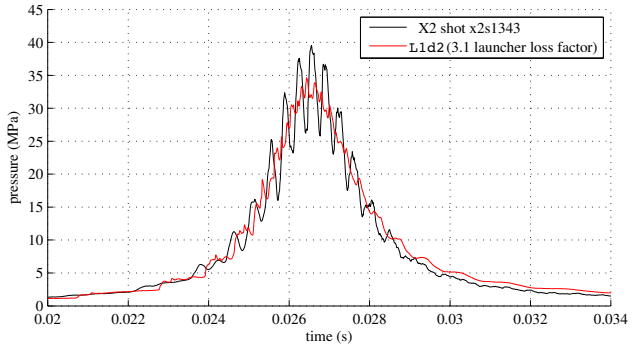

(b) Driver condition LWP-2.0mm-Rev-0 (162% driver fill pressure / 100% reservoir fill pressure)

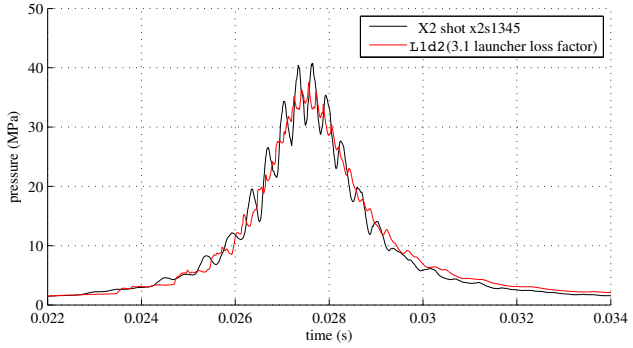

(c) Driver condition LWP-2.5mm-Rev-0 (170% driver fill pressure / 100% reservoir fill pressure)

Figure 41: Comparison of experimental and numerical driver pressures for new tuned lightweight piston driver conditions (refer Table 3). Experimental pressure traces have been time-shifted to match `L1d2` predictions.

Since `L1d` uses a pipe flow model to calculate heat loss, it does not predict heat loss well for a compres-

sion process where the gas is very hot, but only moving with relatively low velocity (i.e. for a heavy, slow piston). For these experiments, the volumetric compression ratio of the driver gas at the end of the piston stroke was measured experimentally using sacrificial soft metal rods fixed into the end of the tube, and it was found that the volumetric compression ratio was well approximated by the `L1d2` simulations. This indicated that heat loss was not significant during the compression process.

Figure 42 shows the `L1d` predicted piston velocity-displacement trajectory for driver condition LWP-2.0mm-Rev-0 from Table 3. It can be seen that the deceleration of the piston prior to reaching the inflection point is significant and that incorrectly locating the buffer too far forward of the tube end may result in very high speed impact. Driver heat loss is very important in this respect, since significant heat loss will result in a smaller driver gas volume at high pressure and, if not properly modeled, may result in the buffer being located too far forward.

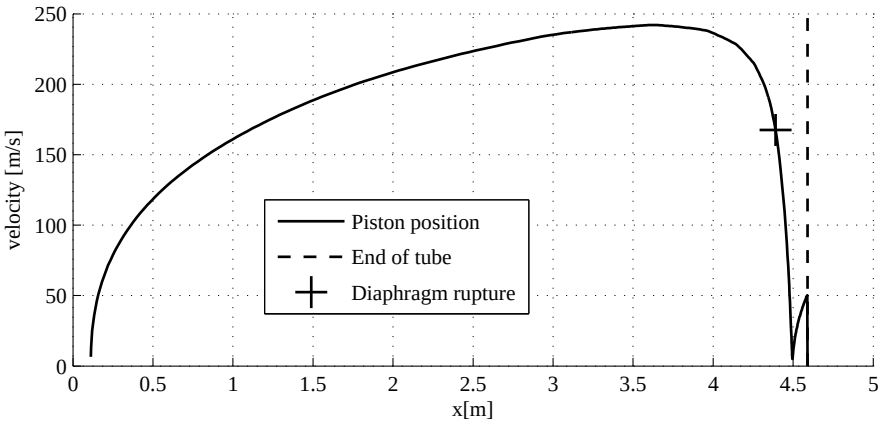

Figure 42: Piston velocity vs. position along compression tube, driver condition LWP-2.0mm-Rev-0. To achieve a soft landing for the above example, a buffer should be located at the inflection point ($x = 4.5$ m). This is the position where the piston temporarilly comes to rest before being pushed forward again by residual reservoir gas pressure.

Shock Speeds with the Tuned Driver

Figures 43(a-c) show example experimental shock speeds for each of the three driver conditions described in Table 3. It can be seen that there is no longer the characteristic shock attenuation observed with the previous driver (refer Figure 33). With the 2.0mm and 2.5mm thick diaphragm conditions, target shock speeds are approached, thus achieving the original goals of the study.

It is noted that the three driver conditions detailed in Table 3 were achieved without damage to the facility. Nylon rods were used as the buffer to catch the piston; they are easily cut to a suitable length and have a high energy absorbing capacity. None of these new driver conditions caused damage to the nylon rods, indicating that the combined analytical, numerical and experimental development process managed to safely determine tuned, workable, driver conditions. This case study on the commissioning of the new lightweight piston for X2 has demonstrated a process which can be used to safely develop new driver configurations, and emphasises the use of the simulation code `L1d` to fine tune piston response prior to experimentation.

6.2 Hybrid simulation of the X2 expansion tube

As discussed in Section 2.1, there are three main processes that occur in an expansion tube:

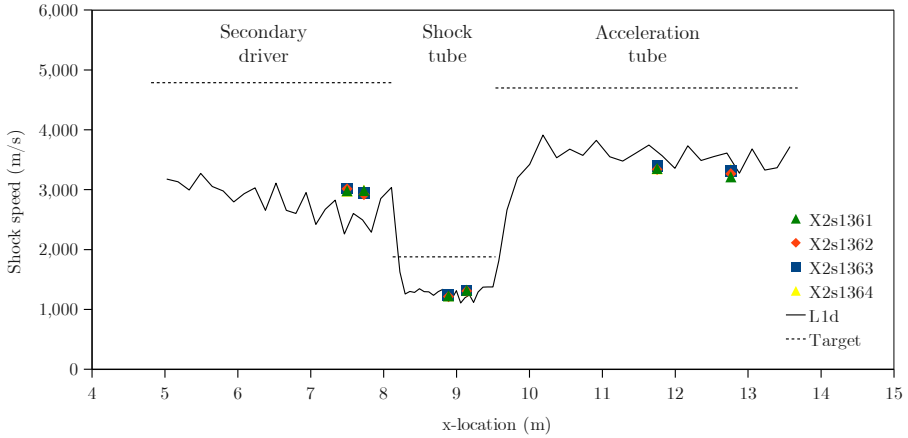

(a) Driver condition LWP-1.2mm-Rev-0

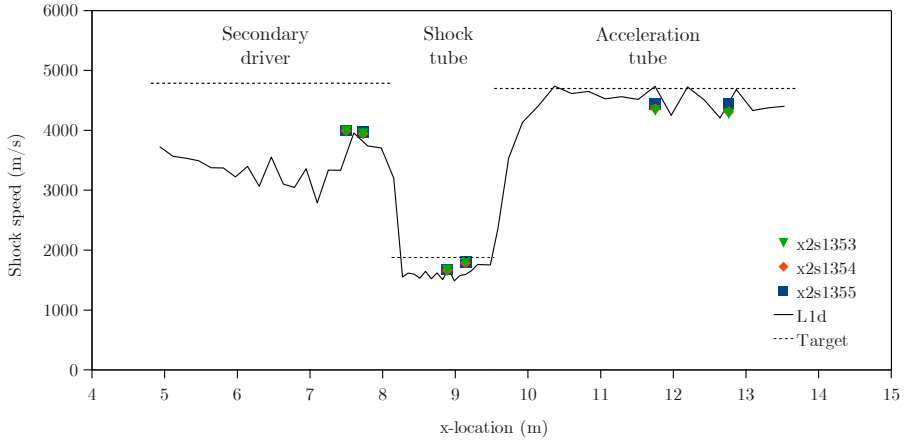

(b) Driver condition LWP-2.0mm-Rev-0

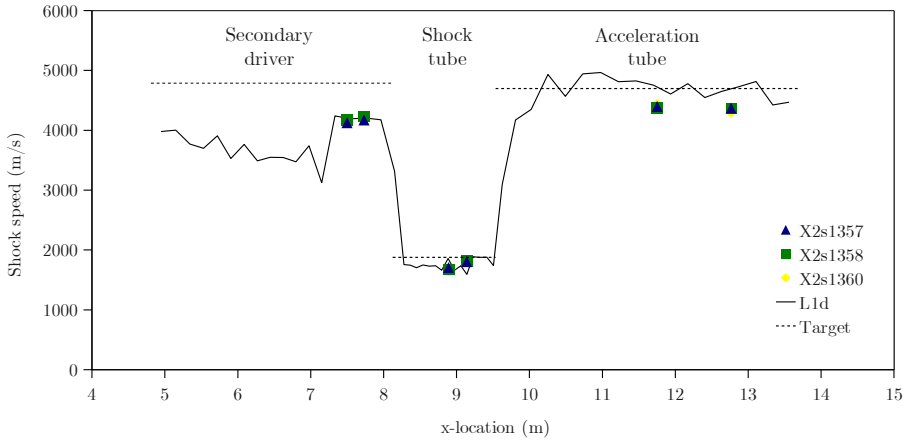

(c) Driver condition LWP-2.5mm-Rev-0

Figure 43: Comparison of experimental, analytical and numerical shock speeds for new tuned lightweight piston driver conditions (refer Table 3). Data points denoted 'X2s...' indicate experimentally measured shock speeds.

1. free-piston compression and primary diaphragm rupture,
2. high pressure, low Mach number shock tube flow and secondary diaphragm rupture, and
3. low pressure, high Mach number acceleration tube, hypersonic nozzle and dumptank expansion.

For superorbital re-entry conditions, the first two stages involve all the important flow processes occurring at reasonably high pressures (p $>$ 100 kPa) and low Mach numbers (M $<$ 4), while the expansion of the test gas into the acceleration tube, nozzle and dump-tank quickly results in low pressures (p $\approx$ 10 kPa) and high Mach numbers (M $\approx$ 10). The hybrid simulation strategy proposed by Jacobs et al [54] makes use of these flow characteristics to simulate the X2 expansion tube in an efficient yet accurate fashion. The in-house quasi-one-dimensional Lagrangian code `L1d` (see Section 5.1) performs well in the high pressure and low Mach number regimes where radial flow variation is small, and is therefore used for simulating the facility up to and including the secondary diaphragm rupture. As the test gas undergoes the unsteady expansion into the acceleration tube post secondary diaphragm rupture, the pressure drops drastically and the flow accelerates. The assumption of a radially uniform flow subsequently breaks down as the boundary layer development limits the shock propagation in accordance with the theory of Mirels [55]. The axisymmetric Navier–Stokes equations are therefore solved with the `Eilmer` code (see Section 5.2) to simulate this critical region of the facility. This hybrid simulation technique has been applied with success to an Earth re-entry condition in the X3 facility [54] and a Titan aerocapture condition in the X2 facility [56]. Here the hybrid simulation technique is applied to a 25 MJ/kg CO_2–N_2 expansion tunnel condition, with additional thermochemical nonequilibrium analyses of the secondary diaphragm rupture and steady nozzle expansion.

Operating Condition

A summary of the initial fill conditions, experimentally measured shock speeds and computationally simulated freestream conditions are shown in Table 4.

Experimental parameters		*Hybrid CFD results*	
Fill conditions		**Simulated shock speeds**	
Reservoir	1.28 MPa Air	Primary shock, $U_{s,st}$	3300 ± 50 m/s
Compression tube	30 kPa 25.0% Ar–75.0% He	Secondary shock, $U_{s,at}$	6310 ± 220 m/s
Shock tube	3.5 kPa 96% CO_2–4% N_2	**Simulated freestream conditions** †	
Acceleration tube	9 Pa Air	Total enthalpy, h_{total}	24.7 ± 0.3 MJ/kg
Diaphragms		Velocity, u	6400 ± 50 m/s
Primary diaphragm	Scored 1.2 mm steel	Pitot pressure, p_{pitot}	65 ± 10 kPa
Secondary diaphragm	13 μm Mylar (or) 10 μm Al	Static pressure, p_{static}	350 ± 50 Pa
Measured shock speeds		Density, ρ	1.6 ± 0.10 g/m^3
Primary shock, $U_{s,st}$	3240 ± 50 m/s	Transrotational temp., T_{tr}	800 ± 100 K
Secondary shock, $U_{s,at}$	6340 ± 230 m/s	Vibroelectronic temp., T_{ve}	1050 ± 100 K
Measured freesteam conditions		Equivalent equil. temp., T	850 ± 100 K
Pitot pressure, p_{pitot}	85 ± 20 kPa	CO_2 mole fraction, X_{CO_2}	0.36 ± 0.04
Static pressure *, p_{static}	500 ± 170 Pa	Mach number, M	12.5 ± 0.5
Test time, t_{test}	150 μs	Unit Reynolds Number, Re/L	2.7×10^4 m^{-1}

Table 4: Fill conditions, shock speeds and freestream conditions for the 25 MJ/kg CO_2–N_2 expansion tunnel condition in the X2 facility.

* Experimental freestream static pressure measured at wall of nozzle exit.

† Simulated freestream conditions are averaged over the central 100 mm diameter core flow and first 100 μs of test time.

The Mars test gas was conservatively taken to be 96% CO_2 – 4% N_2 by volume, as recommended for the ESA *Radiation Workshop* test case TC2-M1 [57]. A sample population of 23 shots with Pitot and static pressure measurements of the test flow are taken to be representative of the nominal condition — the experimental values shown in Table 4 are the means of this population. The calculated freestream conditions are obtained from the hybrid simulation technique to be described below.

Formulation of Hybrid Simulation

The computational approach for expansion tunnel simulation implemented here considers two distinct stages:

1. One-dimensional Lagrangian simulation of the high pressure, low Mach number shock tube flow and secondary diaphragm rupture, and

2. Axisymmetric Navier–Stokes simulation of the low pressure, high Mach number acceleration tube, hypersonic nozzle and dumptank expansion.

The driver gas conditions at primary diaphragm rupture are estimated via an idealised analysis and therefore the piston compression is not simulated. In addition to the main flow simulation, separate analyses of thermochemical nonequilibrium during the secondary diaphragm rupture and steady nozzle expansion are performed. The regions of the X2 facility considered in each simulation component are illustrated in Figure 44.

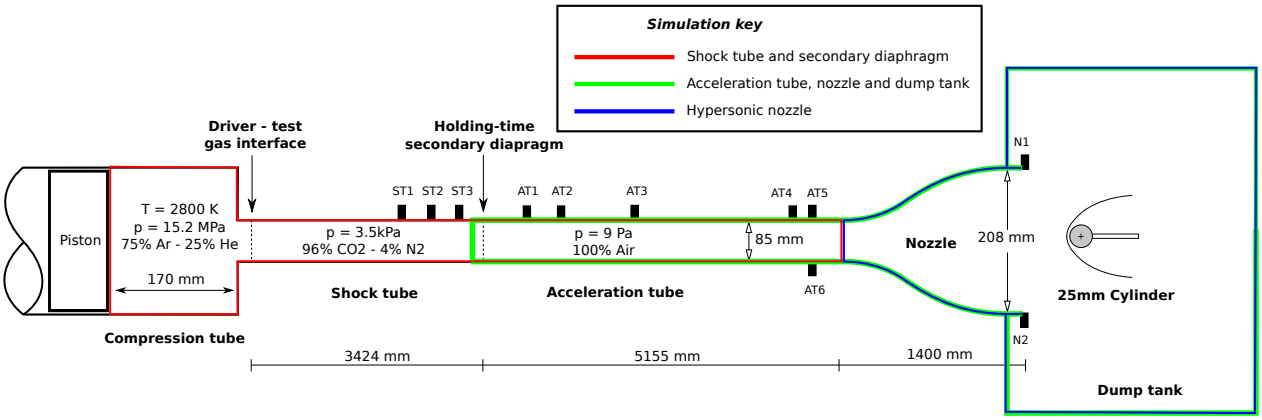

Figure 44: Regions of the X2 facility modelled in the present hybrid simulation technique

Free-piston compression and shock tube flow

The quasi-one-dimensional nature of the `L1d` geometry can result in boundary layer heat loss being significantly under-estimated. Previous attempts at modeling the free-piston compression of the driver gas have demonstrated this inadequacy [58], with the driver gas temperature at primary diaphragm rupture being unreasonably high. The `L1d` simulation of the shock tube flow is therefore begun at the moment of primary diaphragm rupture. The driver gas pressure and slug-length at rupture are obtained from an idealised model of the free-piston compression, whilst the temperature is obtained parametrically by matching the experimentally measured primary shock speed. Momentum loss at the primary diaphragm station area change is accounted for through a loss-per-unit-length factor K_L of 0.25. The CO_2–N_2 test gas is described by an equilibrium equation-of-state using the curve fits provided by the `CEA` program [59], as are the respective transport coefficients. The Ar–He driver gas is described as a mixture of ideal gases.

Light secondary diaphragm rupture

When the primary shock through the stagnant test gas reaches the light secondary diaphragm, the first few millimeters of shock-processed test gas are stagnated by the resulting reflected shock. For the condition at hand the ratio of the stagnated to freestream density of the test gas is approximately $10^4 : 1$ — taking area change into account and using the freestream conditions from Table 4, the observed 150 μs of test flow originates from within the first 2 mm of stagnated test gas. It follows that the subsequent expansion of this very small test gas volume through the acceleration tube and nozzle must be modeled accurately.

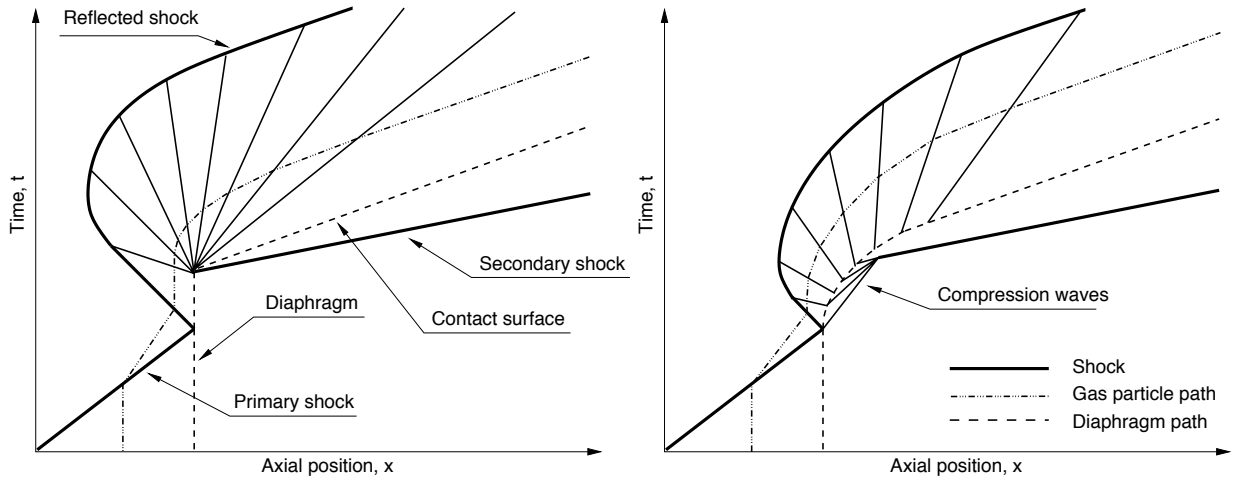

(a) Holding time model

(b) Inertial diaphragm model

Figure 45: Space-time diagrams of light secondary diaphragm rupture in an expansion tube (adapted from Bakos and Morgan [60]).

Diaphragms are typically modeled in `L1d2` as fixed-wall boundary conditions that are held in place for a small period of time to allow the reflected shock to form before being released. This method is referred to as the holding-time model, and is widely implemented due to its relative simplicity. Bakos and Morgan [60] demonstrated the limitations of the holding-time model through comparison with an inertial diaphragm model. Space-time representations of both the holding-time and inertial diaphragm models are shown in Figure 45. The inertial diaphragm model represents the diaphragm as an ideal piston — the diaphragm shears cleanly at the tube wall, remains planar during its motion and provides only inertial resistance to the expanding test gas. Where a test gas particle immediately upstream of the secondary diaphragm experiences an infinite rate of expansion under the holding-time model, the inertial diaphragm model shows the contact surface must accelerate to an asymptotic limit over a finite period of time. The duration a test gas particle spends in the unsteady expansion directly determines the degree of thermochemical relaxation experienced — high expansion rates will result in frozen thermochemistry, while low expansion rates will tend towards equilibrium.

The light secondary diaphragms used for the sample population shots were 13 μm Mylar sheets weighing approximately 70 μg — the assumption that this sheet will stay intact through the entire test gas expansion is clearly invalid. A decaying inertial diaphragm model is therefore proposed for the present analysis, where the diaphragm reduces in mass exponentially after coming in contact with the hot stagnated test gas. The expression for the diaphragm mass m rate-of-change is taken to be:

$$\frac{dm}{dt} = \begin{cases} f_{\text{decay}} \times m \text{ for } m > m_{\text{limit}} \\ 0 \text{ for } m \leq m_{\text{limit}} \end{cases} \tag{2}$$

where f_{decay} is a time constant and m_{limit} an imposed lower mass limit to prevent numerical instabilities. Simulations of the secondary diaphragm rupture and subsequent unsteady expansion are performed for holding-time, inertial diaphragm and decaying inertial diaphragm models with finite-rate chemistry using the `L1d` code.

Acceleration tube, nozzle and dumptank flow

The axisymmetric flow solver `Eilmer` is used for the low pressure, high Mach number acceleration tube, nozzle and dumptank flow. The computational domain is subdivided into a number of interconnected blocks, as illustrated in Figure 46, which allows the calculation to be parallelised over a distributed memory cluster computer.

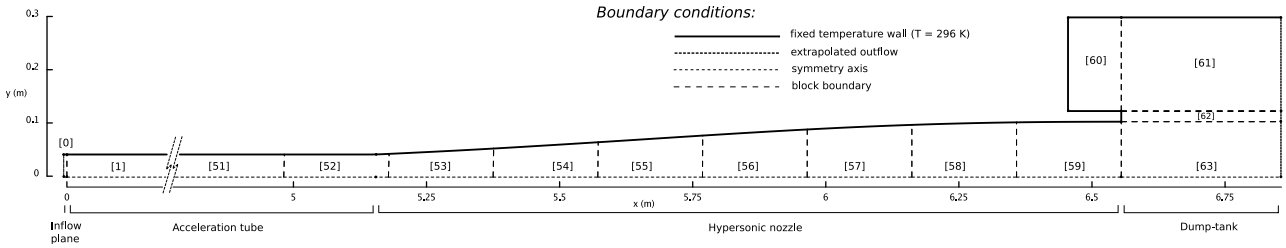

Figure 46: Computational domain for axisymmetric simulation of the X2 expansion tunnel downstream of the secondary diaphragm.

Although the holding-time secondary diaphragm rupture model is expected to underestimate test gas recombination through the unsteady expansion, it provides a simple pre-rupture flowfield that can be easily used to initialise the multidimensional simulation. Using a holding-time of 10 μs the stagnated test gas slug is calculated to be 4 mm long at rupture. A 4 mm block thus precedes the acceleration tube, as shown in Figure 46, which is filled with the equilibrium stagnated test gas conditions. The upstream face of this block is a transient inflow boundary condition, applying the one-dimensional flow solution from the `L1d` simulation uniformally over the inflow plane.

Although thermal nonequilibrium is anticipated to occur during the nozzle expansion process, the inclusion of both thermal and chemical nonequilibrium for such a large-scale simulation is computationally prohibitive. Thermal equilibrium is therefore assumed for the Navier–Stokes simulations of the post-secondary diaphragm rupture flow, while separate inviscid simulations of the hypersonic nozzle are performed with the two-temperature model proposed by Park [61, 62]. The stagnated test gas upstream of the secondary diaphragm just prior to rupture contains negligible ionic species, and therefore only the neutral dissociation and exchange reactions listed in Table 5 (reactions 1 to 16) are included in the Navier–Stokes simulations.

Results and comparison with experiment

Lagrangian shock tube simulations A driver slug length of 170 mm and piston velocity of 50 m/s at primary diaphragm rupture was determined through an idealised model of the free-piston compression. A driver slug temperature of 2800 K was selected through the matching of experimental conditions in a parametric analysis. A comparison of the `L1d2` and experimental static pressure history from shot x2s248 is shown in Figure 47a. Shock arrival time observed in experiment at each transducer location is matched by the simulations within experimental and modeling uncertainties. Although the experimental data shows a higher initial pressure rise for transducer ST1, excellent agreement is shown for the first 800 μs of flow 0.5m downstream at ST3. A space-time representation of logarithmic pressure contours is shown in Figure 47b. The tail of the expansion fan eminating from the primary diaphragm station can be seen to reflect off the compression–shock tube area change and eventually coalesce with the shock at $t = 700\,\mu$s. Stagnation conditions behind

	Neutral reactions	Activation energy		Ionic reactions	Activation energy
Dissociation reactions			*Associative ionisation reactions*		
1	$CO_2 + M \Longleftrightarrow CO + O + M$	-526 kJ/mol	17	$N + O \Longleftrightarrow NO^+ + e^-$	-265 kJ/mol
2	$CO + M \Longleftrightarrow C + O + M$	-1073 kJ/mol	18	$O + O \Longleftrightarrow O_2^+ + e^-$	-670 kJ/mol
3	$N_2 + M \Longleftrightarrow N + N + M$	-941 kJ/mol	19	$C + O \Longleftrightarrow CO^+ + e^-$	-275 kJ/mol
4	$O_2 + M \Longleftrightarrow O + O + M$	-497 kJ/mol	*Charge exchange reactions*		
5	$NO + M \Longleftrightarrow N + O + M$	-628 kJ/mol	20	$NO^+ + C \Longleftrightarrow NO + C^+$	-193 kJ/mol
6	$CN + M \Longleftrightarrow C + N + M$	-590 kJ/mol	21	$O_2^+ + O \Longleftrightarrow O^+ + O_2$	-150 kJ/mol
7	$C_2 + M \Longleftrightarrow C + C + M$	-581 kJ/mol	22	$NO^+ + N \Longleftrightarrow O^+ + N$	-106 kJ/mol
Exchange reactions			23	$NO^+ + O \Longleftrightarrow O_2^+ + N$	-404 kJ/mol
8	$NO + O \Longleftrightarrow N + O_2$	-162 kJ/mol	24	$CO + C^+ \Longleftrightarrow CO^+ + C$	-261 kJ/mol
9	$N_2 + O \Longleftrightarrow N + O_2$	-319 kJ/mol	25	$O_2 + C^+ \Longleftrightarrow O_2^+ + C$	-78 kJ/mol
10	$CO + O \Longleftrightarrow C + O_2$	-575 kJ/mol	*Electron-impact ionisation reactions*		
11	$CO + C \Longleftrightarrow C_2 + O$	-48 kJ/mol	26	$C + e^- \Longleftrightarrow C^+ + e^- + e^-$	-1087 kJ/mol
12	$CO + N \Longleftrightarrow CN + O$	-321 kJ/mol	27	$O + e^- \Longleftrightarrow O^+ + e^- + e^-$	-1318 kJ/mol
13	$N_2 + C \Longleftrightarrow CN + N$	-193 kJ/mol			
14	$CN + O \Longleftrightarrow NO + C$	-121 kJ/mol			
15	$CN + C \Longleftrightarrow C_2 + N$	-11 kJ/mol			
16	$CO_2 + O \Longleftrightarrow O_2 + CO$	-231 kJ/mol			

Table 5: Neutral and ionic chemical reactions from the CO_2 – N_2 reaction scheme of Park et al [62] (Note that the photo-ionisation reactions have been omited).

the reflected shock at diaphragm rupture were determined to be 10.3 MPa and 4370 K with an equilibrium CO_2 fraction of 30% by mass.

Secondary diaphragm rupture analysis Holding-time, inertial diaphragm and decaying inertial diaphragm models were compared in the analysis of secondary diaphragm rupture. Space-time plots of shock propagation obtained from finite-rate `L1d`simulations with the three secondary diaphragm models considered are shown in Figure 48a with experimental shock arrival times overlaid. The experimental transducer shock arrival times are bounded by the holding-time and inertial diaphragm solutions, with the holding-time model predicting the strongest secondary shock as expected. Implementing a decaying inertial diaphragm model with a time constant f_{decay} of $5 \times 10^4\ s^{-1}$ was found to match the secondary shock propagation observed in experiment.

CO_2 mass fraction distributions at $t = t_{rupture} + 150\ \mu s$ for each of the Lagrangian simulations conducted are shown in Figure 48b. The test gas composition was found to be chemically frozen from this time onwards for all diaphragm models. The holding-time model gives the lowest levels of CO_2 recombination, with a much more pronounced variation over the slug when compared to the relatively uniform inertial-diaphragm results. An unrealistically large initial rate of expansion for the test gas particles immediately upstream of the secondary diaphragm gives insufficient time for any recombination to occur before freezing occurs. The holding-time recombination levels only begin to approach that of the inertial diaphragm simulations at the very end of the test slug. The inertial diaphragm model with no mass decay shows significantly higher levels of CO_2 recombination and a more uniform distribution. The decaying inertial diaphragm model gives recombination levels bounded by the previous two models as expected, with an average CO_2 mass fraction in the test slug of 0.46. Assuming that the decaying inertial diaphragm model closely represents the physical rupture behaviour, implementing a holding-time rupture model to initialise the Navier–Stokes simulations will result in CO_2 levels being underpredicted by between 25% and 4% over the test time.

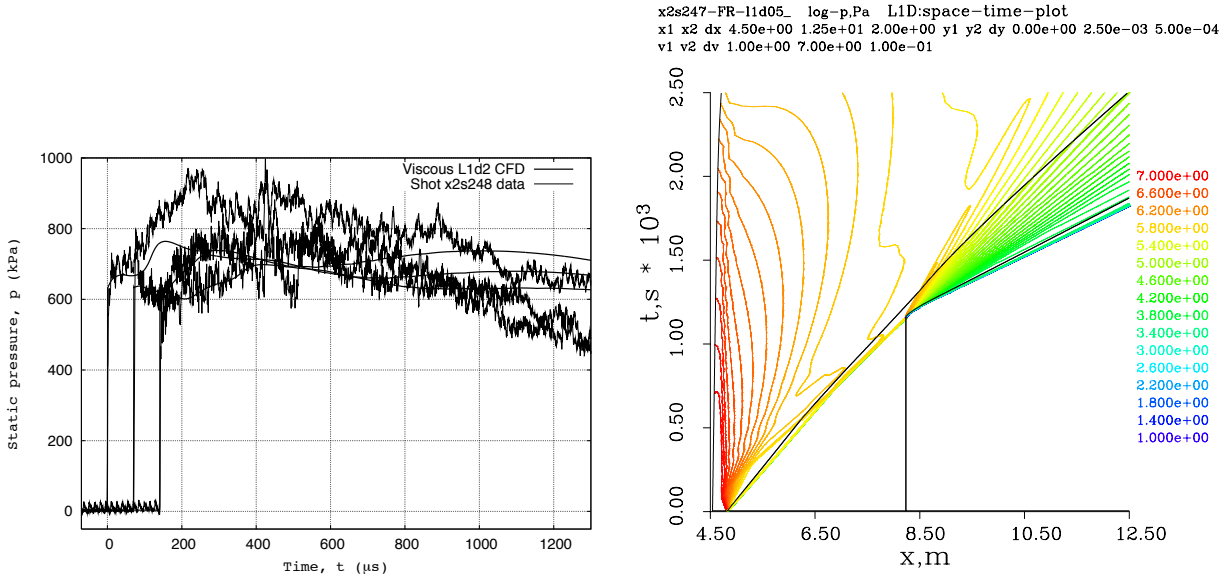

(a) Comparision of simulated and experimental static pressure traces in the shock-tube

(b) Space-time diagram of logarithmic pressure contours.

Figure 47: Results from quasi-one-dimensional Lagrangian shock tube simulation with equilibrium chemistry.

Navier-Stokes expansion tunnel simulation Viscous Navier-Stokes simulations of the expansion tunnel flow were conducted with finite-rate chemistry and a pre-rupture flowfield described by the `L1d` solution with a holding-time secondary diaphragm. Initial simulations with 37 $\times$ 4500 cells in the acceleration tube and a stagnated test gas slug length of 2mm resulted in unphysical pockets of hot, low density gas forming along the axisymmetric axis. Increasing the cell distribution to 43 $\times$ 5155 (1 mm squares, average) reduced this phenomena slightly, however disturbances were still observed during the test time. The test gas slug length was increased to 4 mm, corresponding to a hold-time of 10 μs, and the disturbances no longer formed during the test time. The stability of the flow during the test time for this final simulation is illustrated in the contours of pressure through the nozzle, Figure 49. The freestream conditions from this simulation are shown in Table 4.

A comparison of the `mbcns2` solution with experimentally obtained pressure traces is shown in Figure 50. The simulated secondary shock propagation shown in Figure 50a closely matches that of shot x2s247 which is close to the mean of the sample population. Good agreement with experiment is shown for both static and Pitot pressure at the nozzle exit for the first 200 μs of flow, Figures 50b and 50c. The simulated Pitot pressure profile 100 mm downstream of the nozzle exit shows reasonable agreement with that obtained through the experimental Pitot pressure survey, Figure 50d. For the central 100 mm of flow a test article is likely to occupy slight property variation exists, most noticeably at the extremities which has Pitot pressure 10% higher than at the central axis. Overall, the multidimansional simulation shows sufficient correlation with experiment to proceed with further validation through bluntbody shock layer simulations.

Nonequilibrium nozzle expansion analysis The averaged nozzle entrance conditions from the viscous, thermal equilibrium expansion tunnel simulation were used as initial conditions for inviscid, thermal nonequilibrium simulations of the hypersonic nozzle expansion. Test gas temperature contours through the nozzle after 800 μs of flow are shown in Figure 51a, while the respective centreline temperature profile is shown in Figure 51b. Both temperatures along the centreline are seen to remain constant until the Mach cone arrives 250 mm downstream of the nozzle entrance. The transrotational temperature then begins to drop rapidly as

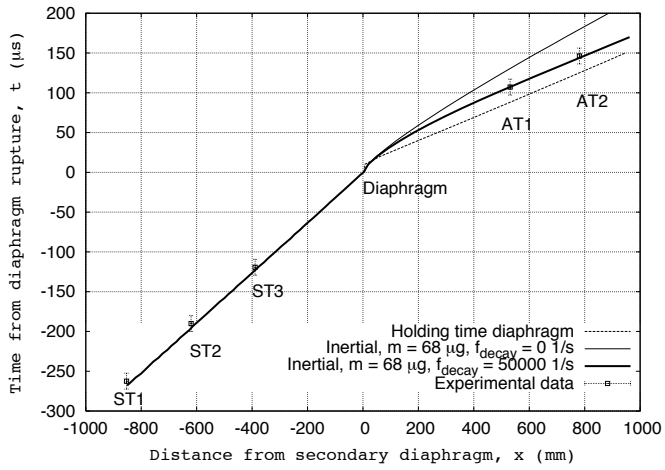

(a) XT diagram from ST1 to AT2.

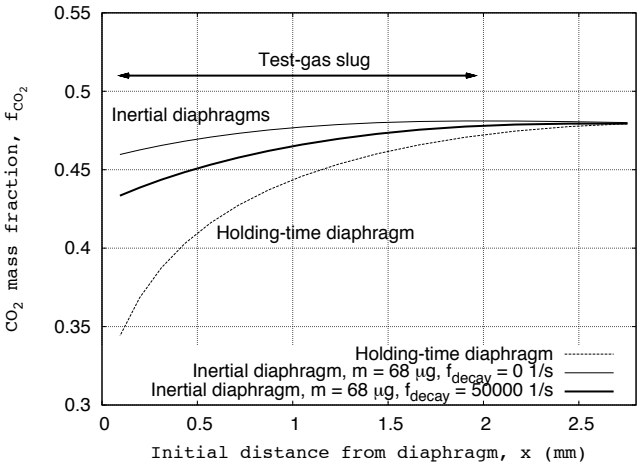

(b) Test gas CO_2 mass fractions 150 μs after rupture.

Figure 48: Comparison of shock propagation and test gas recombination for various light secondary diaphragm models.

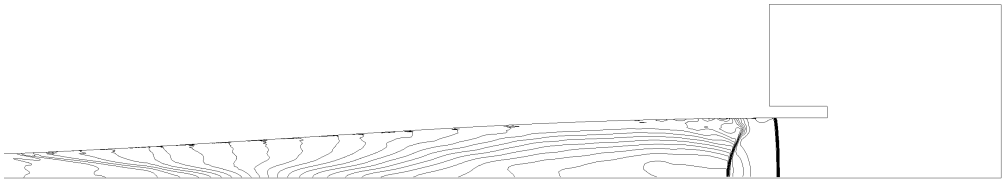

(a) $t = t_{\text{rupture}} + 1050\,\mu s$

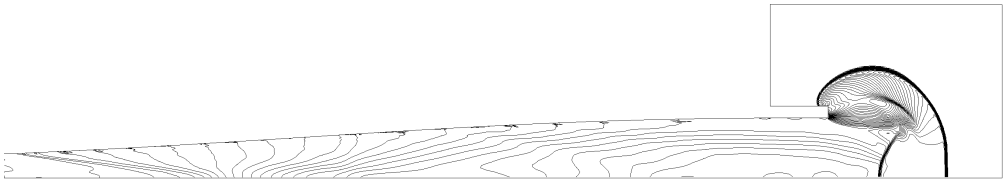

(b) $t = t_{\text{rupture}} + 1100\,\mu s$

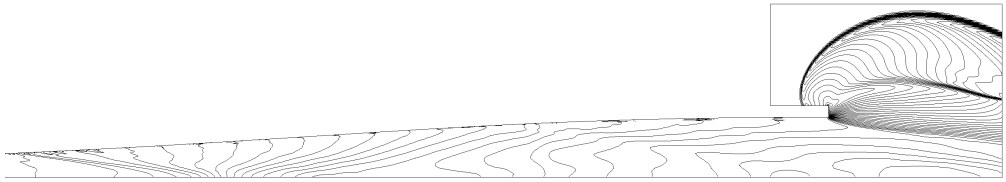

(c) $t = t_{\text{rupture}} + 1150\,\mu s$

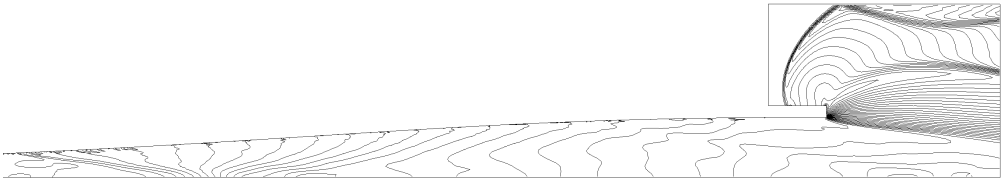

(d) $t = t_{\text{rupture}} + 1200\,\mu s$

Figure 49: Static pressure contours through the hypersonic nozzle during test gas expansion.

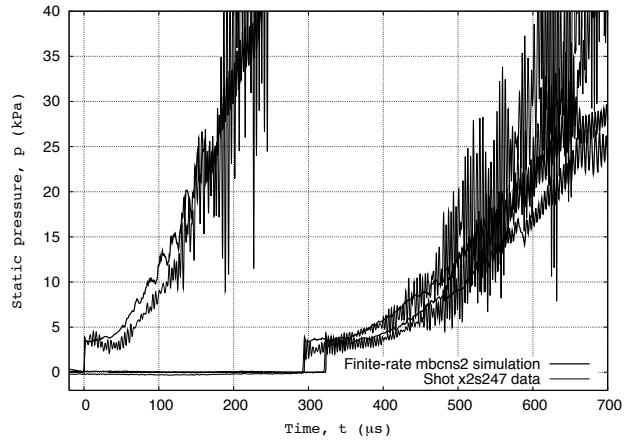

(a) Static pressure history at AT3, AT4 and AT5.

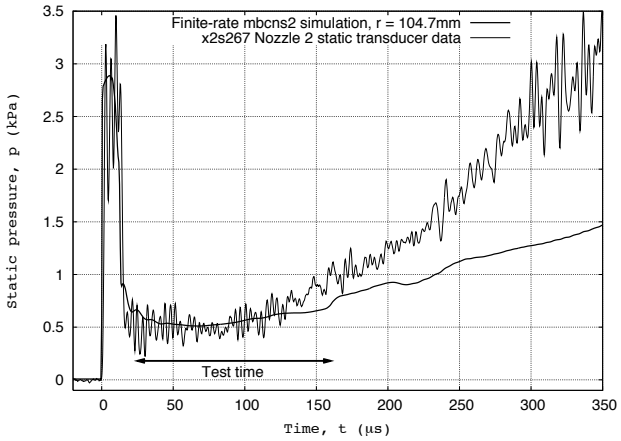

(b) Static pressure history at nozzle exit.

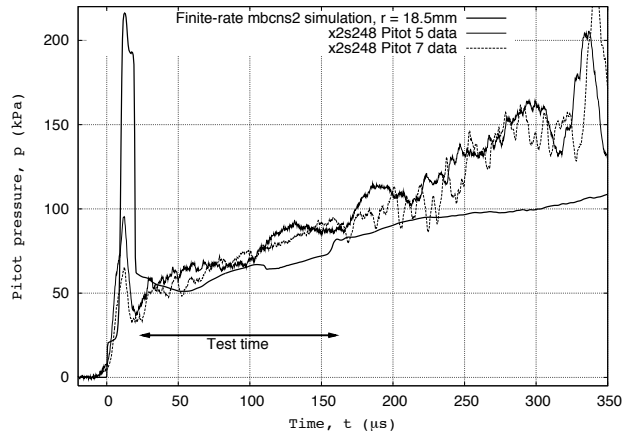

(c) Pitot pressure history 100 mm downstream of nozzle exit.

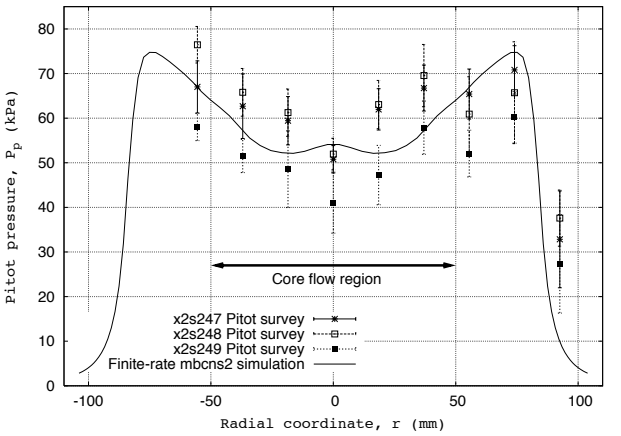

(d) Pitot pressure profile 100 mm downstream of nozzle exit at $t = t_{\text{rupture}} + 1175\mu s$.

Figure 50: Comparison of computational and experimental pressures through the acceleration tube and nozzle.

the test gas expands, while the vibroelectronic temperature relaxes at a much lower rate. After 800 mm the transrotational temperature along the centreline is essentially frozen at 800 K while the vibroelectronic temperature continues to slowly relax. The flow close to the nozzle wall remains in a state of thermal equilibrium at 1100 K through the entire length due to a much weaker expansion than at the centreline. Slightly increased relaxation begins to occur as the test gas expands into the dump tank, resulting in a final temperatures 100 mm downstream of the nozzle exit of $T_{ve} \approx 1050$ K and $T_{tr} \approx 800$ K.

Quality of the Solution A hybrid simulation technique for the X2 expansion tube incorporating a one-dimensional Lagrangian simulation of the shock tube and secondary-diaphragm and an axisymmetric Navier–Stokes simulation of the acceleration tube, nozzle and dump-tank has been applied to a 25 MJ/kg CO_2–N_2 condition. Good agreement with experimentally measured static pressure traces and shock speeds was obtained in both the shock and accerlation tubes, and Pitot pressure was also found to be accurately predicted in the test-section. Although the application of a simplified holding-time model allows the shock propagation and pressure levels to be accurately reproduced in the Navier–Stokes simulation, test gas recombination following secondary diaphragm rupture was found to be under predicted by as much as 25 % when compared

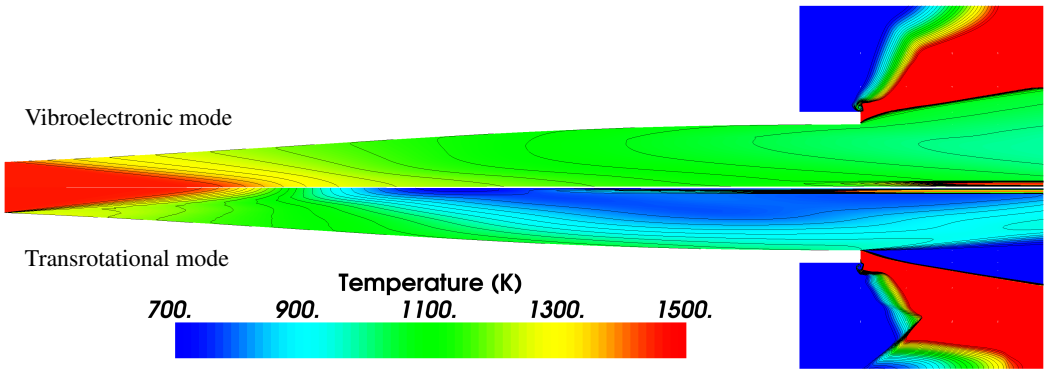

(a) Contours of temperature.

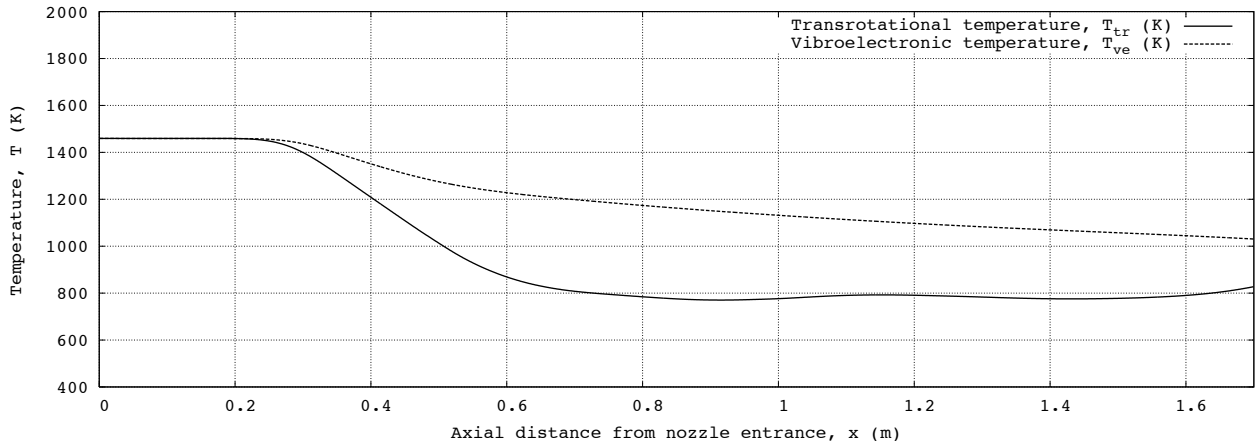

(b) Centreline temperature profiles.

Figure 51: Test gas temperature distributions through the hypersonic nozzle after 800 μs of flow.

to a simulation considering an inertial secondary diaphragm. Furthermore considerable thermal nonequilibrium is shown to develop through the steady nozzle expansion, with T_{ve} and T_{tr} deviating by 24 % and -6 % respectively from the equilibrium temperature T_{eq}. Therefore while the density, pressure and velocity obtained via the hybrid simulation technique is considered to be accurate, the species mass-fractions and thermal equilibrium temperature are considered approximate only.

6.3 Axisymmetric simulation of the X2 shock tube

Experiment discription

A comprehensive set of shock tube experiments with a representative Titan test gas (98% N_2 & 2% CH_4 by volume) over a pressure and velocity range of 2 to 1000 Pa and 4 to 10.5 km/s respectively were conducted by Brandis [63] in the X2 facility. Following the work of Gollan [64, 65], a 1 Torr 5.7 km/s condition was the focus of a recent computational study [66] where the CN Violet radiation intensity predicted by a one-dimensional and an axisymmetric simulation were compared with experiment. The aim of the study was to assess the assumption of one-dimensional variation of properties during the test-time, as the optical line-of-sight passes through the expanding boundary layer and Mach cone in the test section.

Table 6 summarises the fill conditions, shock speeds and spectral measurements performed in the X2 experiments that were simulated.

Shot number	x2s522	x2s645
Driver gas composition *	86.0% He, 14.0% Ar	
Primary diaphragm burst pressure	15.1 MPa	
Test gas composition *	98% N_2, 2% CH_4	
Shock speed, U_s †	5697 ± 54 m/s	5658 ± 53 m/s
Pressure, p_∞	133 ± 0.5 Pa	
Exposure time, $t_{ex.}$	100 ns	
Spectrometer range	308-450 nm	

Table 6: Two X2 shots targeting a 1 Torr 5.7 km/s Titan entry condition

* Gas percentage compositions are by volume

† Given shock speed is that between transducers AT5 and AT7 (see Figure 3)

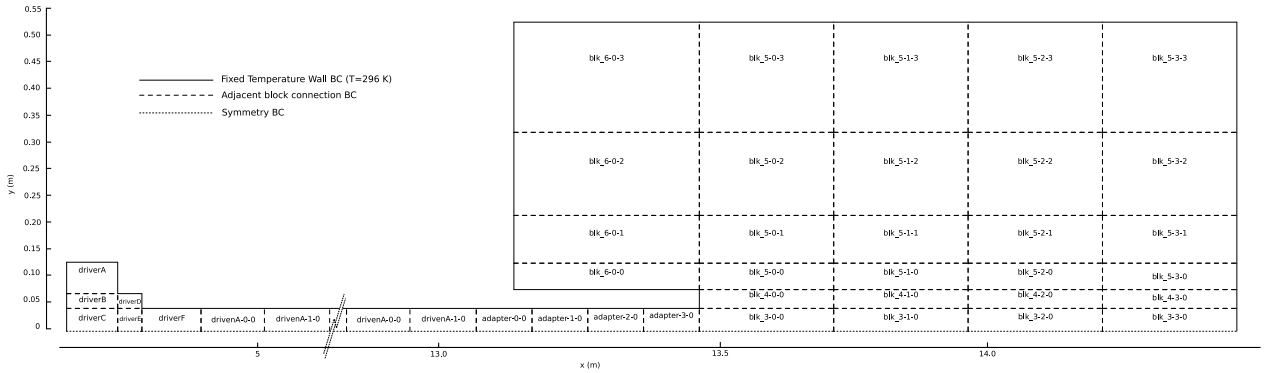

Figure 52: X2 computational domain for axisymmetric Navier–Stokes simulation of shot x2s522

Two shots x2s522 and x2s645 were both performed with an initial test gas pressure of approximately 1 Torr targeting a shock speed of 5.7 km/s; the measured shock speeds matched this within the bounds of measurement uncertainty. Although the pressure of this condition is an order of magnitude higher than that of Huygens-type direct entry peak heating [67], it is a useful condition for investigating the chemical kinetics of Titan gas closer to thermochemical equilibrium.

Formulation of Axisymmetric Simulation

The axisymmetric Navier–Stokes simulation technique implemented here is based on that described in Ref. [64], however the driver gas conditions are assumed to be uniform (T=3450 K, p=15.1 MPa, u=0 m/s) at diaphragm rupture for the present work. A single-temperature gas model is implemented alongside the Gökçen [68] chemical reaction scheme where the ionic reactions have been omitted. This relatively low order thermochemistry model was used due to computational resource constraints. The computational domain for the axisymmetric Navier–Stokes simulation of shot x2s522 is presented in Figure 52. The computational domain extends from the front piston face to 1 m into the dump-tank; the remaining length of the dump-tank is not included.

Again, the simulations were performed with the `mbcns2` code described in Section 5.2. The computational domain is decomposed into 160 roughly equally sized blocks – 5 in the compression tube cavity, 123 along the shock-tube and 32 in the dump-tank. Two grid resolutions were considered – (a) 20×2000 cells in the shock-tube and (b) 40×4000 cells in the shock-tube. The cell discretization in the compression cavity and dump-tank are matched to the shock tube on a cell per unit area basis. The higher resolution

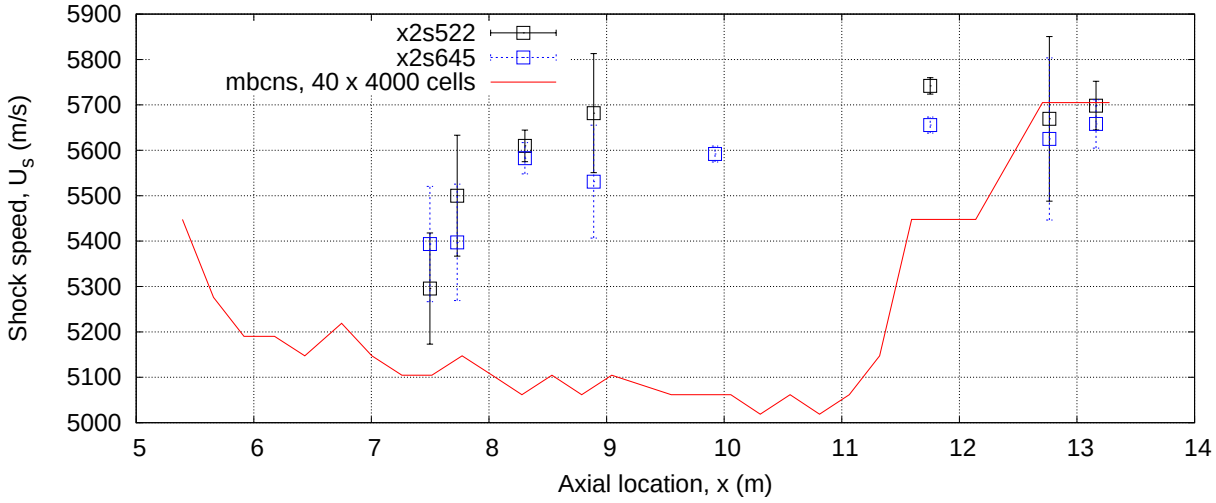

Figure 53: Comparison of shock-speed from experiments and simulations for the 1 Torr X2 condition

simulation has a total of 580,180 cells. The simulations were run on 40 quad-core Intel Woodcrest nodes and the 40×4000 simulation required approximately 140 hours for completion.

Results and comparison with experiment

Figure 53 compares the shock-speeds measured from experiment and those obtained from the computational simulations. The shock speeds from experiment are determined by locating the arrival time of the shock at each of the 8 pressure transducers along the shock tube and calculating the time-of-flight in between each pair. The spatial uncertainty is 1 mm and the temporal uncertainty is nominally 1 μs. Although the 40×4000 cell simulation agrees with the experimentally measured shock speed of approximately 5.7 km/s at the tube exit, the shock propagation through the shock tube is quite different. The experiments show a quick initial rise and then plateau in shock speed in the first 2 meters after the primary diaphragm, whilst the sudden rise in the simulations is only 2 meters from the tube exit. The sudden rise in shock speed is thought to be due to the reflected expansion wave catching-up with and accelerating the shock. The location of the shock/expansion wave interaction is determined largely by the initial temperature of the driver gas – for the present simulations this was set to 3,450 K which is approximately the isentropic compression temperature. If the driver gas compression process is not adiabatic the temperature of diaphragm rupture may be substantially less, and the the shock/expansion wave interaction location would be different.

The simulated and x2s522 static pressure traces at transducers ST1, AT4, AT5 and AT7 are compared in Figures 54a to 54d respectively. Generally the quantitative agreement with experiment is quite good. Of particular note, however, is the discrepancy in expansion wave arrival time at the ST1 transducer – in the experiment the arrival time is approximately 550 μs, while in simulation it is 600 μs. Such a large discrepancy so close to the primary diaphragm (3.5 m) indicates that the expansion of the driver gas is not being modeled correctly. By the AT4 transducer the simulated shock is in agreement with experiment, and this is reflected in the close agreement in the pressure histories at AT4, AT5 and AT7. Most critically, the post-shock static pressure level of approximately 50 kPa at the final transducer before the tube exit is matched almost exactly.

As described in Ref. [63], the spectral measurements in the X2 facility considered in the present work are made as the shock is expanding from the shock tube exit into the dump-tank (see Figure 1). Figure 55 displays CN mass fraction contours from the `mbcns2` simulation of the 1 Torr Titan condition as the shock emerges into the test section for spectral measurement. The spectral measurements are taken at approximately t=1720 μs. Comparing Figures 55a and 55e, the expansion of the shock layer into the test section is

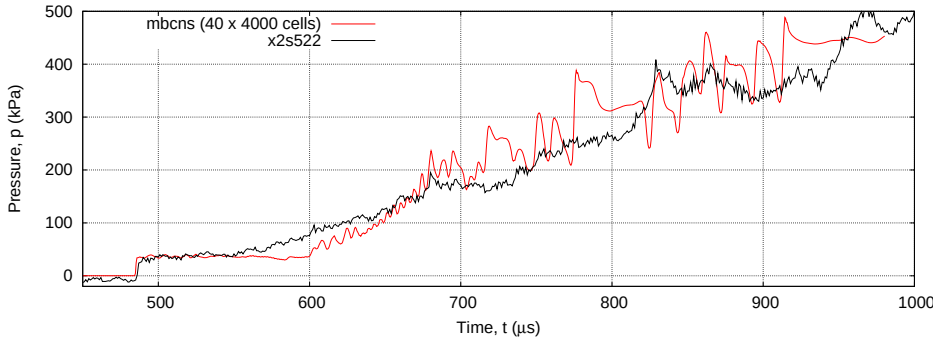

(a) ST1, x=7.381 m

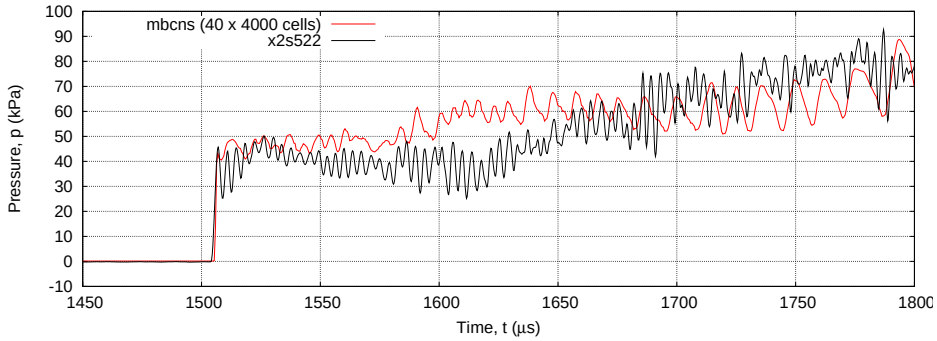

(b) AT4, x=12.675 m

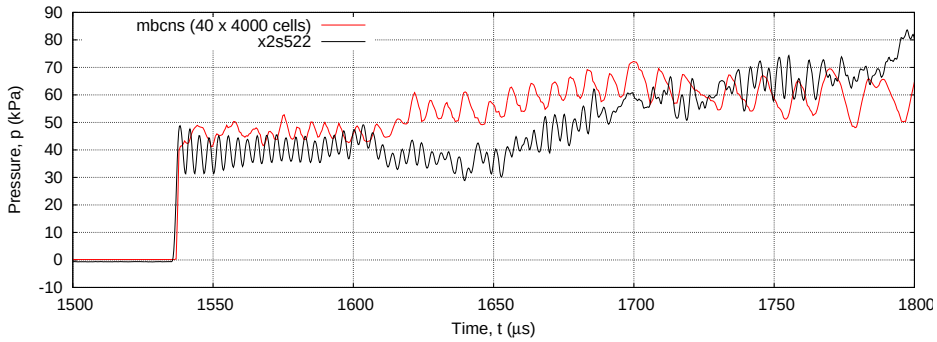

(c) AT5, x=12.855 m

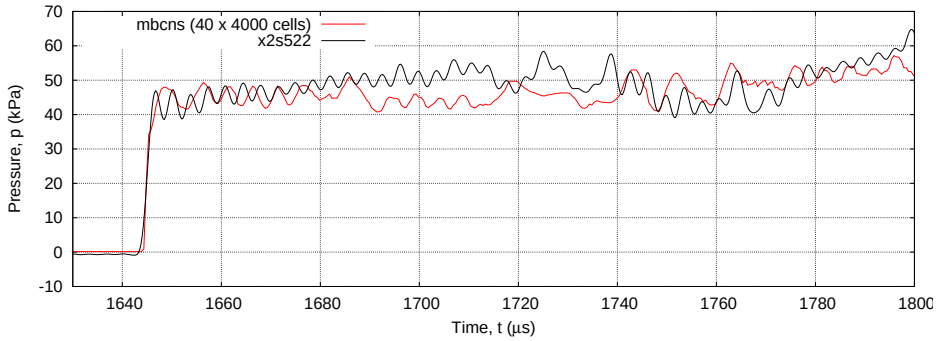

(d) AT7, x=13.469 m

Figure 54: Comparison of simulated and experimentally measured static pressure histories for the 1 Torr condition

seen to alter the quasi-one-dimensional nature of the flow present inside the tube.

To evaluate the assumption that the emerging shock-layer remains approximately one-dimensional until the spectral measurements are taken, one-dimensional post-shock relaxation simulations with the `poshax` code are compared with the axisymmetric `mbcns2` simulations. Both simulations use the aforementioned 1 temperature thermal model with the reduced Gökçen [68] chemistry scheme. Figures 56a through 56c present comparisons of temperature, CN mole fraction and radiative intensity profiles, respectively, for the 1 Torr Titan condition in X2. The experimentally measured intensity profile from shot x2s645 is overlayed on Figure 56c and has been scaled to match the order of magnitude of the one temperature simulations. While the one-dimensional simulation uses the Rankine-Hugoniot relations to calculate the gas condition directly behind the shock (shock-slip is not considered), the finite-volume Navier–Stokes simulation captures the shock over a number of cells resulting in a diffused shock front. Furthermore the curvature of the shock as it emerges into the test section is only modelled in the axisymmetric simulations. These effects are evident in Figures 56a and 56b, where the change in temperature and CN mass fraction across the shock are more gradual in the Navier–Stokes simulations and peak at lower values. Consequently the calculated radiation intensity profile from the Navier–Stokes simulation exhibits a qualitative improvement over that from the one-dimension post-shock relaxation simulation, Figure 56c. The ratio of peak to equilibrium intensity is much closer in the Navier–Stokes simulation and the rise to the peak intensity immediately behind the shock is more realistic.

Quality of the Solution

The shock speed and static pressure levels calculated at AT5 and AT7 matched that measured in experiment, however the shock speed was under-predicted in the early stages of shock propagation. A better representation of shock propagation would require an axisymmetric simulation of the free-piston compression rather than the assumption of uniform driver properties at primary diaphragm rupture. Post-processing of the Navier–Stokes simulation data resulted in a radiation intensity profile that gave improved qualitative agreement with experiment compared to that from a one-dimensional post-shock relaxation simulation.

7 HAYABUSA RE-ENTRY OBSERVATIONS

When an actual flight opportunity presented itself with the return of the JAXA Hayabusa Sample Return Capsule on the 13th of June 2010, the community worked together to mount an airborne and ground-based observing campaign to study the entry. Hayabusa was scheduled to enter the atmosphere above Australia late in the evening on the 13th of June 2010 with a speed of about 12.2 km/s, the fastest re-entry since ‘Stardust’ in 2006. Observations of the Stardust re-entry yielded a significant body of data suitable for testing computational models[69] so, with JAXA and Australian approval, NASA deployed the DC-8 Airborne Laboratory to the Woomera Test Range to provide a high altitude platform for Hayabusa irradiance measurements. A research team from the University of Southern Queensland and the University of Queensland contributed to this mission a near-UV slit-less spectrograph, called the Australian Ultraviolet Spectrograph (AUS). At the same time, teams of researchers from the University of Queensland, The University of Southern Queensland, and the University of New South Wales (Australian Defence Force Academy) were positioned at Tarcoola and Coober Pedy for ground-based observations of the re-entry [70].

The Australian Ultraviolet Spectrograph (AUS) [71] was developed in an effort to provide near-UV emissions spectra from the Hayabusa re-entry to augment the existing Stardust data base. For the AUS instrument to make a useful contribution in this respect, it was determined that the CN and N_2^+ structures would need to be resolved, the deduced spectral emissions should have an absolute calibration reference, and reliable results were required throughout the re-entry process, including the time of peak heating.

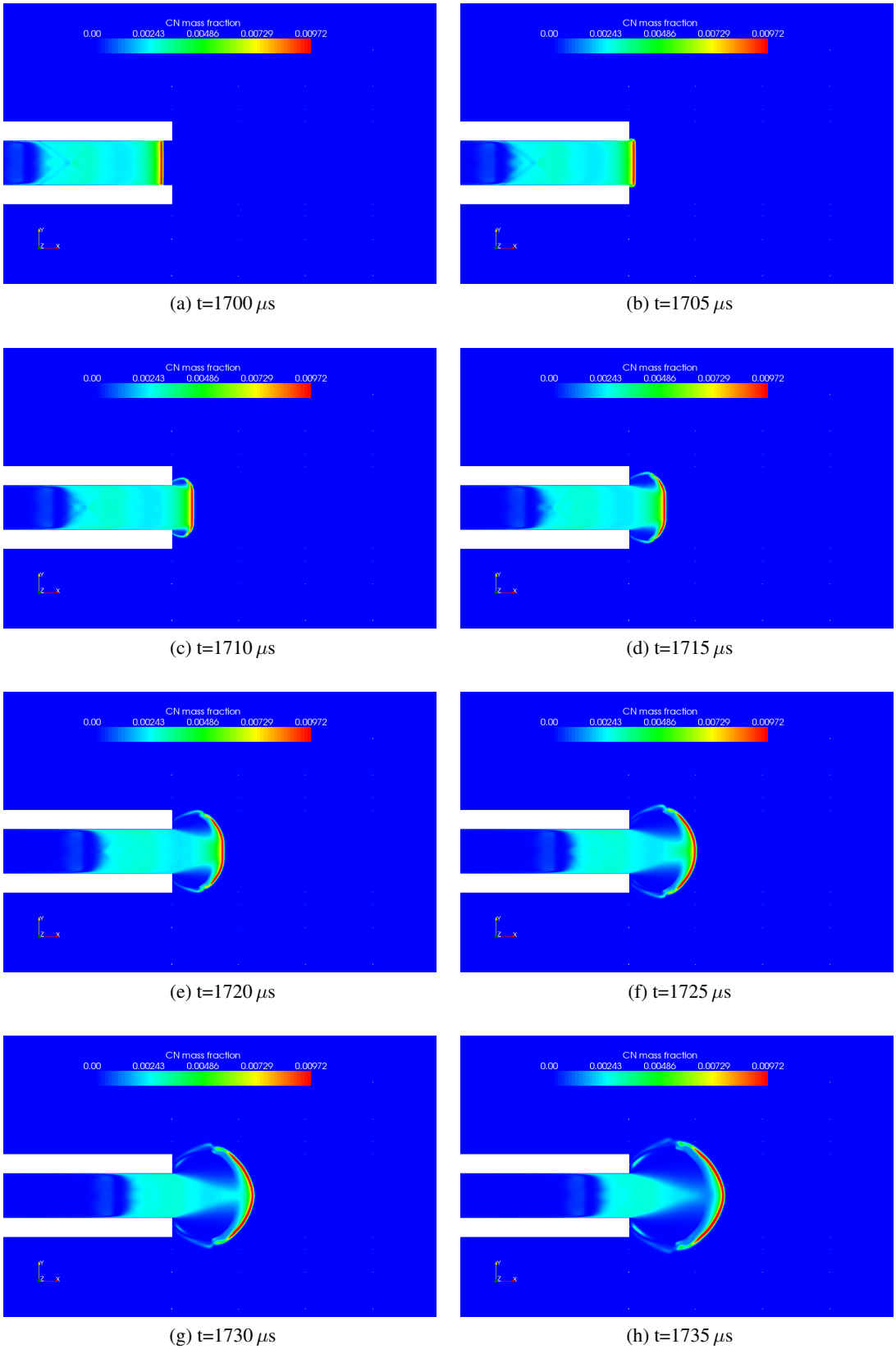

(a) t=1700 μs (b) t=1705 μs

(c) t=1710 μs (d) t=1715 μs

(e) t=1720 μs (f) t=1725 μs

(g) t=1730 μs (h) t=1735 μs

Figure 55: CN mass fraction contours from Navier–Stokes simulation of the 1 Torr Titan condition (x2s522) in the X2 facility. The spectral measurements are taken at approximately t=1720 μs.

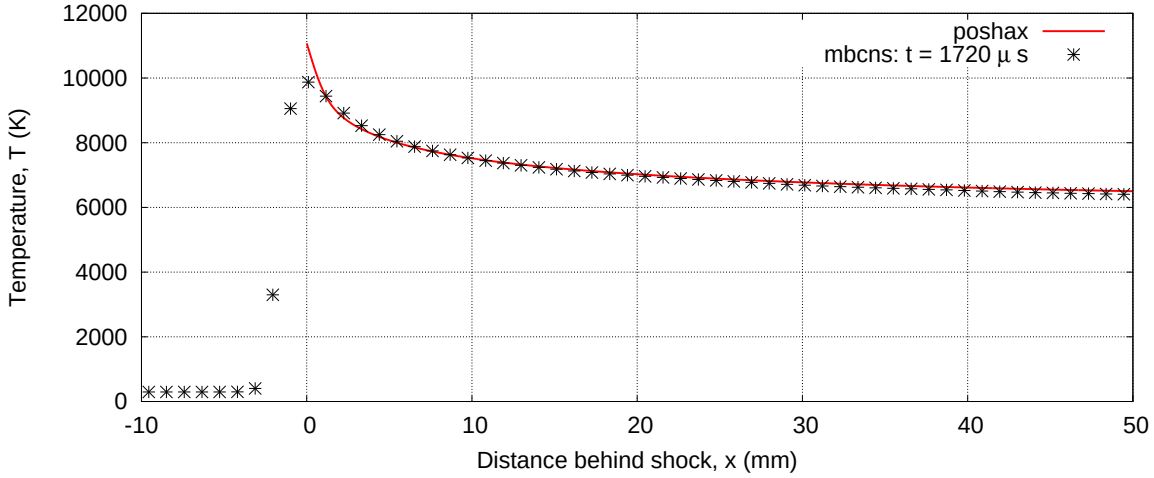

(a) Temperature

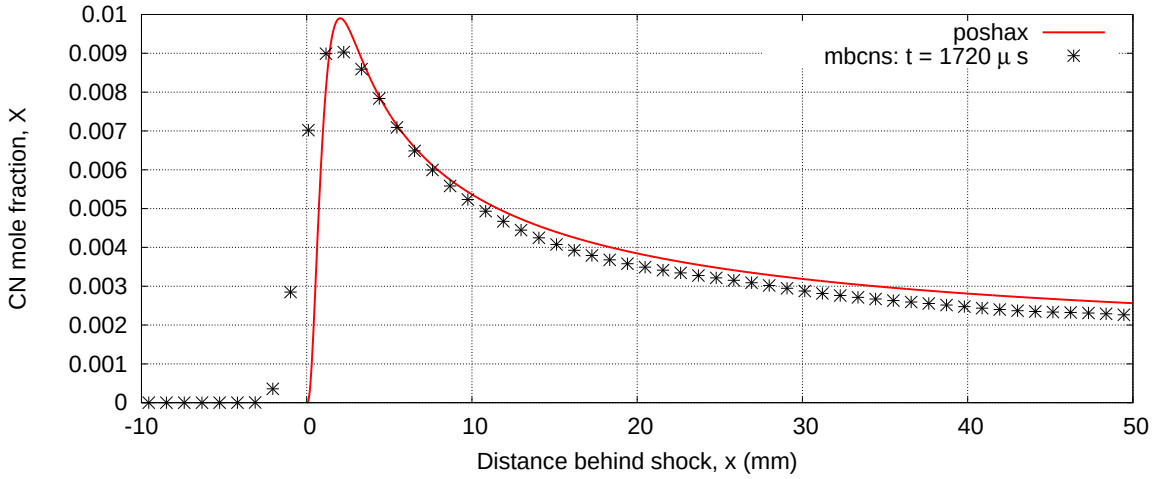

(b) CN mole fraction

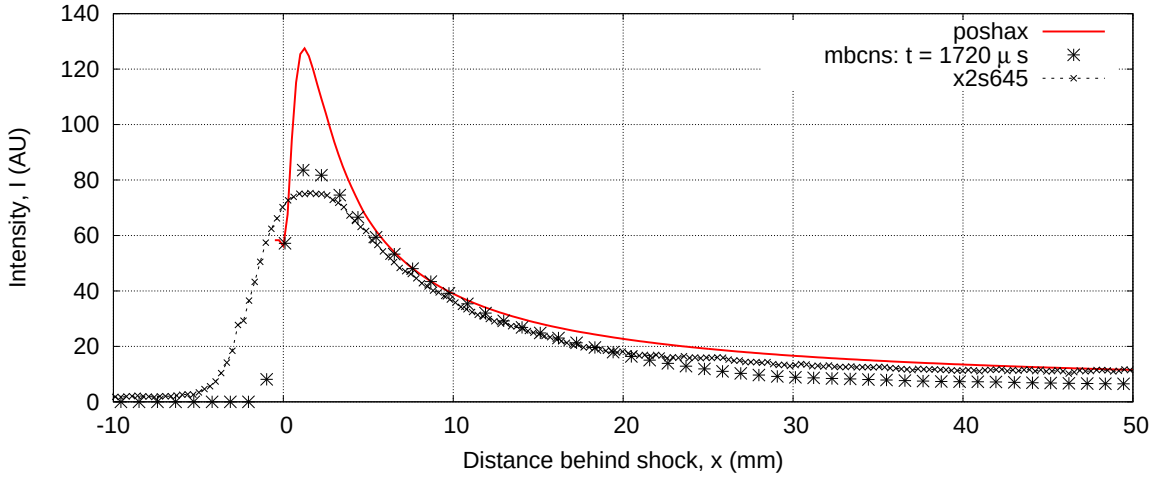

(c) Radiative intensity $310\,nm \leq \lambda \leq 450\,nm$

Figure 56: Comparison of one-dimensional and axisymmetric (centerline, $t = 1720\,\mu s$) profiles for the 1 Torr Titan condition in X2

The AUS instrument was mounted in the DC-8 at station 610 (the distance in inches from the nose of the aircraft). The instrument was co-aligned with an intensified near-UV spectrometer (IUV) as illustrated in Fig. 57. The IUV device was previously deployed in the Stardust observation campaign[72]. At station 610, a fused silica window was fitted to the DC-8 to enable acquisition of emission signatures in the near-UV region. The instrument was secured on top of a ball mount and pointed to the entering capsule by hand. A wide field of view video camera with good performance at low light levels was co-aligned with the spectrometer to facilitate manual tracking which was achieved by displaying the video signal on a headset display with cross-hairs.

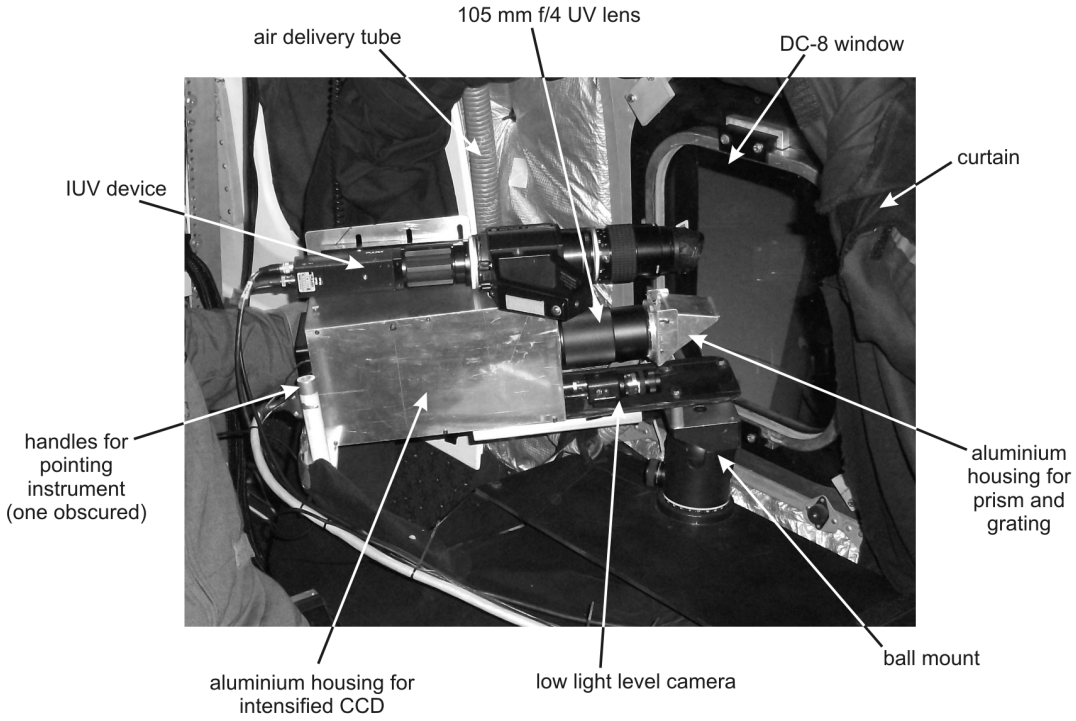

Figure 57: Annotated photograph showing the arrangement of the Australian Ultraviolet Spectrograph (AUS) mounted in the DC-8. [71]

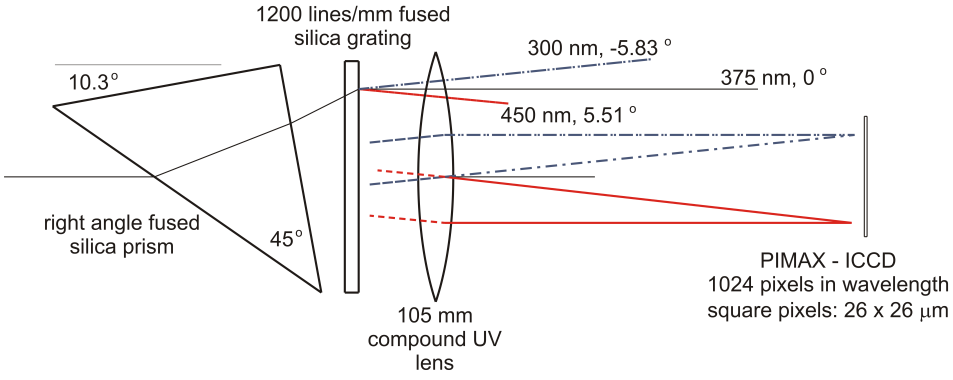

Figure 58: Optical arrangement of the Australian Ultraviolet Spectrograph (AUS). [71]

The design of the AUS instrument is illustrated in Fig. 58. The AUS instrument consisted of UV fused silica right angle prism (60 mm size, uncoated, Thorlabs: PS613) positioned ahead of a 1200 lines/mm fused

silica transmission grating (50 × 50 mm, Thorlabs: GTU50-12). An offset of approximately 10 degrees was applied to the prism to achieve a centre wavelength of about 375 nm on the intensified CCD array. The right angle prism and diffraction grating were embedded in an aluminium housing with mating 52 mm filter mount. The 105 mm lens used in the AUS device was manufactured by CoastalOpt and had colour correction between 250 and 650 nm and an f/4.5 maximum aperture.

Imaging of the emissions was achieved using a Princeton Instruments intensified CCD camera (PI-MAX 1024B with a GenII intensifier) with 1024 × 256 pixels. The longer 1024 pixel rows were aligned in the vertical direction – the direction of the wavelength dispersion, providing a dispersion of 0.187 nm/pixel. The FWHM of Hg lines identified during wavelength calibrations was about 3 pixels, corresponding to a resolution of approximately 0.5 nm. The spectrometer field of view in the direction of the 256 pixels was approximately 3.6 degrees. Images were exposed for 100 ms and read-out and stored during a period of 269.536 ms to produce data at a rate of approximately one frame every 0.370 seconds.

Results

Sample results from a frame recorded at 13:52:05.40 UTC are presented in Fig. 59. In this figure the primary feature of the ICCD image is the main bus, but the capsule region can be seen just below the main bus region. For the orientation of ICCD image of Fig. 59, the direction of increasing wavelength is towards the right of the page, and the direction of capsule travel is towards the bottom of the page. To define the capsule region, a strip of around 8 or more pixels (in the spatial direction) was manually identified for each frame, and the counts within this strip were summed in the spatial direction. The width of the pixel strip identified for each frame actually varied depending on motion blur arising from imprecise tracking of the capsule during the period of exposure of the ICCD frame (100 ms). When motion blur resulted in smearing in both the spatial and the wavelength directions, it was generally possible to track a spectral feature across adjacent pixels rows, and summation of the capsule counts at each wavelength was then performed along this oblique direction.

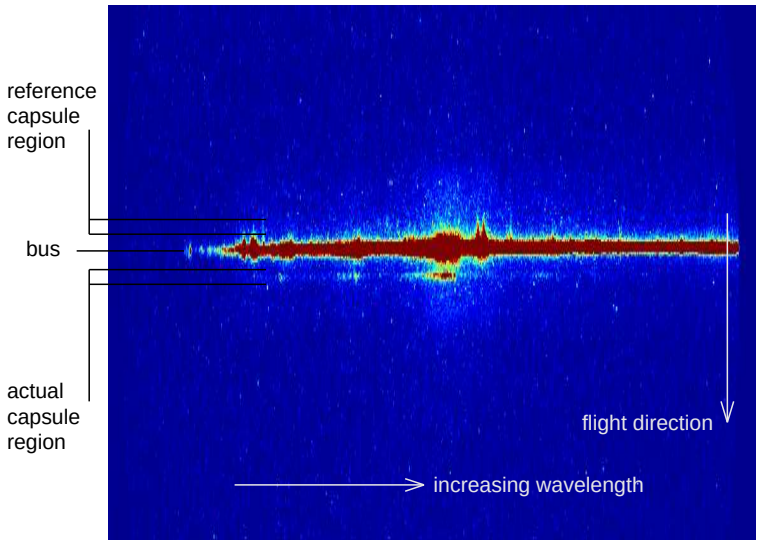

Figure 59: ICCD image acquired at 13:52:05.40 (UTC) (presented in false colour and an expanded spatial scale) illustrating the location of the Hayabusa capsule and the spacecraft bus. [71]

To identify the appropriate background level for subtraction from the capsule region results, the counts along two rows of pixels, one immediately above and the other immediately below the capsule region (in the orientation of the ICCD image in Fig. 59) were averaged across 3 pixels in the wavelength direction. The

background counts across the capsule region was then taken to be a linear variation in the spatial direction between the counts identified from the strip of pixels above and below the capsule region. A spectral feature within the net counts from the capsule region and the calibrated dispersion of the instrument (0.187 nm/pixel) allowed the assignment of wavelengths to each pixel. The net counts from the capsule region at each wavelength was then divided by the sensitivity figure of the instrument at each corresponding wavelength to determine the spectral irradiance received at the DC-8 location.

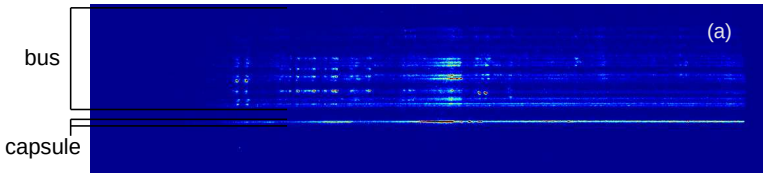

(a) False colour illustrating the location of the capsule and the spacecraft bus.

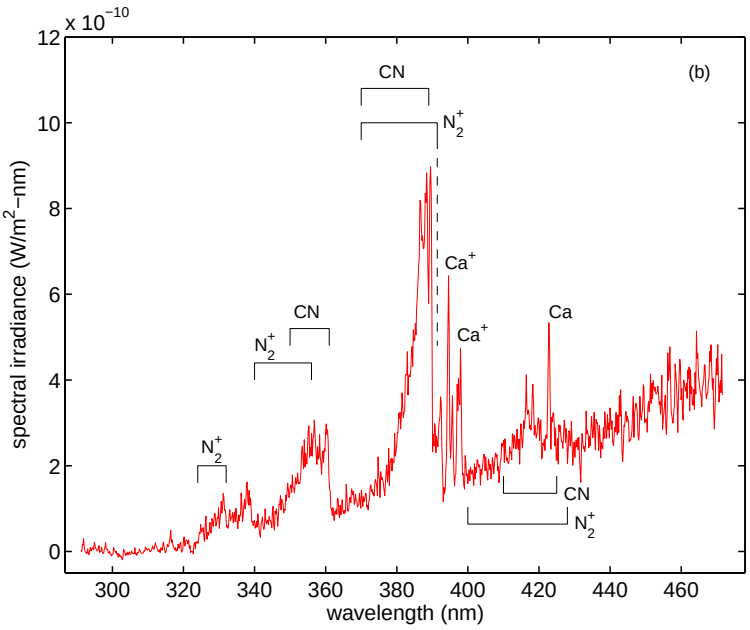

(b) Spectral irradiance received at the DC-8.

Figure 60: Results acquired at 13:52:22.40 (UTC). [71]

Results in Fig. 60b show emissions from a variety of molecular and atomic species superimposed on the continuum emissions from the capsule surface. The principal species contributing to observed molecular radiation are N_2^+ and CN. Carbon is a major element of Hayabusa's carbon phenolic ablator thermal protection system so CN is expected to be generated primarily through the combination of dissociated nitrogen in the high temperature shock layer air and ablation products from the heat shield. Calcium lines (Ca and Ca^+) are also apparent and on close inspection, aluminium lines can also be observed between the two Ca^+ lines.

8 CONCLUDING REMARKS

Expansion tubes can simulate the flow conditions relating to superorbital re-entry for time periods of up to the order of a millisecond. The flow generation process is complex and significant analysis is required to accurately define the flow conditions achieved. The total pressure generating capability of the facilities is so

high, up to the order of tens of gigapascals, that scaled testing of re-entry capsules is possible with reproduction of flight Reynolds numbers for a wide range of conditions. The test gas composition is, however, different to that in flight and this must be taken into account when evaluating the results of experiments performed in these facilities. By using models with preheated walls, the effects of ablation and ablation-radiation coupling can be studied using wall boundary conditions similar to those experienced by an ablating re-entry heat shield. When used with the appropriate instrumentation and analysis, these facilities form a powerful tool for the study of superorbital aerothermodynamic flow processes.

9 ACKNOWLEDGEMENTS

It takes a lot of people many hours to design, build and operate the physical facilities, the instrumentation and the flow simulation codes. Beyond the list of authors, material in this paper has come from the efforts of many graduate students and technical staff. Hardware has been manufactured by the technical staff of the faculty, including Brian Loughrey, Franz De Beurs, Neil Duncan, Keith Hitchcock, Eugene Kochnieff and Barry Allsop. Financial support, in large part, has been provided by the Australian Research Council through its various granting schemes, dating back to our first ARGS Large Grant in 1990. Significant funding has also come from the Queensland Smart State Research Facilities Fund. The University of Queensland High-Performance Computing Group has provided many years of large-scale computing support.

References

[1] P. A. Gnoffo, C. O. Johnston, and B. B. Kleb. Challenges to computational aerothermodynamic simulation and validation for planetary entry vehicle analysis. Technical report, NASA Langley Research Center, Hampton, Virginia, 2010.

[2] R. G. Morgan, T. J. McIntyre, D. R. Buttsworth, P. A. Jacobs, D. F. Potter, A. M. Brandis, R. J. Gollan, C. M. Jacobs, B. R. Capra, M. McGilvray, and T. N. Eichmann. Impulse facilities for the simulation of hypersonic radiating flows. In *38th Fluid Dynamics Conference and Exhibit*, pages Paper AIAA–2008–4270. American Institute of Astronautics and Aeronautics, June 2008.

[3] D. R. Buttsworth, M. D'Souza, D. Potter, T. Eichmann, N. Mudford, M. McGilvray, T. J. McIntyre, P. Jacobs, and R. Morgan. Expansion tunnel radiation experiments to support Hayabusa re-entry observations. In *48th AIAA Aerospace Sciences Meeting*, pages AIAA–2010–634. Americal Institute of Aeronautics and Astronautics, January 2010.

[4] E. L. Resler and D. E. Bloxom. Very high Mach number flows by unsteady flow principles. Limited Distribution Monograph January, Graduate School of Aeronautical Engineering, Cornell University, 1952.

[5] A. Hertzberg, W. E. Smith, H. S. Glick, and W. Squire. Modifications of the shock tube for the generation of hypersonic flow. Technical Note 55-14, Arnold Engineering Development Center, USA, 1955.

[6] R. L. Trimpi. A preliminary theoretical study of the expansion tube, a new device for producing high-enthalpy short-duration hypersonic gas flows. NASA Technical Report R-133, 1962.

[7] C. G. Miller and J. J. Jones. Development and performance of the NASA Langley Research Center expansion tube/tunnel, a hypersonic-hypervelocity real-gas facility. In D. Archer, R and B. E. Milton, editors, *14th International Symposium On Shock Tubes and Waves*, 1983.

[8] A. Dufrene, M. MacLean, R. Parker, T. Wadhams, and M. Holden. Characterization of the new LENS expansion tunnel facility. AIAA Paper 2010-1564, January 2010.

[9] M. MacLean, A. Dufrene, T. Wadhams, and M. Holden. Numerical and experimental characterization of high enthalpy flow in an expansion tunnel facility. AIAA Paper 2010-1562, January 2010.

[10] M. S. Holden. Experimental studies of radiation and plasma effects behind the incident shock in LENS XX, and the unsteady flow characteristics associated with "free flight" shroud and stage separation and mode switching in LENS II. In O. Chazot and K. Bensassi, editors, *RTO-EN-AVT-186 - Aerothermodynamic Design, Review on Ground Testing and CFD*. NATO Science and Technology Organization, April 2010.

[11] A. Paull, R. J. Stalker, and I. Stringer. Experiments on an expansion tube with a free-piston driver. AIAA Paper 88-2018, 1988.

[12] A. J. Neely and R. G. Morgan. The superorbital expansion tube concept, experiment and analysis. *The Aeronautical Journal*, 98(973):97–105, 1994.

[13] R. G. Morgan. *Handbook of Shock Waves*, volume 1, chapter Shock Tubes and Tunnels: Facilities, Instrumentation, and Techniques, Free-Piston Driven Expansion Tubes, pages 603–622. Academic Press, San Diego, 2001.

[14] A. Paull and R. J. Stalker. Test flow disturbances in an expansion tube. *Journal of Fluid Mechanics*, 245:493–521, 1992.

[15] J. Tamagno, R. Bakos, M. Pulsonetti, and J. Erdos. Hypervelocity real gas capabilities of GASL's expansion tube (HYPULSE) facility. AIAA Paper 90-1390, 1990.

[16] C. J. Doolan and R. G. Morgan. A two-stage free piston driver. *Shock Waves*, 9:239–248, 1999.

[17] D. E. Gildfind. *Development of High Total Pressure Scramjet Flow Conditions using the X2 Expansion Tube.* PhD thesis, The University of Queensland, School of Mechanicaland Mining Engineering., 2012.

[18] D. F. Potter, R. J. Gollan, T. N. Eichmann, T. J. McIntyre, R. G. Morgan, and P. A. Jacobs. Simulation of CO_2-N_2 expansion tunnel flows for the study of radiating shock layers. In *46th AIAA Aerospace Sciences Meeting and Exhibit*, pages Paper AIAA–2008–1280. American Institute of Astronautics and Aeronautics, January 2008.

[19] R. G. Morgan and R. J. Stalker. Double diaphragm driven free piston expansion tube. In *Proceedings of the Eighteenth International Symposium on Shock Waves, Sendai.*, pages 1031–1038, 1991.

[20] T.N. Eichmann, A.M. Brandis, D.F. Potter, T.J. McIntyre, and Rubinsztein-Dunlop. Radiating hypersonic flow studies using a super-orbital expansion tube. *40th Thermophysics Conference, Seattle, Washington*, 23 - 26 June 2008.

[21] A Dann, D Gildfind, RG Morgan, M McGilvray, and PA Jacobs. Upgrade of the X3 super-orbital expansion tube. In *18th Australasian Fluid Mechanics Conference*, page Paper 126, December 2012.

[22] M. G. Davey. A hypersonic nozzle for the x3 expansion tube. Fourth-year thesis, The University of Queensland, Department of Mechanical Engineering, Australia, December 2006.

[23] Hadas Porat, Richard G. Morgan, and J. McIntyre, Timothy. Study of radiative heat transfer in Titan atmospheric entry. In I. Grant, editor, *28th International Congress of the Aeronautical Sciences (ICAS 2012)*, pages Paper ICAS 2012–3.8.3, United Kingdom, September 2012. International Council of the Aeronautical Sciences.

[24] B. R. Capra and R. G. Morgan. Radiative and total heat transfer measurements to a titan explorer model. *A.I.A.A. Journal of Spacecraft and Rockets*, 49(1), 2012.

[25] Hadas Porat, Richard G. Morgan, and J. McIntyre, Timothy. Study of radiative heat transfer in Titan atmospheric entry. In P. A. Brandner and B. W. Pearce, editors, *Proceedings of the 18th Australasian Fluid MEchanics Conference*. Australasian Fluid Mechanics Society, December 2012.

[26] T.N. Eichmann. *Radiation measurements in a simulated Mars atmosphere.* PhD thesis, The University of Queensland, School of Mathematics and Physics., 2012.

[27] F. Zander, R. G. Morgan, U. Sheikh, D. R. Buttsworth, and P. R. Teakle. Hot-wall reentry testing in hypersonic impulse facilities. *AIAA Journal*, 51(2):476–484, 2013.

[28] H. Ma, R. Stevens, and R. Stone. In-cylinder temperature estimation from an optical spray-guided DISI engine with color-ratio pyrometry (CRP). In *SAE 2006 World Congress and Exhibition*, 2006.

[29] M. Balat-Pichelin, J.F. Robert, and J.L. Sans. Emissivity measurements on carbon-carbon composites at high temperature under high vacuum. *Applied Surface Science*, 253(2):778–783, 2006.

[30] T. J. McIntyre, A. I. Bishop, H. Rubinsztein-Dunlop, and P. A. Gnoffo. Experimental and numerical studies of ionizing flow in a super-orbital expansion tube. *AIAA Journal*, 41(11):2157–2161, 2003.

[31] T. N. Eichmann, T. J. McIntyre, A. I. Bishop, S. Vakata, and H. Rubinsztein-Dunlop. Three-dimensional effects on line-of-sight visualization measurements of supersonic and hypersonic flow over cylinders. *Shock Waves*, 16(4–5):299–307, 2007.

[32] Fabian Zander, Sannu Molder, Richard Morgan, Peter Jacobs, and Rowan Gollan. High temperature gas effects for converging conical shocks. In *18th AIAA/3AF International Space Planes and Hypersonic Systems and Technologies Conference*, September 2012.

[33] S. Molder. Internal, axisymmetric, conical flow. *A.I.A.A. Journal*, 5(7):1252–1255, 1967.

[34] M. J. Wright, J. Olejniczak, D. Bose, and T. Gokcen. A summary of radiation prediction capabilities for titan aerocapture applications. Technical report, NASA Ames Research Center, Moffat Field, California, 2004.

[35] Mary G. D'Souza, Troy N. Eichmann, Daniel F. Potter, G. Morgan, Richard, Timothy J. McIntyre, Peter A. Jacobs, and Neil R. Mudford. Observation of an ablating surface in expansion tunnel flow. *A.I.A.A. Journal*, 48(7):1557–1560, 2010.

[36] C. Park and M. Tauber. Heatshielding problems, a rewiew. In *A.I.A.A. Fluid Dynamics Conference*, pages Paper 99–3415, July 1999.

[37] P. A. Jacobs and R. J. Gollan. The Eilmer3 code: User guide and example book. Mechanical Engineering Report 2008/07, The University of Queensland, Brisbane, Australia, 2010.

[38] R. J. Gollan and P. A. Jacobs. About the formulation, verification and validation of the hypersonic flow solver Eilmer. *International Journal for Numerical Methods in Fluids*, Wiley Online Library(DOI: 10.1002/fld.3790), 2013.

[39] P. A. Jacobs, R. J. Gollan, D. F. Potter, D. E. Gildfind, T. N. Eichmann, and B. T. O'Flaherty. CFD tools for design and simulation of transient flows in hypersonic facilities. In O. Chazot and K. Bensassi, editors, *RTO-AVT-VKI Lecture Series 2010-AVT186 Aerothermodynamic Design, Review on Ground Testing and CFD.*, Belgium, April 2010. von Karman Institute for Fluid Dynamics.

[40] H. Bernier and J. Gambart. MOOREA, an internal ballistic code for two stage light gas gun study. In *38th Meeting of the Aeroballistic Range Association.*, 1987.

[41] C. P. T. Groth and J. J. Gottlieb. Numerical study of two-stage light-gas hypervelocity launchers. UTIAS Report 327, Institute for Aerospace Studies, University of Toronto., 1988.

[42] J. Lacey and D. Long. A wave diagram computational method with application to a free-piston shock tube. AIAA Paper 90-1378, 1990.

[43] C. P. T. Groth, J. J. Gottlieb, and P. A. Sullivan. Numerical investigation of high-temperature effects in the UTIAS-RPI hypersonic impulse tunnel. *Canadian Journal of Physics*, 69(7):897–918, 1991.

[44] D. G. Edwards, K. C. Phan, and C. V. Hurdle. Computational modelling of the gas flow from a high-enthalpy blast simulator. In *17th International Symposium on Shock Waves and Shock Tubes*, pages 891–896, 1989.

[45] H. Gurgenci and W. R. B. Morrison. Rocketdyne shock tunnel: Diaphragm research and development program. WBM Report 6058, 1989.

[46] P. A. Jacobs. Single-block Navier-Stokes integrator. ICASE Interim Report 18, 1991.

[47] E. Oran and J. Boris. *Numerical Simulation of Reactive Flow*. Cambridge University Press, New York, USA, 2nd edition, 2001.

[48] R.J. Stalker. Use of argon in a free piston shock tunnel. In *AIAA Plasmadynamics Conference, Monterey, California, March 2-4, AIAA Paper No. 66-169*, 1966.

[49] R.J. Stalker. A study of the free-piston shock tunnel. *AIAA Journal*, pages 2160–2165, 1967.

[50] A. Paull and R.J. Stalker. Test flow disturbances in an expansion tube. *Journal of Fluid Mechanics*, 245:493–521, 1992.

[51] K. Itoh, S. Ueda, T. Komuro, K. Sato, M. Takahashi, H. Myajima, H. Tanno, and H. Muramoto. Improvement of a free piston driver for a high-enthalpy shock tunnel. *Shock Waves*, 8:215–233, 1998.

[52] H. Tanno, K. Itoh, T. Komuro, and K. Sato. Experimental study on the tuned operation of a free piston driver. *Shock Waves*, 10:1–7, 2000.

[53] Hans G. Hornung. The piston motion in a free-piston driver for shock tubes and tunnels. Technical Report GALCIT Report FM 88-1, Graduate Aeronautical Laboratories, California Institute of Technology, Jan 1988.

[54] P.A. Jacobs, T.B. Silvester, R.G. Morgan, M.P. Scott, R.J. Gollan, and T.J. McIntyre. Superorbital expansion tube operation: estimates of flow conditions via numerical simulation. Paper presented to the 43rd AIAA Aerospace Sciences Meeting, Reno, NV, 10-13 January, 2005.

[55] H. Mirels. Test time in low-pressure shock tubes. *The Physics of Fluids*, 6(9):1201–1214, 1963.

[56] A.M. Brandis, R.J. Gollan, M.P. Scott, R.G. Morgan, P.A. Jacobs, and P.A. Gnoffo. Expansion tube operating conditions for studying nonequilibrium radiation relevant to Titan Aerocapture. *42nd Joint Propulsion Conference and Exhibit, 9 - 12 July 2006, Sacramento, California*, 2006.

[57] Pascal Boubert. TC2 - M1: Definition of shock tunnel test-cases for gas radiation prediction in Mars-like atmosphere. In *Rebuilding of Selected Test Cases, Radiation Workshop in Roma*, volume ESA SP 629, pages 12 –, Rome, Italy, 2006. European Space Agency.

[58] M.P. Scott. *Development and Modelling of Expansion Tubes*. Phd thesis, School of Engineering, St Lucia, QLD, June 2006.

[59] S. Gordon and B.J. Mcbride. Computer program for calculation of complex chemical equilibrium compositions and applications. Part 1: Analysis. NASA Reference Publication 1311, United States, 1994.

[60] R.J. Bakos and R.G. Morgan. Chemical recombination in an expansion tube. *AIAA Journal*, 32(6):1316 – 1319, 1994.

[61] C.S. Park. Assessment of two-temperature kinetic model for ionizing air. *Journal of Thermophysics and Heat Transfer*, 3(3):233–244, 1989.

[62] C.S. Park, J.T. Howe, R.L. Jaffe, and G.V. Candler. Review of chemical-kinetic problems of future NASA missions, II: Mars entries. *Journal of Thermophysics and Heat Transfer*, 8(1):9 – 22, 1994.

[63] A.M. Brandis, R.G. Morgan, T.J. McIntyre, and P.A. Jacobs. Nonequilibrium radiation intensity measurements in simulated Titan atmospheres. *40th Thermophysics Conference, Seattle, Washington*, 23 - 26 June 2008.

[64] R.J. Gollan, C.M. Jacobs, P.A. Jacobs, R.G. Morgan, T.J. McIntyre, M.N. Macrossan, D.R. Buttsworth, T.N. Eichmann, and D.F. Potter. A simulation technique for radiating shock tube flows. *26th International Symposium on Shock Waves (ISSW26)*, July 2007.

[65] R.J. Gollan. *Computational Modelling of High-Temperature Gas Effects with Application to Hypersonic Flows*. PhD thesis, School of Engineering, The University of Queensland, June 2008.

[66] D.F. Potter. Validation of Aerothermo-Chemistry Models for Re-Entry Applications – TN 3.5: Comparison with Experiments. Technical Note 3.5, European Space Agency, European Space Research and Technology Centre, Noordwijk, The Netherlands, May 2009.

[67] J Olejniczak, M Wright, D Prabhu, N Takashima, B Hollis, E V Zoby, and K Sutton. An Analysis of the Radiative Heating Environment for Aerocapture at Titan. *AIAA Paper No. 2003-4953*, 2003.

[68] Tahir Gökçen. N_2 - CH_4 -Ar Chemical Kinetic Model for Simulations of Atmospheric Entry to Titan. *37th AIAA Thermophysics Conference, 28 June - 1 July 2004, Portland, Oregon*, 2004.

[69] P Jenniskens. Observations of the stardust sample return capsule entry with a slitless echelle spectrograph. *Journal of Spacecraft and Rockets*, 47(5):718–735, 2010.

[70] T.N. Eichmann, R. Khan, T.J. McIntyre, C. Jacobs, H. Porat, D. Buttsworth, and B. Upcroft. Radiometric temperature analysis of the hayabusa spacecraft re-entry. In *28th International Symposium on Shock Waves*, Manchester, UK, 17 – 22 July 2011.

[71] D Buttsworth, R Morgan, and P Jenniskens. Near ultraviolet emission spectroscopy of the hayabusa re-entry. In *50th AIAA Aerospace Sciences Meeting*, AIAA Paper 2012-1297, Nashville, Tennessee, 9 – 12 January 2012.

[72] R L Rairden and P Jenniskens. Near-ultraviolet spectroscopy of the stardust sample return capsule reentry. *Journal of Spacecraft and Rockets*, 47(5):753–756, 2010.